Title: Engineering of Lead Selenide Quantum Dot Based Devices and Core/Shell
                 Heterostructures

Author(s):   Nakotte, Tom

Intended for: Thesis

Issued: 2020-04-13

Engineering of Lead Selenide Quantum Dot Based Devices and Core/Shell Heterostructures

By: Tom Nakotte

A dissertation submitted to the Graduate School

in partial fulfillment of the requirements

for the degree

Doctor of Philosophy

Specialization in Chemical and Materials Engineering

New Mexico State University

Las Cruces, New Mexico, United States

May 2020

Tom Nakotte

Candidate

Chemical Engineering

Major

This Dissertation is approved on behalf of the faculty of New Mexico State University, and it is acceptable in quality and form for publication:

Approved by the Dissertation Committee:

Hongmei Luo

Chairperson

Jeffery Pietryga

Committee Member

Reza Foudazi

Committee Member

Jessica Houston

Committee Member

Stefan Zollner

Committee Member

Acknowledgements

Vita

August 30, 1992	Born in Amsterdam, North Holland, Netherlands
May 2010	Graduated from Pojoaque Valley High School
May 2014	Graduated from University of New Mexico with a Bachelor of Science in Chemical Engineering

Publications

1. **Nakotte, T**.; Luo, H.; Pietryga, J. "Carrier Density Modulation in PbSe Quantum Dot Films via In-Solution Ligand Exchange" MRS Advances. **2020**; submitted

2. **Nakotte, T**.; Luo, H.; Pietryga. J. "PbE (E = S, Se) Colloidal Quantum Dot-Layered 2D Material Hybrid Photodetectors" *Nanomaterials*. **2020**; 10(1):172

3. Kozlov, O. V.; Park, Y.-S.; Roh, J.; Fedin, I.; **Nakotte, T**.; Klimov, V. I. "Sub–single-exciton lasing using charged quantum dots coupled to a distributed feedback cavity" *Science* **2019**, 365, 672-675.

4. Wang, H.; Yan, L.; **Nakotte, T**.; Xu, W.; Zhou, M.; Ding, D.; Luo, H. "IrO2-incorporated La0.8Sr0.2MnO3 as a bifunctional oxygen electrocatalyst with enhanced activities" *Inorganic Chemistry Frontiers* **2019**, 6, 1029-1039.

5. Shan, C.; Wu, K.; Yen, H.-J.; Narvaez Villarrubia, C.; **Nakotte, T**.; Bo, X.; Zhou, M.; Wu, G.; Wang, H.-L. "Graphene Oxides Used as a New "Dual Role" Binder for Stabilizing Silicon Nanoparticles in Lithium-Ion Battery" *ACS Applied Materials & Interfaces* **2018**, 10, 15665-15672.

6. Sarker, S.; Chaturvedi, P.; Yan, L.; **Nakotte, T**.; Chen, X.; Richins, S. K.; Das, S.; Peters, J.; Zhou, M.; Smirnov, S. N.; Luo, H. "Synergistic effect of iron diselenide decorated multi-walled carbon nanotubes for enhanced heterogeneous electron transfer and electrochemical hydrogen evolution" *Electrochimica Acta* **2018**, *270*, 138-146.

7. Lin, Q.; Yun, H.J.; Liu, W.; Song, H.J.; Makarov, N.S.; Isaienko, O.; **Nakotte, T**.; Chen, G.; Luo, H.; Klimov, V.I.; et al. "Phase-transfer ligand exchange of lead chalcogenide quantum dots for direct deposition of thick, highly conductive films" *J. Am. Chem. Soc.* **2017**, 139, 6644–6653.

Abstract

Near infrared (NIR) emitting colloidal quantum dots (QDs) such as PbSe are interesting materials for implementation in various optoelectronic devices such as solar cells, photodetectors, and radiation detectors. Material properties like size tunable emission wavelengths, facile solution processability, the possibility of carrier multiplication and Auger assisted up-conversion, and high Z number provide PbSe QDs with unique advantages over many currently available commercial materials used in these devices.

In this dissertation, after an introduction to QDs in general, we first focus on synthesis of PbSe-based heterostructured QDs for study via optical spectroscopy. PbSe/CdSe QDs synthesized via cation exchange reaction were used as seeds to study the proper conditions for further CdSe or CdS shell growth. Optical spectroscopy studies show that growth of thicker CdSe shells leads to tunable visible emission, while growth of thick CdS shells can greatly increase the photoluminescence quantum yield (PLQY) observed from the intermediate CdSe shell. NIR PL lifetimes can be greatly enhanced by the growth of CdS shells, due to strong delocalization of the hole wavefunction within the PbSe core, while the electron is delocalized throughout the QD including in the CdS shell, resulting in radiative lifetimes in the tens of microseconds. Two pulse delay measurements show that Auger assisted up conversion is also taking place in these engineered QD dot heterostructures.

In the sections that follow, we look at QD devices, first with a focus on novel devices fabricated from PbSe QDs, using an amine synthesis method that allows for facile in-solution ligand exchange. QD film mobilities are measured for PbSe QDs capped with various short ionic ligands. Carrier densities in PbSe QD films are calculated from C-V measurements, showing for the first time that carrier densities can be modulated by simply changing the capping ligand.

Radiation detectors utilizing PbSe QDs capped with KI and NH$_4$I ligands show tangible response to incident alpha radiation. Current output response to alpha radiation is dependent on strength of radiation source and amount of bias voltage applied.

In the final section a critical review of hybrid layered 2D-QD photodetectors is presented. In a typical example, PbSe and PbS QDs act as the absorbing layer in phototransistor devices which utilize layered 2D materials such as graphene and transition metal dichalcogenides as transport layers. Resulting devices display high gains and improved directivities compared to QD only and 2D only devices.

Table of Contents

List of Tables

List of Figures

and graphene (valence and conduction band values of the PbS QD are 5.35 eV and 4.15 eV respectively, while the value for graphene reads 4.6 eV). **(C)** Horizontal shift of the transfer curves ($I_{DS} \sim V_G$, $V_{DS} = 0.5$ V) of the hybrid graphene-PbS QDs devices with different thicknesses of PbS QDs layers under irradiation with 6.4 mW cm^{-2} of 895 nm light. Saturation after 150 nm indicates that any carriers generated further than 150 nm from graphene layer are not collected; **(D)** [Top] Photocurrent response as a function of time of a hybrid graphene-PbS QDs phototransistor. The temporal response indicates a rise time of ~10 ms, and two different fall times on the order of 100 ms (50%) and 1s (see inset, measured at a higher power of 267 pW). [Bottom] temporal response of a bilayer graphene phototransistor after the laser is turned off and application of a reset pulse for 10 ms. The fall time is reduced from several seconds to ~10ms (insets: energy diagrams showing effect of reset pulse lowering potential barrier allowing electrons trapped at graphene-QD barrier to escape); **(E)** Transfer characteristics (I_{DS}-V_G, $V_{DS} = $ 0.1V) of *p*-doped graphene phototransistors before (dashed lines) and after (black) deposition of PbS QD with varying ligand length (schematic not to scale) red line is transfer curve under illumination with unfocused laser light ($\lambda = 514$ nm) with P = 10 W m^{-2}. Size of shift after deposition is an indication of coupling between graphene and QD layer; shift upon illumination is an indication of charge transfer of photoexcited carriers. **(F)** Responsivity as a function of incident power for hybrid detector using short TGL ligands (inset: responsivity as a function of V_G) (G) Photocurrent dependence on photon energy of the incident light (P ≈ 10^{-11} W) at different gate voltages for same device as Figure F. *Figures reprinted by permission from: (A and D) Ref. [190]. Springer Nature COPYRIGHT (2012); (B and C) Ref. [199]. John Wiley and Sons COPYRIGHT (2012), (E, F, and G) Ref. [200]. John Wiley and Sons COPYRIGHT (2015).*

Figure 4.5. (A) Schematic representation of a combined QD photodiode and graphene phototransistor device; V_{TD} creates a bias in the photodiode. **(B)** Schematic of a typical hybrid graphene-QD vertical phototransistor using graphene as an electrode. **(C)** Comparison of responsivity as a function of wavelength at various applied biases for devices using graphene and ITO as an electrode, respectively. **(D)** Energy band diagram of graphene QD interface; yellow shading indicates the depletion region in the QD layer. Top schematic is when detector is operated in only phototransistor mode, while the bottom shows the expansion of the depletion region when QD layer is used as a photodiode with an applied bias. **(E)** Photocurrent response of hybrid graphene-PbS QD phototransistor as a function of time for light on/off cycles at an irradiance of 335 mW/cm2, ($V_{DS} = 1$ V and $V_{GS} = 1.5$ V). **(F)** Zoomed in view of E to see rise and decay times of device, rise time 8ms, decay time 125 ms. *Figures reprinted with permission from; (A and D) Ref. [205]. Springer Nature COPYRIGHT (2016), (B) Ref. [208]. AIP Publishing COPYRIGHT (2016), (C) Ref. [207]. AIP Publishing COPYRIGHT (2011), (E and F) Ref. [209]. Copyright (2017) American Chemical Society.*

Figure 4.6. (A) Photocurrent response of hybrid MoS$_2$-PbS QD phototransistor as a function of time at various, relatively high gate voltages ($V_{DS} = 1$ V, irradiance 3 μW/cm^2). **(B)** Schematics of bare MoS$_2$ phototransistor as well PbS QD/MoS$_2$ phototransistor with and without TiO$_2$ buffer layer; label colors correspond with points on the graph. Graph is On/Off ratio as a function of dark current density, demonstrating that a TiO$_2$ buffer layer helps to reduce dark current. **(C)** [Right] Responsivity as a function of irradiance for hybrid MoS$_2$-PbS QD device with a TiO$_2$ buffer layer at different gate voltages ($V_{DS} = 1$ V). [Left] Photocurrent decay time of a light response at 67 nW/cm^2; the approximation with a single-exponential function results in a time constant of 12 ms. **(D)** Schematic of hybrid MoS$_2$-PbS QD devices using EDT and TBAI ligands to create a built in potential (energy-band diagram inset), and [right] response time of device

List of Abbreviations

ACN	acetonitrile
AFM	atomic force microscope
ALD	atomic layer deposition
BP	black phosphorous
CdOA	cadmium oleate
CM	carrier multiplication
CMOS	complementary metal–oxide–semiconductor
CTAB	cetyltrimethylammonium bromide
CVD	chemical vapor deposition
DIP	di-i-butylphosphine
DFP	2, 6-diflouropyridine
DMF	N, N-dimethylformamide
DOS	density of states
DTG	2, 3-dimercapto-1-propanol
EDT	1, 2-ethanedithiol
Eg	band gap
EQE	external quantum efficiency
FET	field effect transistor
FTIR	Fourier transform infrared spectroscopy
IQE	internal quantum efficiency
LED	light-emitting-diode
MPA	mercaptopropionic acid
NIR	near-infrared
OA	oleic acid
ODA	octadecylamine
ODE	1-octadecene
OFET	optical field effect transistor

OLA	oleylamine
PL	photoluminescence
PLQY	photoluminescence quantum yield
SILAR	successive ionic layer absorption reaction
SeSUS	selenium suspension
TBAI	tetrabutylammonium iodide
TCE	tetrachloroethylene
TEM	transmission electron microscope
TGL	thioglycerol
TMD	transition metal di-chalcogenide
TOP	tri-n-octylphosphine
TOPSe	tri-n-octylphosphine selenide
QD	quantum dot

Chapter 1: Introduction

1.1 What are Quantum Dots?

Quantum dots (QDs) are 0-dimensional semiconductor nanocrystals, that are typically comprised of II-VI, IV-VI, III-V, group V, CIS(e), or perovskite materials. Their sizes are smaller than (or comparable to) the exciton Bohr radius of the semiconductor material. Classically the Bohr exciton radius is defined as:

$$a_B = \frac{4\pi\varepsilon_r\hbar^2}{\mu e^2}$$

Equation 1.1

where ε_r is the relative dielectric constant of the material, e is electronic charge, $\hbar$ is the reduced Plank's constant, and μ is the reduced mass of electron-hole bound state [1]. The reduced mass can be calculated with **Equation 1.2;**

$$\mu = \left(\frac{m_e^* m_h^*}{m_e^* + m_h^*}\right) \qquad\qquad Equation\ 1.2$$

where m_e^* and m_h^* are effective mass of electron and holes respectively in M.K.S units. In PbSe the electron and hole have similar masses in the bulk phase, therefore the electron and hole will have comparable wave functions leading to an ideal QD in the strong confinement regime where both the electron and hole are confined [2]. In PbSe electrons and holes of an electron hole bound pair each have a Bohr radii of 23 nm resulting in an exciton Bohr radius of 46 nm [3]. The small size of the QD causes the material to display quantum confinement effects, such as the disappearance of band energies in favor of spatially quantized energy states, along with increased exciton lifetimes, and narrow photoluminescence (PL) peaks [4]. These effects are favorable for various applications. Examples are solar cells, where the long excitonic lifetimes allow for more

efficient collection of photogenerated carriers [5], and light-emitting-diodes (LEDs) [4] and lasers [6], where the narrow PL peaks cause visible emitting QDs to display very sharp colors.

The discrete energy levels in the electronic structure can be seen in the fine structures of the absorption spectra of quality monodisperse PbSe QDs **Figure 1.1 (A)**. The first absorption peak can be ascribed to the 1S excitonic transition, the second to the 1P transition, and third to the 1D transition **Figure 1.1 (B)** [7].
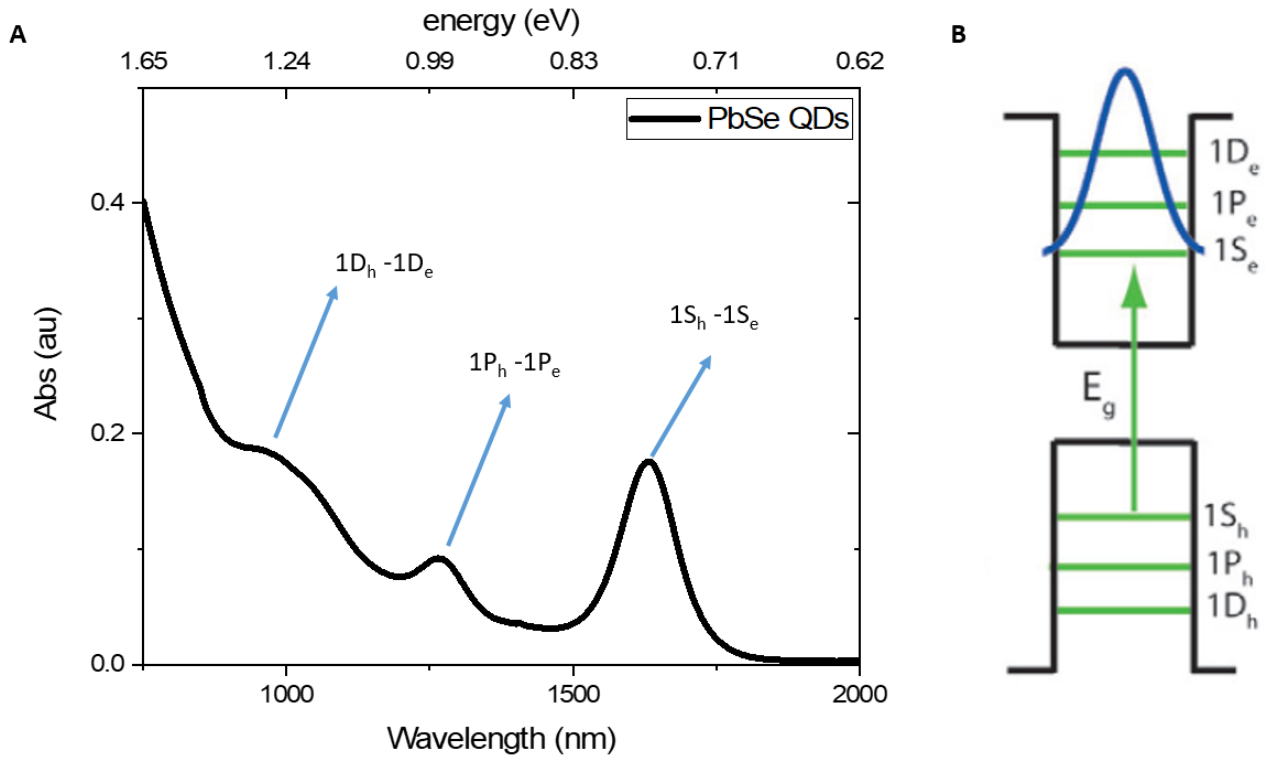
Figure 1.1 (A) Typical absorption spectra of PbSe QDs with good monodispersity in which discrete energy transitions can be seen. **(B)** Schematic of the discrete energy levels located in the valence and conduction band of a PbSe QD. Reprinted from Ref [7].

1.1.1 History

QDs were initially discovered in glass in 1980 [8,9] by Alexie Ekimov with the first reported instance of QDs forming in colloidal solutions by Luis E. Brus in 1983 [10]. The term "quantum dot" was officially coined in 1985 in a paper by Reed *et al.*, who observed a

completely spatially quantized system when studying GaAs-AlGaAs quantum wells [11]. PbSe QDs were first effectively synthesized and characterized in phosphate glass by Liposkvii *et al.* in 1997 [3]. However, much of the early advancements in QD synthesis were made on cadmium chalcogenide structures such as CdSe and CdS, because their air stability makes them less difficult to work with. For example, the first instance of monodisperse QDs was presented by Murray *et al.* in 1993 [12], where the hot injection method combined with size selective purification methods was used to produce CdE (E= S, Se, and Te) with less than 5% size variation within the ensemble. The use of less reactive precursors, cadmium oxide (CdO) and phosphonic acid, which allow for better separation of the nucleation and growth phases was introduced by Peng *et al.* [13] in 2001. This procedure results in highly monodisperse QDs without need for size selective precipitation, and catapulted quality QD synthesis into other material systems including the lead chalcogenide system. Since then, much research has been done in understanding both the chemistry and physics of QDs, leading to great advancements in both synthetic techniques and understanding how the chemical and physical properties of the dots affect their electronic and optical properties.

1.1.2 Density of States

The effect of quantum confinement in QDs can be understood by using the density of states (DOS) function. DOS describes the number of states per unit energy in a system and is important in determining the carrier concentration and energy density in a semiconductor. In bulk semiconductors the DOS function within a single band is continuous, meaning that carriers (electrons and holes) are not physically constrained in any dimension. However, as the material is reduced in dimension to 2D (*i.e.* nanoplatelets), 1D (*i.e.* nanorods), and 0D (*i.e.* QDs) the carriers become more and more confined. For 2D systems the carriers are still free to move along

the x and y-axis but are confined in the z-axis, while for 1D materials carriers are only free to move along 1 axis. In the case of QDs the carriers are confined in all directions resulting in quantized energy states similar to that of an atom. **Figure 1.2** is a simple illustration of the effect confinement has on electrons and the resulting influence on the energy states.
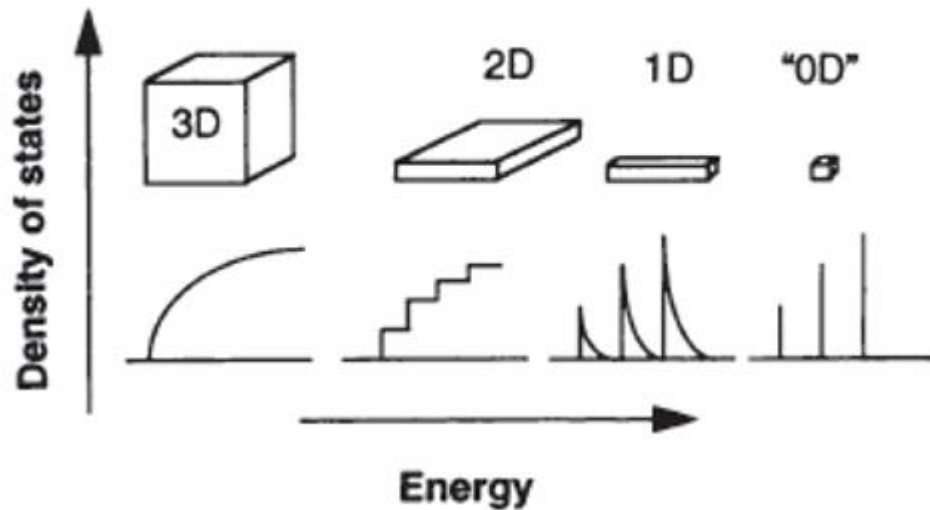
Figure 1.2 Graphical representation of the DOS in one band of a semiconductor as a function of dimension. Reprinted from ref [4].

1.1.3 Bandgap

The band gap (Eg) is defined as the energy position difference between the lowest energy edge of the conduction band and the highest energy edge of the valence band. Metallic materials, such as gold and copper, have no gap between their valence and conduction bands, meaning there is a continuous availability of electrons in these closely spaced orbitals, this results in the material being a very good conductor. When a material has a large Eg (*i.e.* larger than 4 eV), the material is considered an insulator, meaning that it is a very poor conductor. When Eg is between 0 to 4 eV, the material is considered a semiconductor, in this region, the application of voltage or absorption of a photon, through the photoelectric effect, can cause the material to conduct

current. Semiconductors are the basis for modern technology including computer chips, solar cells, and photodetectors.

There are two types of Eg, indirect and direct. A semiconductor is considered to have a direct Eg if the electrons and holes in the valence and conduction bands have the same crystal momentum in their Brillouin zone, in which case an excited electron can directly emit a photon. If the electrons and holes have different crystal momentum the Eg is considered indirect. If a material has an indirect Eg the excited electron must go through a phonon assisted momentum change during the transition from the valence band to conduction band in order to absorb a photon, see **Figure 1.3** [14]. Therefore, the energy conversion of absorbing or emitting photons is very weak in the indirect Eg materials, meaning direct Eg materials are more attractive for applications in which energy conservation is desirable (*e.g.* solar cells and photodetectors). Depending on the range of the Eg, QDs can be used for different applications, for instance QDs with an Eg in the visible regime (1.6-3.1 eV), such as CdS and CdSe, are commonly used for light-emitting-diodes (LEDs), while near-infrared (NIR) QDs such as PbSe and PbS are commonly used for solar cells and signal detection.
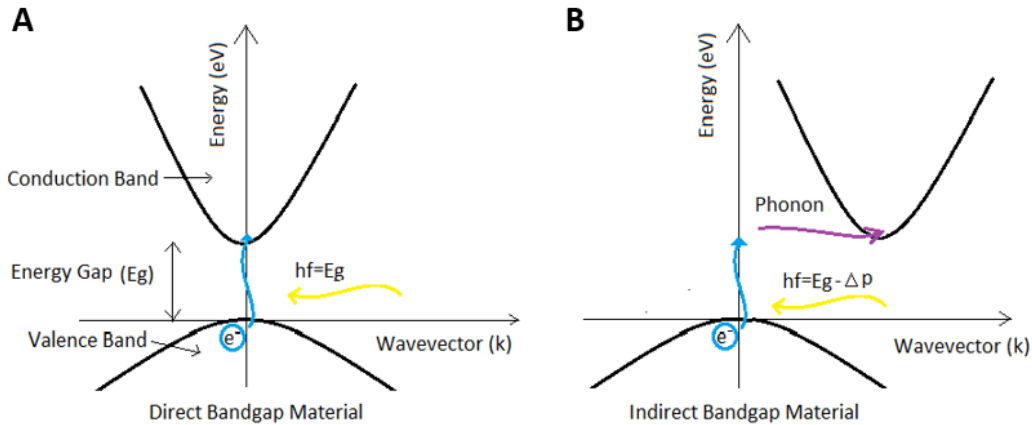
Figure 1.3 (A) Illustration of a direct band gap semiconductor in which an excited electron (represented by the blue arrow) can directly emit a photon (represented by the yellow arrow). **(B)** Illustration of an indirect band gap semiconductor in which a phonon (represented by the purple arrow) must assisted the excited electron to reach the conduction band state in order for a photon to be emmitted. Reprinted from ref [14]

1.1.4. Why PbSe Quantum Dots?

PbSe is an established family of QDs with well-documented reproducible synthesis techniques to control both the size [15,16], shape [17-19], and composition [20,21] as well as improve the stability of the dots in air [22], which was an inhibiting factor when PbSe QDs were initially synthesized. PbSe QDs have size-tunable optical absorption and emission properties that can range anywhere from the NIR (~1150 nm) [15,16] to mid-IR (~4000 nm) [23], which make them interesting materials for a wide array of applications from IR photo-detectors to photovoltaics. PbSe QDs are also the first material for which carrier multiplication (CM), a process in which multiple electron-hole pairs are generated by the absorption of one photon with energy in excess of 2 Eg, was observed and quantified [24]. PbSe is also dense and relatively high in atomic or 'Z' number, meaning this material has high radiation stopping power, which is a key factor in radiation detection, especially for detection of X-rays that have energies in the in the keV range or possibly even gamma rays that have energies in excess of 100 keV [25]. CM can be enhanced

6

by shelling PbSe QDs with a larger bandgap material such as a cadmium chalcogenide (*i.e* PbSe/CdSe core/shell QDs), which forms a quasi-type II band alignment when the shell is sufficiently thick, meaning the conduction bands of the PbSe core and CdSe shell have a negligible energy band offset but the valence bands have a large energy offset, see section 2.1. This type of band alignment leads to slowed intraband cooling and enhanced carrier-carrier Coulomb interactions due to the ground-state hole wavefunction being spatially confined in the lower energy core [26]. Increasing the aspect ratio (length/diameter) of QDs to make nano-rods instead of QDs, can also lead to improvements in CM efficiency by reducing the density of charges, spreading them out along the nano-rod direction (which leads to a reduction in Auger recombination rates), while simultaneously maintaining a certain degree of confinement which is controlled primarily by the cross-sectional size of the nano-rod [27].
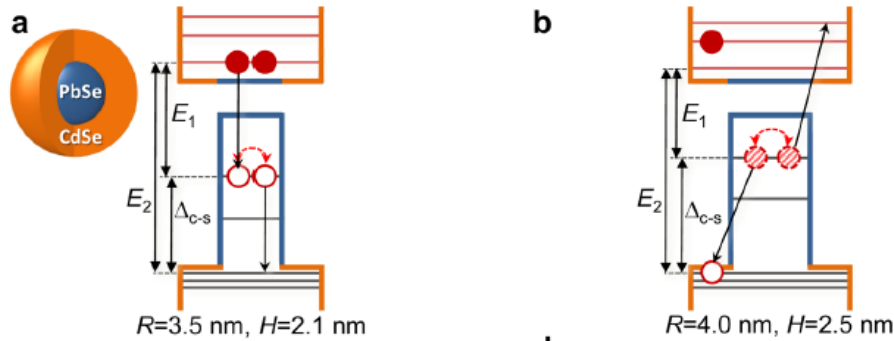
Figure 1.4 (A) Schematic representation of a core shell QD optimized for auger up-conversion. 2E1>E2, meaning that the visible emission (E1) is more than half the infrared emission (E2) is wavelength i.e visible emission 700 nm IR emission at 1200 nm. **(B)** Schematic representation of a core/shell QD optimized for CM, 2E1<E2. Reprinted from ref [28].

In addition to improving CM, growing a thick CdSe shell on PbSe QD cores also provides the possibility of Auger up-conversion occurring. Up-conversion is a process in which 2 or more sub-*Eg* energy photons generate a single above *Eg* exciton, allowing for the possibility

of harvesting lower energy photons that would typically be lost in a core-only device. Auger up-conversion in PbSe/CdSe QDs with a substantially thick shell would result in two lower-energy core-based excitons converted into a single higher-energy shell-based exciton; this process can be observed spectroscopically by exciting the core/shell QDs with lower-energy photons that can only be absorbed by the core and subsequently observing higher-energy emission from the CdSe shell. These infrared/visible dual emission QDs can be tailored towards either being more proficient in CM or in Auger up-conversion by altering the ratio of the higher and lower energy bandgaps, with a ratio >2 being ideal for CM and <2 leading to higher Auger up-conversion efficiencies [28], see **Figure 1.4**.

1.2 Synthesis of PbSe Quantum Dots

There are multiple methods that are commonly used for synthesis of QDs including colloidal methods as well as epitaxial methods. One of the most common and efficient ways to synthesize QDs with a narrow size distribution is via hot-injection method, in which an anionic source is injected into a cationic precursor at high temperatures (120-320°C) under inert conditions, forming nanocrystals that are stabilized in solution by coordinating ligands attached to the QD surface [12]. A schematic of a typical hot injection set-up is presented in **Figure 1.5**. Control over the size and shape of the QD can be attained by manipulating the reactions conditions, such as reaction time, temperature [23], choice of coordinating ligand [29], and reactivity of precursor.
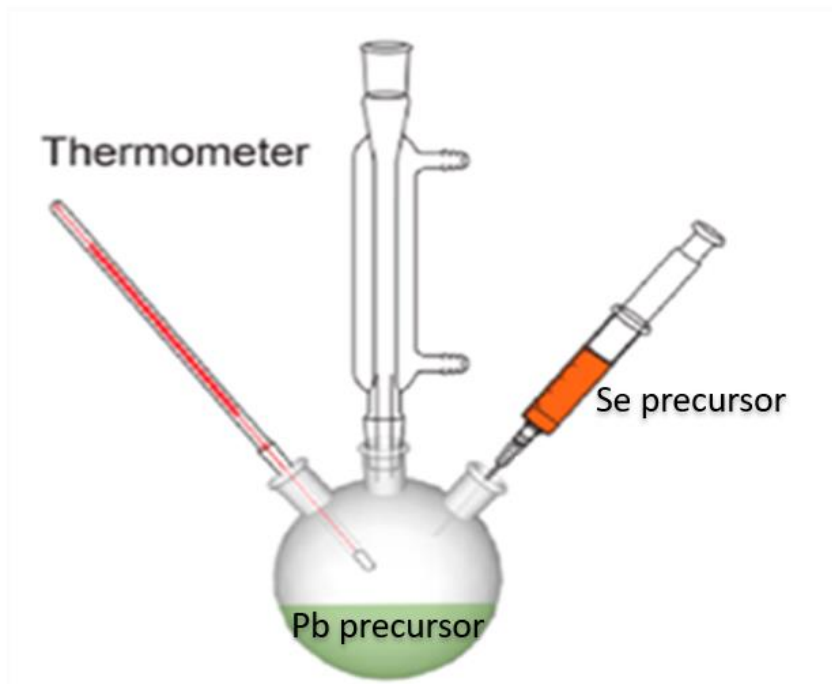
Figure 1.5 Schematic of a typical hot injection set up for PbSe QD synthesis

Generally there are two common colloidal synthesis routes used for PbSe QD synthesis, the

carboxylate route [30] and the amine route [31,32]. In the carboxylate-based synthesis lead oxide

(PbO) is combined with oleic acid (OA) and high boiling point solvent, typically 1-octadecene

(ODE), in a flask and degassed at ≈120°C in order to remove excess water from the solution.

After degassing, the solution is put under inert atmosphere, either Argon or Nitrogen, and set to a

temperature based on desired QD size, with higher temperatures resulting in larger QDs. When

the desired temperature is reached a solution of tri-n-octylphosphine selenide (TOPSe) and a

secondary phosphine such as di-i-butylphosphine (DIP) is swiftly injected into the reaction flask.

The secondary phosphine acts as a reducing agent, lowering the threshold for nucleation, causing

the reaction to occur more rapidly, as well as increase the yield of PbSe QDs [33]. After initial

nucleation there is a growth phase in which the QDs grow larger overtime, during this stage, the

monomer concentration is too low to generate new nuclei but still beyond the solubility limit in

the solvent, resulting in the excess monomer depositing on to the existing nuclei [34,35]. Reduction

of temperature after initial injection reduces the chances of secondary nucleation and allows the

QDs to undergo size focusing while the monomer concentration is still above the solubility limit,

as the smaller QDs are more reactive and will be more receptive to the free monomers in the

solution. However, as the monomer concentration is decreased toward the solubility limit, the

rate of precipitation and dissolution are balanced, resulting in a size defocusing regime, known as

Ostwald ripening, in which the smaller particles dissolve faster than the larger particles.

Therefore, it is important to balance time and temperature during QD synthesis, as one wants the

particles to grow long enough to become monodisperse but not too long as this will hurt the size

distribution.

The amine route undergoes similar reaction kinetics as the carboxylate route, however rather

than using oleate as a coordinating ligand oleylamine (OLA) is used instead. The Pb source in

the amine route is a PbX_2 (X = Cl, Br, or I), while the other reaction variables are the same. The

stabilizing ligand, oleate or OLA, on the surface of PbSe QDs causes the QDs to remain

colloidally stable even after multiple purifications and re-dispersions. Purification of colloidal

PbSe QDs is typically accomplished by addition of polar solvents into a solution of QDs

dispersed in a non-polar solvent, resulting in a slurried dispersion of QD precipitates that can be

separated via centrifugation. After centrifugation the supernatant can be removed and QDs can

be re-dispersed in solvent of choice; depending on surface chemistry, QDs will be dispersible in

either non-polar or polar solvents. Choice of anti-solvent used during purification can have

significant effects on the surface chemistry QDs, leading to negative consequences to QD

properties, specifically photoluminescence quantum yield (PLQY). Protic solvents such as

methanol and ethanol, can strip tightly bound X-type ligands [36], such as carboxylates, from the

surface of QDs by way of a proton transfer reaction from the solvent to the ligand. The greater acidity of methanol results in this proton transfer occurring more readily, leading to greater surface ligand stripping and in turn lower quantum yields compared to QDs purified with ethanol. However, the use of an aprotic solvent such as acetonitrile (ACN) does not induce stripping of surface ligands, resulting in QDs with greater surface ligand coverage and in turn higher PLQY. More weakly bound L-type ligands, such as OLA, are even more susceptible to stripping and QDs synthesized with these ligands must be purified with aprotic solvents in order to maintain colloidal stability [36].

1.3 Air stabilization of PbSe QDs

Pristine PbSe QDs are prone to surface oxidation, which causes a decrease in the PLQY as well as introduces surface trap states which can hinder transport in QD films [37]. In order to protect the surface of PbSe QDs from oxidation many techniques have been developed such as; passivation of the surface with an inorganic shell (*i.e.* CdSe) through cation exchange [38] and passivation with molecular chlorine [22]. Cation exchange is a technique in which Pb^{2+} cations on the surface of PbSe QDs are replaced by Cd^{2+} cations in the presence of excess cadmium oleate. The replacement of Pb^{2+} cations results in the PbSe "core" shrinking which is accompanied by a blue shifting in the PL peak. **Figure 1.6** shows a schematic of the cation exchange process, as well as an example of the absorption spectra of PbSe QDs left in air with and without passivation of molecular chlorine. Colloidal atomic layer deposition (C-ALD), a technique in which a shell is grown in sequential self-limiting reactions [39], which results in the deposition of either anionic or cationic molecules on the surface, has also been utilized. However, C-ALD typically does not result in an increase in PLQY of Pb based QDs in the same way that cation exchange does due to the low temperature of the reaction causing defects between the core and shell [40].
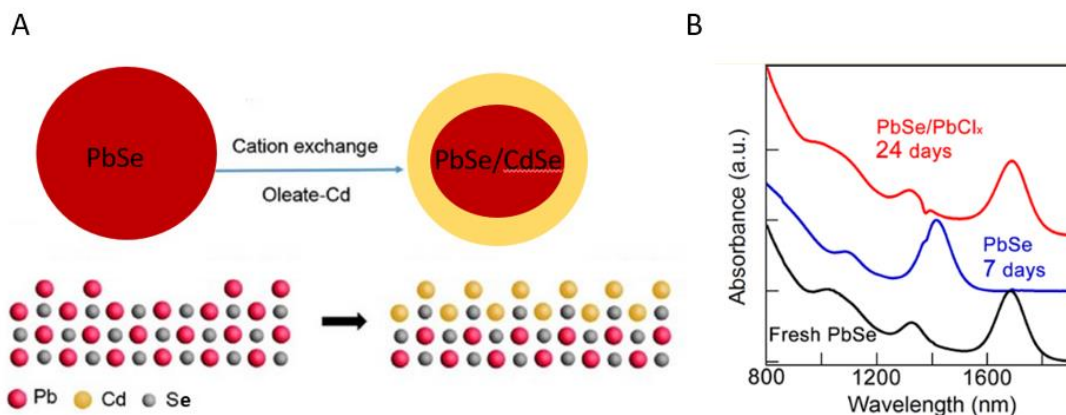
Figure 1.6 (A) Schematic of the cation exchange process, figure modified from reference [41]. **(B)** Absorption spectra of fresh PbSe QDs as well as PbSe stored in air for 7 days without chlorine passivation and PbSe QDs stored in air for 24 days with chlorine surface passivation. The lack of blue shifting in the absorption spectra indicates that surface oxidation has been suppressed. Reprinted from reference [22]

Additional shell growth after cation exchange through successive ionic layer absorption reaction (SILAR) is a common way to improve the photo-stability PbSe QD cores even more. SILAR is a method that involves adding precise amounts of anionic and cationic precursors [42], to grow a shell in half mono-layer steps, similar to C-ALD. SILAR and modified SILAR growth methods have been employed to grow thick CdS shells onto PbSe/CdSe core/shell QDs, resulting in ultra-long carrier lifetimes [43]; the growth of additional layers of CdSe onto PbSe/CdSe structures using Se in ODE precursor resulted in giant core/shell QDs that were stable enough for single dot measurements [44]. However, SILAR does not employ self-limiting reactions which causes the possibility of homogeneous nucleation of unwanted sub ensemble particles if precursor addition amounts aren't accurately calculated. Proper precursor amounts can be

calculated by using **Equation 1.3** to calculate the diameter of a single PbSe QD based on the position of the first peak in the absorption spectra [16].

$$D = \frac{\lambda - 143.75}{281.25}$$ *Equation 1.3*

Where D is the diameter of the QD in nm, and λ is the first absorption peak in nm as well. The molar extinction coefficient of PbSe particles can be calculated from **Equation 1.4**:

$$\varepsilon = 0.03389 * D^{2.53801}$$ *Equation 1.4*

Where ε is the molar extinction coefficient with units of $10^5\,M^{-1}\cdot cm^{-1}$, and D is the diameter calculated for **Equation 1.3.** The accuracy of the ε value in **Equation 1.4** can be greatly affected by the size distribution of the QDs within an ensemble, because broader size distribution will result in broader peaks in the absorption spectra as well as lower absorption values at the true peak position[16]. The concentration of in mol/L of PbSe QD solutions can then be calculated by rearranging the Beer-Lambert law to solve for C, as presented in **Equation 1.5.**

$$C = \frac{A}{\varepsilon L}$$ *Equation 1.5*

In **Equation 1.5**, A is the value of the absorbance of the first peak in the absorption spectra and L is the length of the optical path in cm. A more useful form of concentration for working with QD solutions is mg/mL, which can easily be calculated by first converting to QD/mL by multiplying by Avogadro's number ($6.02*10^{23}$) and dividing by the amount of mL in a liter. The mass of a single QD can be found by converting the diameter into a volume (mL) with **Equation 1.6**, which can then be converted into mass (mg) by multiplying by the bulk density of PbSe (8100 mg/mL), **Equation 1.7.**

$$V = \left(\frac{4\pi/3}{\frac{D}{2}}\right)^3 * 1^{-21} \qquad\qquad Equation\ 1.6$$

$$mass = V * 8100 \qquad\qquad Equation\ 1.7$$

The above equations assume that the QD is a perfect sphere, and that PbSe QDs are stoichiometric in composition. While PbSe QDs are generally slightly off stoichiometric due their Pb rich surfaces [16] these assumptions are still valid to calculate QD concentration within a reasonable error. Once QD size and the concentration of solution are known, the number of atoms (n) in the QD as well as the amount of surface atoms (n_s) can be calculated to determine the amount of precursor needed for the first layer of SILAR growth with **Equations 1.8 and 1.9.**

$$n = \frac{4\pi * \left(\frac{D}{0.612}\right)^3}{3} \qquad\qquad Equation\ 1.8$$

$$n_s = 4 * n^{-1/3} \qquad\qquad Equation\ 1.9$$

In **Equation 1.8** the value of 0.612 is in units of nm which is equal to the lattice constant of PbSe QDs which have a rock salt crystal structure. The amount of precursor solution to be used for each additional layer grown by the SILAR method should be calculated assuming that a perfect uniform half monolayer shell was added by the previous iteration.

1.4 Quantum Dot Films

The fabrication of QD solids in the form of a film can be accomplished by various solution processing techniques such as; spin-coating [45,46], dip-coating [47], doctor blading [48], and inkjet printing [49]. The creation of QD solids from semiconductor QD building blocks is dictated by the composition, size and shape of the QDs, and their spacing and organization in the solid [50]. Synthesis of highly monodisperse QD ensembles is the first step in realizing the possibility of "band like" transport in QD films, as this would contribute to denser packing with less defects,

increasing the likelihood that the electronic wavefunctions of the individual electronic states would overlap to form an extended state as indicated in **Figure 1.7.** However, QDs are far from ideal building blocks, as the best colloidal synthesis procedures still have size distributions of 3-5% within an ensemble, slight composition change from dot to dot is inevitable, and differences in surface chemistry are certain.
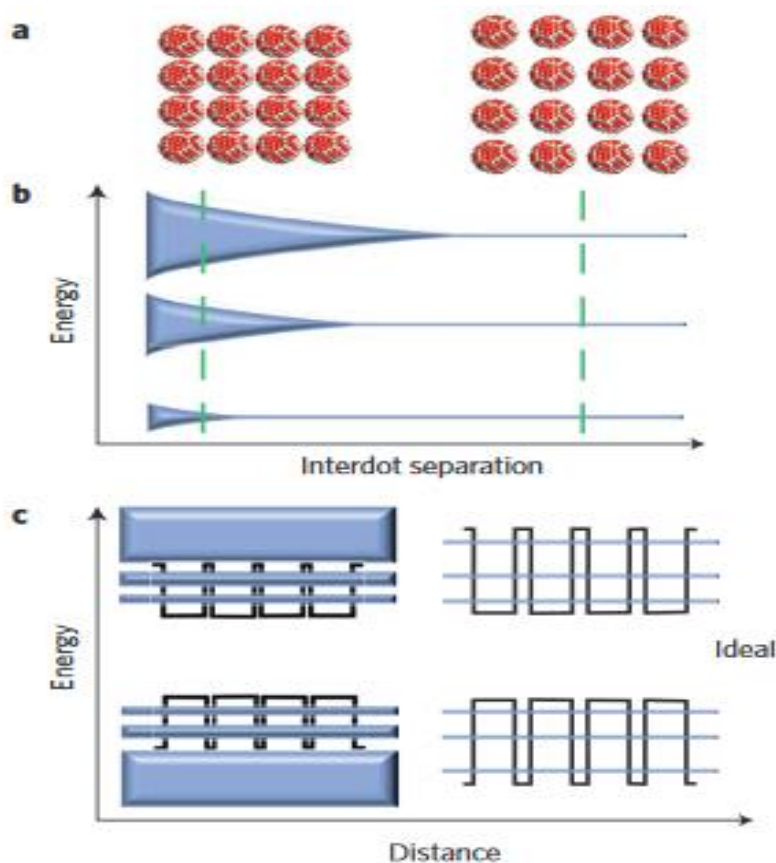
Figure 1.7 (A) A schematic of QD spacing within a QD film. **(B)** Visual representation of the progression from discrete to extended electronic state formation as inter-dot spacing is decreased and wavefunctions overlap more. **(C).** Schematic of the electron and hole states in a QD film, as the QD spacing becomes closer the electronic states of the solids start to form bands. Reprinted from reference [50].

Preparation of quality QD films has long been a hindrance to fabricating QD devices because the long ligands attached to their surface, which are vital for colloidal stability, act as insulators to carrier transport when QDs are incorporated into a film[46,51]. Layer-by-layer ligand exchange employed during QD film preparation, in which long native ligands in a thin QD film are replaced by shorter ligands through exposure to a solution containing more strongly binding short ligands, was an early solution to improve QD spacing issues within films [46,52]. However, layer-by-layer ligand exchange is only successful if the QD film is sufficiently thin to allow complete solution penetration and can result in non-uniform films, as it is performed repeatedly when producing a thicker films. For many applications, such as simple photodetectors, thin films are sufficient because PbSe QDs are very strong absorbers, but thick films (>300 nm) are important for solar cells and detection of higher energy photons such as X-rays and gamma rays.

In 2017 Lin *et al.* [32] introduced a universal method for in-solution ligand exchange of PbSe QDs with short ionic ligands, allowing for the deposition of thicker films and removal of post deposition ligand exchange step as shown in **Figure 1.8**. PbSe QDs were synthesized using the amine route, which results in Pb rich surfaces with OLA ligands, which are more weakly binding than oleate ligands, promoting facile exchange from OLA to shorter ionic ligands through a phase transfer reaction using polar solvents in which the ionic ligands were dissolved. The use of 2,6-diflouropyridine (DFP), which is a polar solvent with a relatively low boiling point (124°C) and a higher dielectric constant (107.8) [53], as a solvent for PbSe QDs capped with shorter ionic ligands is ideal for creating thick films in a single deposition step.
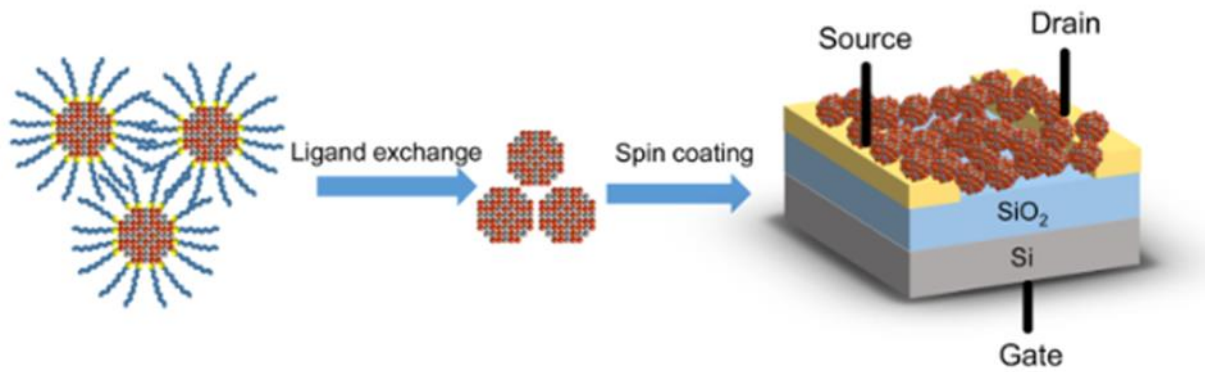
Figure 1.8 Schematic of PbSe QDs undergoing ligand exchange to shorter ionic ligands and subsequently being incorporated into a film with close QD spacing without the need for additional post deposition ligand exchange steps. Reprinted from reference [32]

The surface chemistry of QDs plays a vital role in carrier transport through QD films, affecting inter-dot spacing, passivating surface trap states [54], and altering the band alignment [55,56]. There are several studies on the effect of surface chemistry on energy-band positions in QDs, indicating that not only can the position of the valence band and conduction band positions be altered by surface chemistry, but the Fermi level can be affected as well [56]. The type of carrier transport, *n*-type or *p*-type, can also be altered by changing the surface chemistry, allowing for the possibility of tailoring QDs for a specific device or function within a device. Treating the surface of a QD film with chemicals such as hydrazine [57] or ethanedithiol [58] can produce *n*-type and *p*-type behavior, respectively, by introducing charges into surface trap states. While a more persistent introduction of charges can be achieved by introduction of a reducing agent, such as cobaltocene, which leads to higher electron concentrations being generated within the QD film thus making the films more conductive [21].

Control over carrier concentration is very important for achieving maximum performance in electronic devices, because it allows the ability to control charge carrier behavior [21]. Each device has a different ideal situation when it comes to carrier concentration, for instance solar cells prefer a higher carrier concentration because it can make forming *p-n* junctions easier, while in detectors this may lead to more non-desirable noise. Deposition of additional Pb cations on the surface of PbSe QD films has been shown to increase the electron density in films, while additional Se anions increases the hole density [59,60].

Minimizing recombination of carriers before collection is paramount to maximizing the device efficiency and detector accuracy. There are many possible approaches for maximizing the amount of information collected and in turn minimizing information/energy lost in a device, including altering the device architecture to minimize the amount of distance the carrier must travel before it is collected. This could be accomplished by fabricating devices with inter-digitated electrodes [61] where the QDs and collection electrodes form alternating layers, in which the carriers could be generated and then almost immediately collected by the nearest electrode. However there are also methods for increasing the carrier diffusion length within the QD film, including partial fusing of QDs. Fusing of certain facets of the QDs, combined with effective passivation of non-fused facets, allows for easier transport of carriers among the somewhat interconnected solid, while still maintaining some degree of quantum confinement [62].

Additional post deposition treatment of PbSe QD films such as atomic layer deposition (ALD) infilling or encasing with alumina can improved the resiliency of QD films to air, as well improve carrier mobility by inflling gaps within the film [63-65]. ALD treatment of PbSe QD films has also shown the potential to unlock carrier multiplication [66] within the film, providing a road

map for harnessing one of the desirable properties of PbSe QDs, which was previously only observable in QDs in solution, in devices.

1.5 Overview of Dissertation

This dissertation focuses on the synthesis of PbSe based heterostructured QDs including PbSe/CdSe, giant PbSe/CdSe/CdSe, and PbSe/CdSe/CdS structures, as well as implementation of PbSe QDs into simple devices for film property characterization. Chapter 2 uses PbSe/CdSe core/shell QDs as the basis for creating more complex structures such as giant-PbSe/CdSe/CdSe QDs through the additional growth of CdSe via direct shell growth techniques. PbSe/CdSe/CdS structures of various sizes and shapes including tetrapods with CdS arms and triangular or pyramidal shaped nanocrystals with long carrier lifetimes are also synthesized, with the effect of intermediate CdSe shell thickness as well as reaction temperature playing an important role in the final structure of the nanocrystal.

In Chapter 3 PbSe based QD devices, fabricated using exclusively in-solution ligand exchanged PbSe QDs, are studied for the effect of ligand type on carrier mobility as well as carrier density. A broad range of mobilities and carrier densities for films of PbSe QDs of the same size are realized as a result of varying only the surface ligand. The effect of PbSe QD size on both electron and hole mobility in NH_4I capped PbSe QDs is also examined. Sensitivity of PbSe QD films to radiation such as alpha particles and gamma rays is tested to determine feasibility of room temperature solid state radiation detectors comprised PbSe QDs.

Chapter 4 is a critical review of an emerging class of photodetectors, which aim to combat the relatively low carrier mobilities in QD films by combining them with layered 2D materials. These hybrid 2D-0D detectors utilize materials such as graphene and MoS_2, which have reported carrier mobilities at least 2 orders of magnitude greater than those currently feasible in Pb based

QD films. The combination of these two types of materials combines the high mobility of 2D materials with the strong size tunable absorption of QDs to fabricate photodetectors that display high gain and tunable detection ranges.

Chapter 2: Core/Shell PbSe/CdSe Quantum Dots

2.1 Introduction

Synthesis of core/shell structures has become an omnipresent technique in the field of colloidal QDs for improving QD stability and PLQY [38,67], manipulating carrier recombination dynamics [28,43], and altering bandgap energies [68,69]. Compared to core only or thin-shell QDs, growth of a thick shell, or "giant" QDs, can lead to many desirable properties such as, non-blinking single QD emission [70], suppressed Auger recombination [71,72], and large stokes shift between PL and the onset of strong optical absorption. The nature of the interface between the core and shell plays an important role in influencing the optical behavior. Generally, there are two types of interfaces as, shown in **Figure 2.1**, type I where the conduction band of the shell is higher than that of the core, and the valence band of the shell is lower than that of the core. Type II interfaces are where the conduction and valence bands of the shell are both higher (or lower) that that of the core.
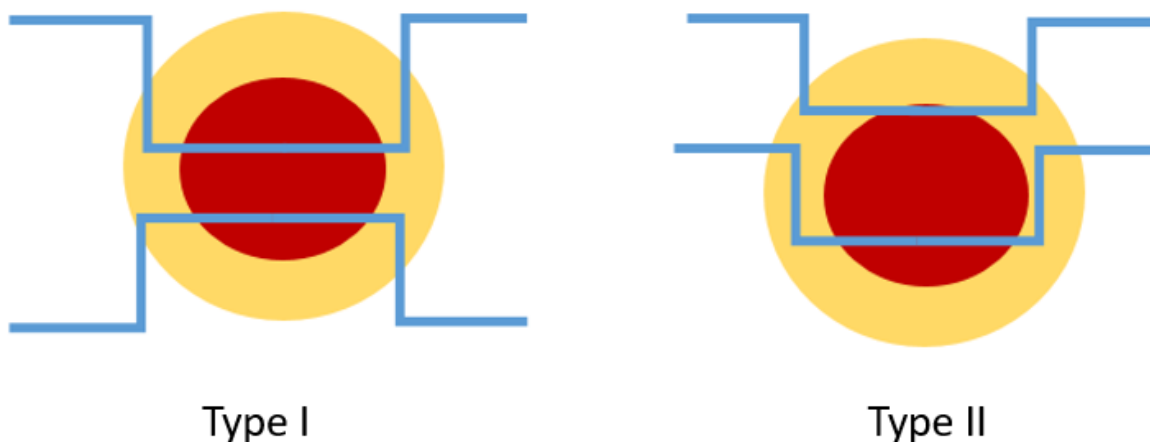
Figure 2.1 Schematic of the type I and type II band offsets in core/shell QDs

In QDs with type I band alignment the electron and hole are strictly confined in the core, which serves as potential wall to decrease non-radiative decay such as thermal relaxation of exciton to the environment. In QDs with type II band alignment either the electron or hole is confined in the core while the other is confined in the shell, which results in a loss in absorbed energy and leads to longer exciton lifetimes. Based on these two types, other types of band alignment are possible with inversed type I structure, in which the electron and holes are confined in the shell, and quasi type II structure, in which electron (or hole) is delocalized through the whole particle, while the other is localized in the core (or shell).

Direct synthesis of core/shell structures usually requires high stability of core QDs at the shell growth temperature, which is typically well above 200°C for Cd based shells [73]. PbSe QDs do not have good stability at high temperatures, so an alternative way to prepare PbSe/CdSe core/shell QDs was achieved by cation exchange from pristine PbSe QDs in the presence of cadmium oleate precursor by Pietryga et al. in 2008 [38]. The lattice energy of PbSe and CdSe was believed to be the driving force for the partial replacement of lead ions with cadmium ions. In 2015 Lin *et al.* showed that as the CdSe shell becomes sufficiently thick (≈7 monolayers) visible emission, **Figure 2.2 (A),** from the shell can be observed as a result of slowed carrier cooling [74]. Shell thickness as a result of cation exchange was shown to saturate after 16 hours at a certain temperature, only continuing if temperature was increased, as shown in **Figure 2.2 (B)**, however long periods of time at a temperature of 200°C resulted in smaller unwanted CdSe particles forming, as can be seen is **Figure 2.2 (B)**. The visible emission from the CdSe shell was observable even when excited with low intensity light sources, however the PLQY was very weak with values on the order of 0.01%.
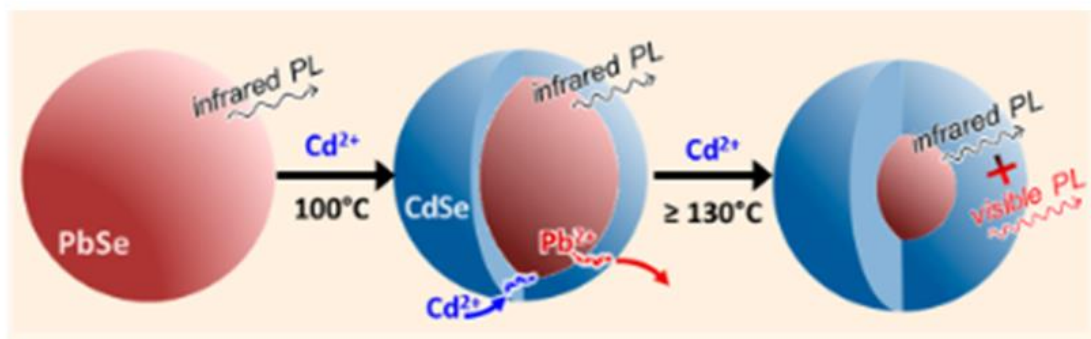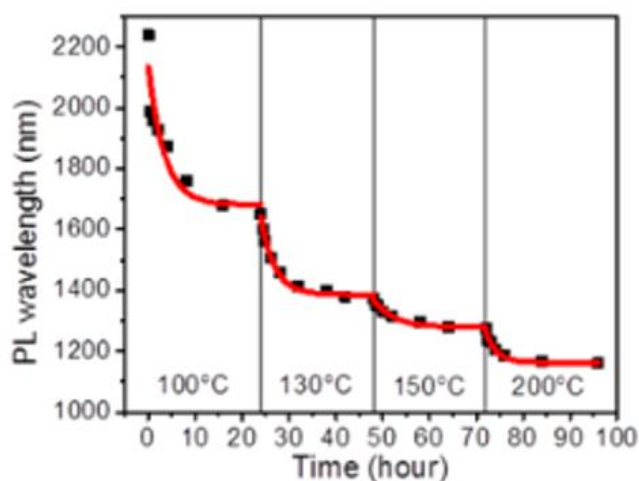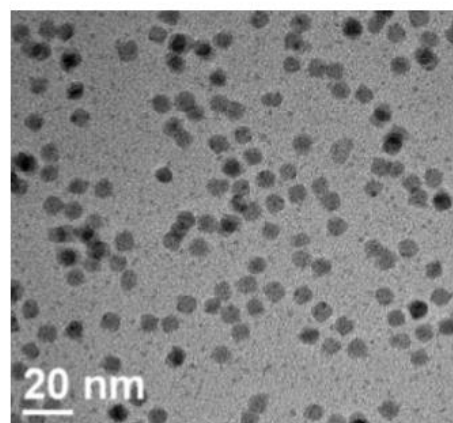
Figure 2.2 (A) Schematic of cation exchange in PbSe/CdSe QDs, as shell becomes sufficiently thick visible emission becomes observable. **(B)** Graphical representation of the blue shifting in PL peak position, as a result of CdSe shell thickness increasing, as a function of time and temperature. **(C)** TEM image of PbSe/CdSe QDs held at 200°C for 18 hours, notice the sub ensemble of smaller CdSe particles. A and B reprinted from reference [74], C reprinted from reference [28].

Auger assisted up-conversion in dual emitting QDs is a process in which excitation with lower energy photons, which can only be absorbed by the PbSe core, results in emission from the visible shell via a coulomb interaction between 2 electrons that were simultaneously excited into an intermediate state, resulting in one electron being promoted into the shell state and the other

relaxing back to the core state [28]. Auger assisted up-conversion is essentially the inverse process of carrier multiplication (CM), which has been shown to be enhanced in thick shell PbSe/CdSe QDs [26], and should therefore be more easily accomplished in these structures as well. Auger assisted up conversion is also more efficient and requires less intense excitation than other typical methods of up-conversion, such as non-linear 2 photon absorption and stepwise 2 photon absorption, shown in **Figure 2.3**, making it interesting for the prospects of increases QD solar cell efficiencies. PbSe/CdSe QDs can be tailored to be up-converting materials or carrier-multiplying materials by engineering the difference between the visible and NIR PL peaks. Core/shell QDs with a NIR emission peak (E_2) of wavelength less than double that of the visible emission peak (E_1) display higher up-conversion efficiencies. This is due the lowest energy required to excite a band-edge hole from the core to the shell being defined as $\Delta_{c\text{-}s}=E_2-E_1$. Based on energy conservation, for Auger up-conversion to occur, $\Delta_{c\text{-}s}$ should be less than or equal to the energy released in the recombination of a core-based exciton. On the other hand, the opposite condition, $\Delta_{c\text{-}s} \geq E_1$ or $E_2 \geq 2 E_1$, should be satisfied to make CM the desired relaxation pathway [28].
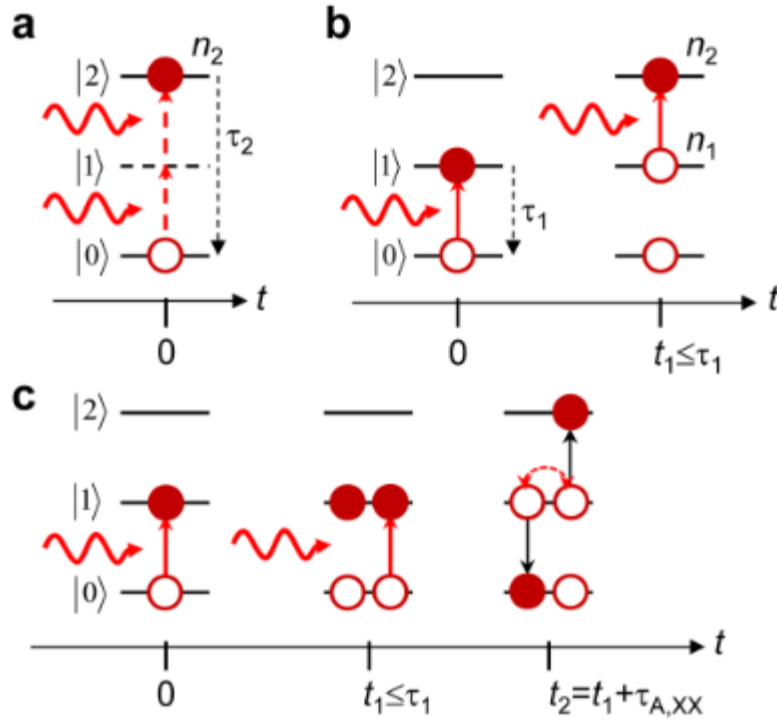
Figure 2.3 (A) Schematic of nonlinear 2PA, an electron is promoted from the ground state (solid black line labeled as$|0\rangle$) to an excited state (solid black line labeled as$|2\rangle$ state) via a virtual intermediate state (dashed black line denoted as$|1\rangle$) by simultaneously absorbing two photons (red wavy arrows). This process involves two virtual transitions (dashed red arrows) to generate electrons into the higher state (n_2 is the average per-dot occupancy) characterized by lifetime τ_2. **(B)** Stepwise 2PA involves a real intermediate state (average per-dot occupancy n_1 and lifetime τ_1) and two real optical transitions (solid red lines): one couples the initial to the intermediate state and the other the intermediate to the final state. In this process, the absorbed photons can be separated by a time interval on the order of $\tau_1$or less. **(C)** In Auger up-conversion, two electrons are excited into the intermediate state via sequential absorption of two photons. A Coulomb interaction between the electrons (dashed red arc arrow) triggers an Auger process (characteristic time $\tau_{A,XX}$) whereby one electron is promoted into the final state while the other returns to the initial state. Reprinted from reference [28]

25

Theoretically Auger up-conversion could be further enhanced by thicker CdSe shells because the increased aspect ratio (ratio of shell thickness to total QD radius), is beneficial to the process. However, growth of thicker CdSe shells is hindered by the nature of the cation exchange reaction, which is strongly dominated by growth on the {111} facets of the QD [75] . As PbSe particles become larger (D ≈ 10 nm), they begin to change from spherical in shape to cubic resulting in a reduction of the prevalence of the {111} facets. Accordingly, cation exchange does not readily occur in cubic PbSe QDs as shown in **Figure 2.4**. Therefore, cation exchange is only viable in smaller particles, and under high temperature conditions unwanted side effects such as complete exchange or formation of CdSe sub ensembles can occur.
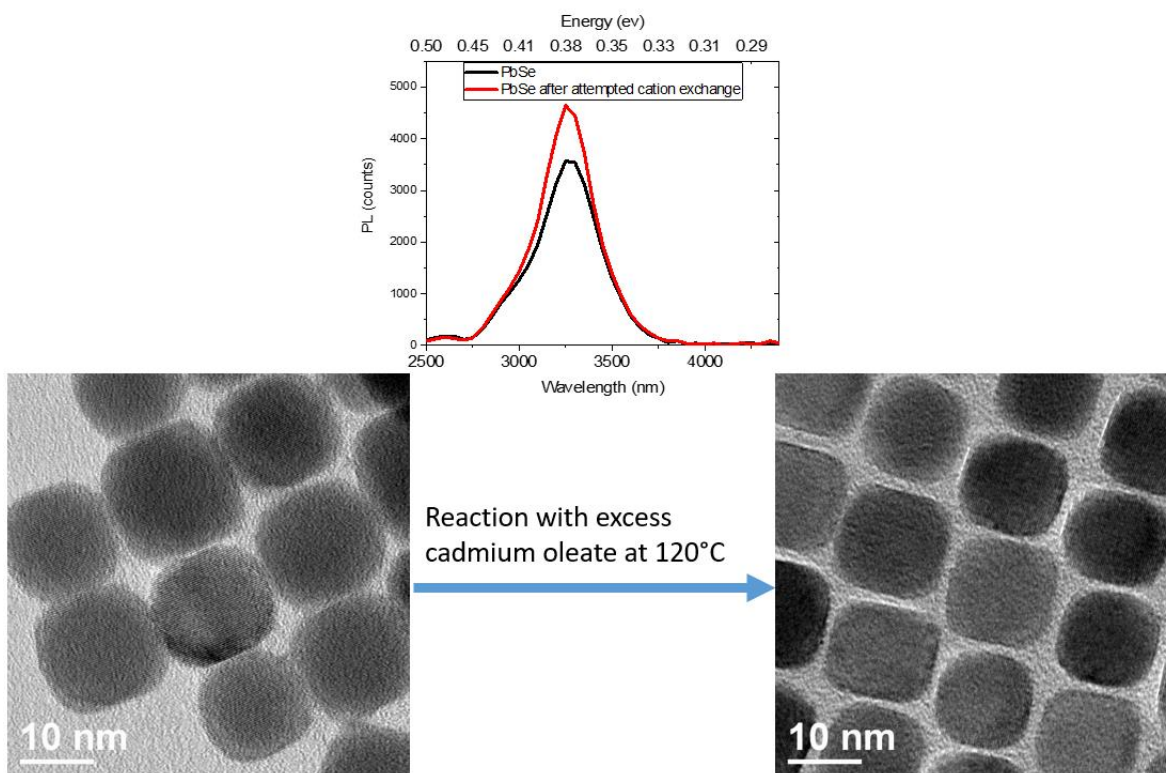
Figure 2.4 (Top) PL peak of large mid-IR emitting PbSe QDs before and after attempted cation exchange (notice a lack in blue shifting of the PL, indicating a lack cation exchange) (Bottom) TEM images of PbSe QDs before and after treatment with CdOA at a temperature of 120°C, no noticeable shell formation is visible.

A method for growing thicker CdSe shells, is the utilization of partial cation exchange to form the initial CdSe shell followed by direct growth via modified SILAR method to increase shell thickness [44]. Initial CdSe shell thickness is an important variable in the process of the secondary shell growth because it can determine the shape of the secondary shell [44], and it acts as a protective layer for the PbSe core which is susceptible to structural deformation at high temperatures. The type of Se precursor (Se in ODE or TOPSe) utilized during secondary shell growth dictates the crystal structure of the outer CdSe shell. Se in ODE results in zinc blende crystal structure and large cubic particles, suggesting an influence of the core on crystal growth, while TOPSe results in the more common wurtzite crystal structure for the CdSe outer shell.

Increasing PLQY in the visible regime for dual emitting PbSe/CdSe QDs is an area that has not been extensively studied. Shelling with sulfides with larger band gaps, such as CdS [42,76] and ZnS [77], has been a common approach to increase quantum efficiencies in visible emitting QDs, however studies on PbSe/CdSe/CdS heterostructures thus far have focused more on the effects of IR PL efficiencies and IR exciton lifetimes [43]. Lin *et al.* showed that a thin layer of CdS or ZnS on top of PbSe/CdSe QDs led to a 4 fold enhancement of the visible PL, however this procedure was not optimized and only mentioned in passing [74]. Herein we more closely exam the effects of CdS and CdSe shell growth on visible PLQY enhancement as well as the possibility of improved Auger up-conversion due to higher PL efficiency and aspect ratio.

2.2 Experimental Methods

Materials. Oleic acid (OA, technical grade 90%), lead(II) oxide (99.999%), selenium powder (99.99%), and selenium shot (99.999%) were purchased from Alfa Aesar; 1-octadecene (ODE, technical grade 90%), sulfur (99.5%), cadmium oxide (99.998%), tri-n-octylphosphine

(TOP, 90%), octadecylamine (ODA, 97%), and oleylamine (OLA, 90%) were purchased Sigma

Aldrich; di-i-butylphosphine (DIP, 97%) was purchased from Strem.

Stock solutions and precursors for additional shell growth: Stock solution of 2M TOPSe

was prepared in an inert glovebox overnight by mixing 10 mL TOP with 20 mmol Se shot in a

vial on a hot plate at moderate heat. 0.1M Se suspension (SeSUS), for additional CdSe shell

growth was prepared by sonicating 1 mmol Se powder in ODE for a minimum of 10 minutes.

0.1M Se in ODE, for additional CdSe shell growth was prepared by reacting 1 mmol of Se shot

with 10 mL of ODE at 270°C under inert atmosphere until Se shot was dissolved and the

solution turned yellowish in color. For CdS shell growth 0.1M S in ODE was prepared by

dissolving 1 mmol of S powder in 10 mL of under vacuum at 110°C. CdOA at a concentration of

0.1 M was prepared by degassing 1 mmol CdO powder with 1 mL OA and 9 mL of ODE at

110°C under vacuum for 15 minutes, followed by raising the temperature to 250°C under inert

atmosphere until the solution turned clear. After the solution was clear the temperature was set

back to 100°C and degassing under vacuum for an additional hour.

Synthesis of PbSe QD cores: PbSe QDs were synthesized using the carboxylate synthesis

route. In a typical synthesis 4 mmol PbO + 4 mL OA + 10 mL ODE were loaded into a three-

neck flask and degassed under vacuum at 120°C for 30 minutes. After degassing, the three-neck

flask was placed under inert atmosphere and heating mantle was set to desired temperature,

based on the desired size of QD, for injection of Se precursor. Temperature of injection varies by

the desired size of QD cores. Temperature should be below 230°C as PbSe QDs begin to become

cubic in shape at a diameter of around 10 nm[23], and the cation exchange reaction involves

faceted growth which cannot occur when PbSe QDs are cubic. When desired temperature was

reached a solution of 1 mL 2M TOPSe + 1 mL TOP + 0.1 mL DIP was swiftly injected into the

three-neck flask, temperature is lowered by 20°C from injection temperature and reaction was allowed to proceed for 3 minutes. When reaction was complete the heating mantle was removed allowing the flask to come to room temperature, at which point the flask was transferred to an inert atmosphere glove box to be cleaned three times through addition of hexane and ethanol followed by centrifugation. After cleaning, QDs were re-dispersed in TCE; QD diameter and concentration of solution are calculated using *Equations 1.3-1.7*.

Cation exchange to synthesize PbSe/CdSe QDs: In a typical synthesis 5 mmol CdO+ 5 mL OA + 5 mL ODE were loaded into a three-neck flask and degassed under vacuum for 15 minutes at 110°C. After degassing, flask was put under inert atmosphere and temperature was raised to 250°C until the solution becomes clear. When solution is clear, temperature is returned to 110°C and degassed under vacuum for one hour. After degassing, solution was brought to room temperature and 100 mg of PbSe QDs in TCE is injected into the flask, after which the flask was degassed under vacuum to remove the solvent. After degassing, the flask was returned to inert atmosphere and temperature was set to reach the desired shell thickness, following **Figure 2.2**, and the reaction was allowed to proceed overnight. Purification of QDs was performed three times with a mixture of hexane and ethanol, and QDs were re-dispersed in TCE.

Synthesis of PbSe/CdSe/CdSe heterostructures: A three neck flask with 6 mL ODE and 1 mL OLA was degassed under vacuum at 100°C for 30 minutes. Following degassing the flask was returned to room temperature and ≈25 mg of PbSe/CdSe QDs in TCE was injected, followed by degassing to remove solvent. 2 growth temperatures were used for additional shell growth under inert atmosphere: 170°C for tetrapods and 240°C for cubic or spherical particles. Cubic particles were grown at 240°C synthesized using alternating injections or slow addition via syringe pump of either SeSUS or Se in ODE and CdOA, while spherical particles were

synthesized using TOPSe and CdOA. Amount of precursor used per injection was calculated by determining approximate amount of surface atoms per QD from *Equations 1.8-1.9.* Tetrapods were synthesized at 170°C using alternating injections of SeSUS and CdOA, allowing 10 minutes between each injection. Purification of nanocrystals was performed three times using a mixture of hexane and ethanol; on occasion OA must be added to the solution to improve colloidal stability.

Synthesis of PbSe/CdSe/CdS heterostructures: The synthesis method of spherical and tetrapod shaped PbSe/CdSe/CdS nanocrystal was similar to that described above for PbSe/CdSe/CdSe nanostructures; however rather than OLA, octadecylamine (ODA) was used as coordinating ligand and S in ODE was used for injections rather than Se.

2.3 Characterization Techniques

Transmission electron microscope (TEM) images were taken using a JEOL 2010 TEM, using QD samples drop cast from a dispersion onto carbon-coated copper grids. Absorption spectra were measured by a PerkinElmer Lambda 950 spectrophotometer. Near infrared (NIR) PL spectra were taken using a custom-built apparatus. Samples were excited using the mechanically chopped light from an 808 nm laser, and emission was spectrally dispersed using a grating monochromator and recorded using a liquid-N2-cooled InSb detector with lock-in amplification. Visible emission spectra were taken with a Flouromax-4 spectrofluorometer form Horiba at an excitation wavelength of 400 nm. The PL quantum yields (QYs) were determined relative to IR-26 (in 1,2-dicholorethane, QY = 0.048%)[78] for NIR emission and LD 690 (in ethanol, QY 63%) for visible emission. PL decay traces were measured using a superconducting nanowire single-photon detector (SNSPD)[27] with both 400 and 800 nm excitation, probing both visible and NIR PL peaks. Up-conversion measurements were performed using an 800 nm

pulsed laser and ocean optics for visible emission detection. To deconvolute two-photon absorption and Auger up-conversion processes, we used a two-pulse setup with a delay stage. At long time delays between pulses we should see a tail in up-conversion intensity that becomes independent of delay time.

2.4 Results and Discussion

2 types of heterostructured nanocrystals were synthesized, PbSe/CdSe/CdSe and PbSe/CdSe/CdS, with the CdS capped particles displaying stronger visible emission efficiencies. In general size selective precipitation was required to remove smaller CdSe and CdS particles that formed homogenously in the solution during the shell growth process. Visible emission spectra and TEM images showed that these particles were considerably smaller and could be easily removed with proper size selection techniques, with only a small sacrifice of desired products. **Figure 2.5** shows the effect of size selection in both TEM images and visible PL of a typical PbSe/CdSe/CdS tetrapod synthesis; tetrapod synthesis produced the most sub ensemble particles because the lower temperatures resulted in slower shell/arm growth. Since nanocrystals shelled with CdS displayed higher visible PLQYs, these particles were further examined for Auger assisted up-conversion. Visible emission was probed with normal pulsed laser excitation (800 nm wavelength), and through an experimental setup in which the sample was excited with 2 pulses with set delays between the pulses to check if the up-conversion deviated from linearity, which would indicate that Auger assisted up-conversion was indeed taking place rather than 2 photon absorption.
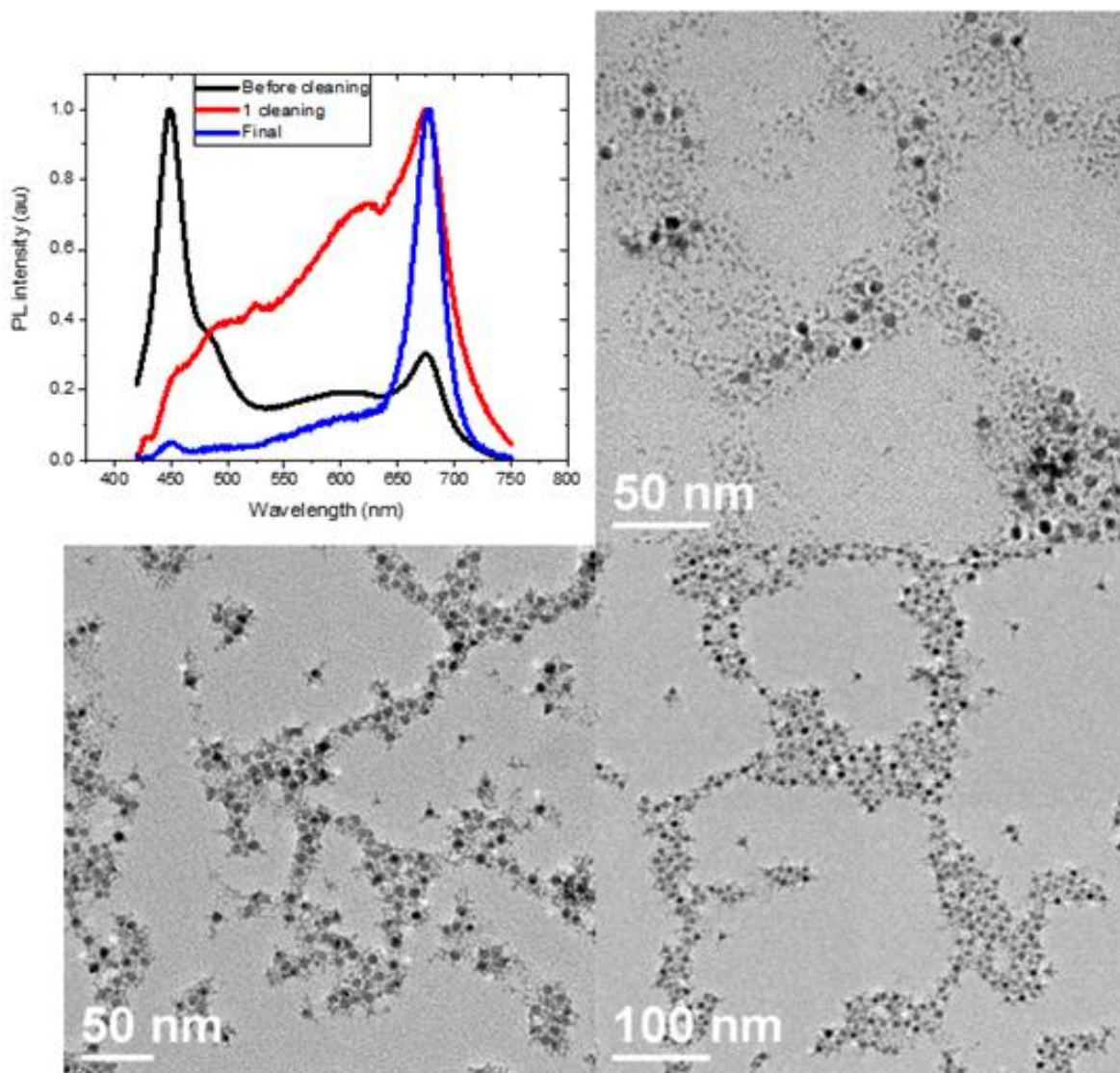
Figure 2.5 Progression of visible emission during size selection process when excited with 400 nm wavelength light of PbSe/CdSe/CdS. TEM images (right top) pristine sample no size selection (bottom left) after 1 size selection step (bottom right) final product.

2.4.1 Giant PbSe/CdSe/CdSe QDs

Tetrapods:

CdSe growth at 170°C using SeSUS and CdOA injections separated by 10 minutes to allow for complete absorption of Se and Cd precursors to the surface of the QDs showed results similar to those presented by Lee *et al.* for CdS growth [43]. Resulting particles were tetrapod

shaped with CdSe arms of ≈ 7 nm length, with NIR emission peaking at 1550 nm; no visible emission was observed. PLQY in the NIR dropped significantly from 5% to 0.4%, as well as blue shifted by ≈ 200 nm (≈ 86 meV), while the FWHM increased from 142 meV to 272 meV, indicating a broader distribution in core size. Absorption, PL spectra and TEM images are presented in **Figure 2.6**.
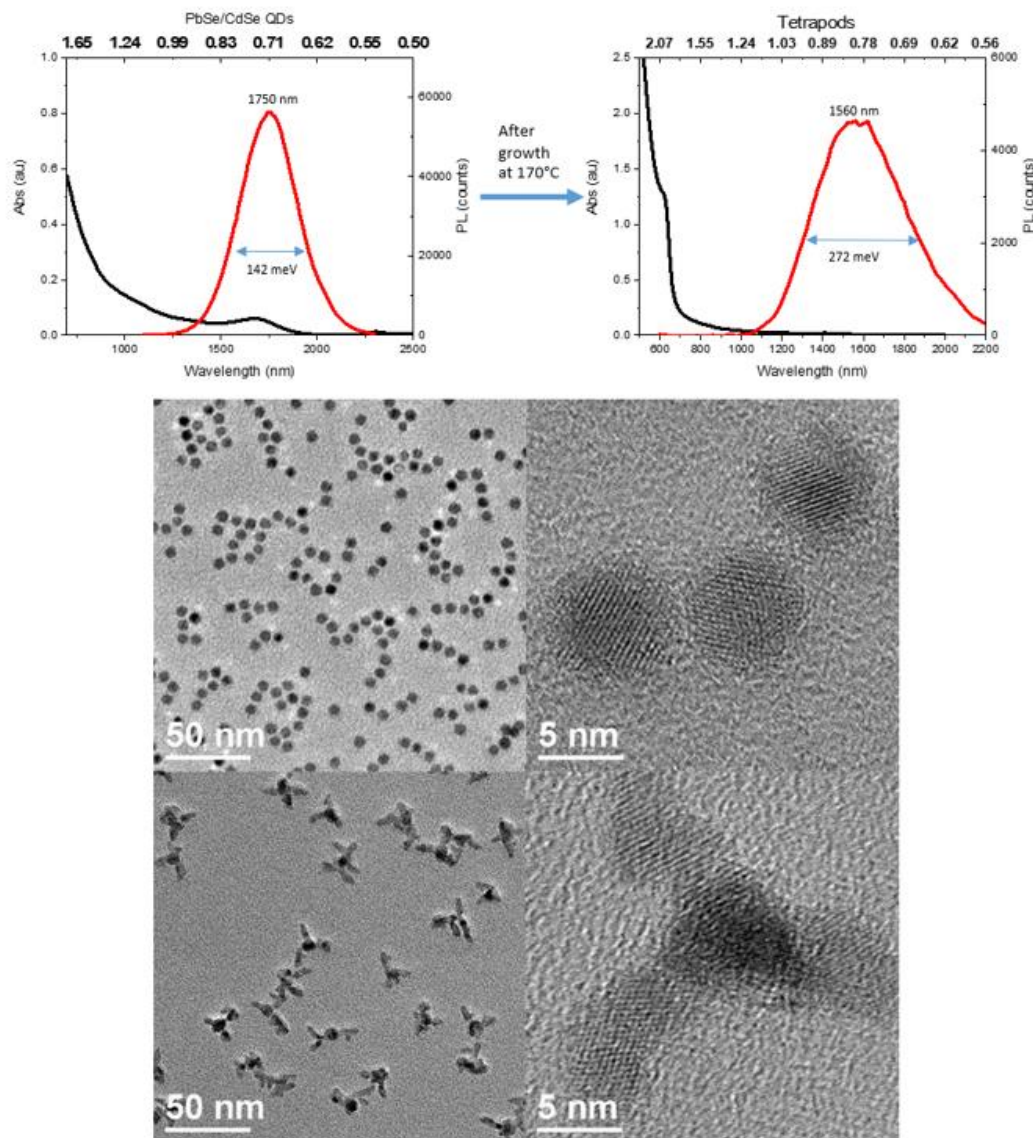
Figure 2.6 (Top) Absorption and PL before and after CdSe arms growth (middle) TEM images of PbSe/CdSe seeds (bottom) TEM images of PbSe/CdSe/CdSe tetrapods

Due to the lack of PLQY no further characterization of these particles was performed; rather, higher shell growth conditions, in an effort to make cubic nanocrystals, were employed.

Giant PbSe/CdSe/CdSe cubic nanoparticles:

Alternating injections of SeSUS and CdOA in 10 nm intervals resulted in PbSe/CdSe/CdSe QDs of cubic shape, **Figure 2.7**, indicating that the crystal structure of the CdSe outer shell is zinc blende, rather than the typical wurtzite structure.
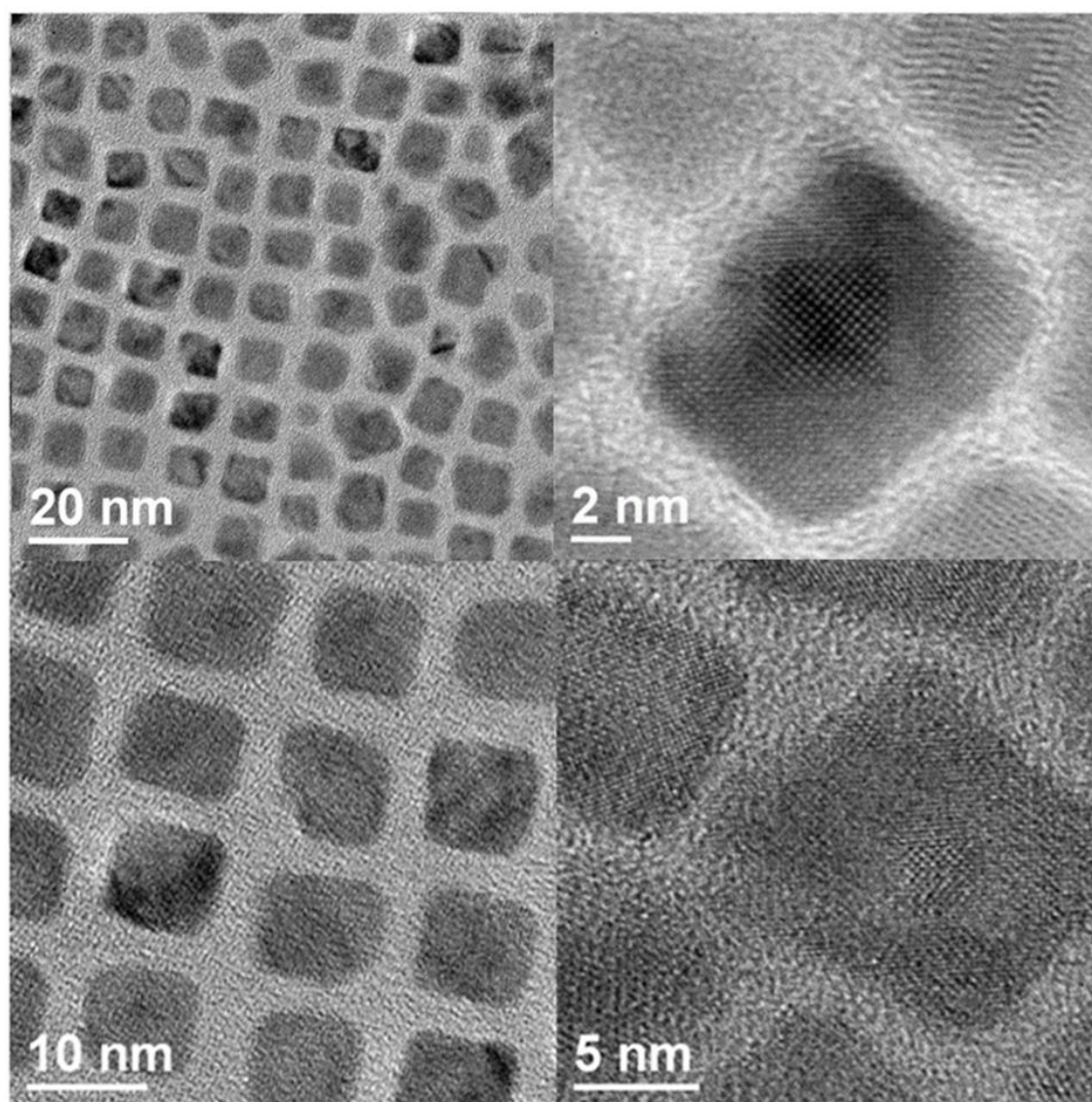
Figure 2.7 TEM images of cubic PbSe/CdSe QDs

Blue shifting of NIR emission during shell growth at higher temperatures is even more prevalent than growth at lower temperatures, indicating that thicker intermediate CdSe shells are required. NIR peak positions shifted from 1920 nm for PbSe CdSe seeds to 1260 nm for the final product, while the FWHM of the QDs increased from 109 meV to 424 meV. The large increase in FWHM as well as the asymmetrical shape of the PL peak, as seen in **Figure 2.8,** indicate a broad distribution in core size. QDs used for tetrapod and cubic nanocrystal synthesis were only subject to cation exchange at 90°C, in accordance with the report from Hanson *et al.* [44]. However, this results in CdSe shells with less than 1 nm of thickness, providing very little protection for PbSe cores.
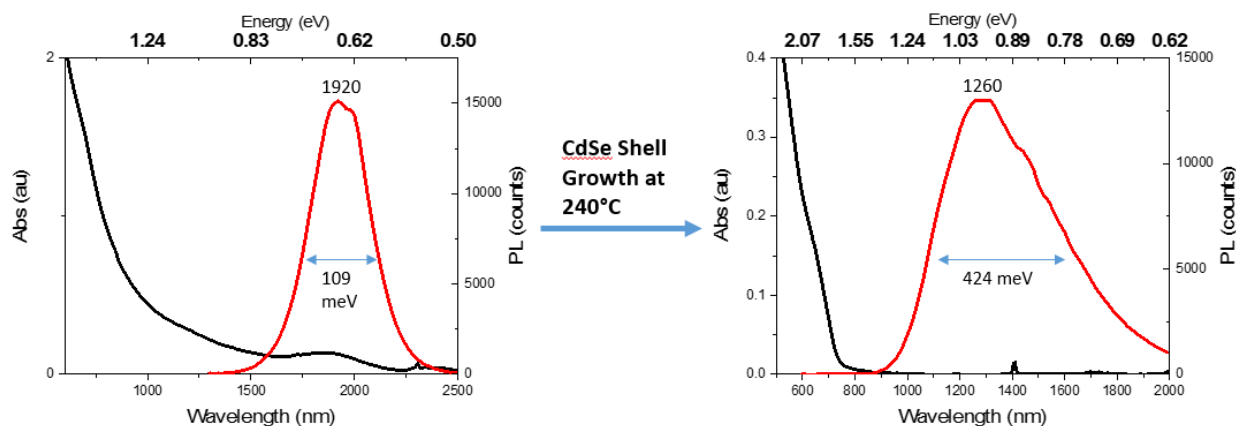
Figure 2.8 Absorption and PL spectra of PbSe/CdSe seed (left) and cubic PbSe/CdSe/CdSe QDs (right)

Cubic samples showed no visible emission, displayed NIR PLQY of 1.1%, and required significant size selection during purification to remove CdSe nanoparticles. The final products were roughly 10 nm in diameter with an average CdSe shell of 3 nm in diameter, however the broad PL peaks show that there is significant variance in these sizes. The abundance of unwanted CdSe particles could be a result of the physical properties of the SeSUS [79], which does not

completely dissolve into a homogeneous solution, resulting in possible measurement errors during precursor addition. Se shot completely dissolved in ODE, along with PbSe/CdSe seeds with thicker CdSe shell thickness were used to improve the synthetic procedure for cubic PbSe/CdSe/CdSe particles. Use of precursor that was completely dissolved and homogeneous throughout the solution allowed for the possibility of slow injection via a syringe pump rather than alternating injections.

Giant PbSe/CdSe/CdSe QDs:

Cation exchange to synthesize PbSe/CdSe QDs was performed overnight at a 100°C, resulting in a blue shifting of the PL peak from 2110 nm to 1750 nm and a shell thickness of roughly 1 nm. The PbSe/CdSe seeds do not show visible emission, however upon further shell growth visible emission begins to appear; see **Figure 2.9.** Visible emission of the final product was very weak, on the order 0.01%, similar to that reported by Lin *et al.* for thick shell QDs formed by cation exchange only. Further shell growth also induced a blue shift in the NIR PL peak from 1750 nm to 1220 nm, and the resulting QDs have PLQY in the NIR of 6.3% which is a significant improvement compared to the cubic particles displayed above. The FWHM of the PL peak was also drastically improved compared to cubes presented above from 424 meV to 238 meV.
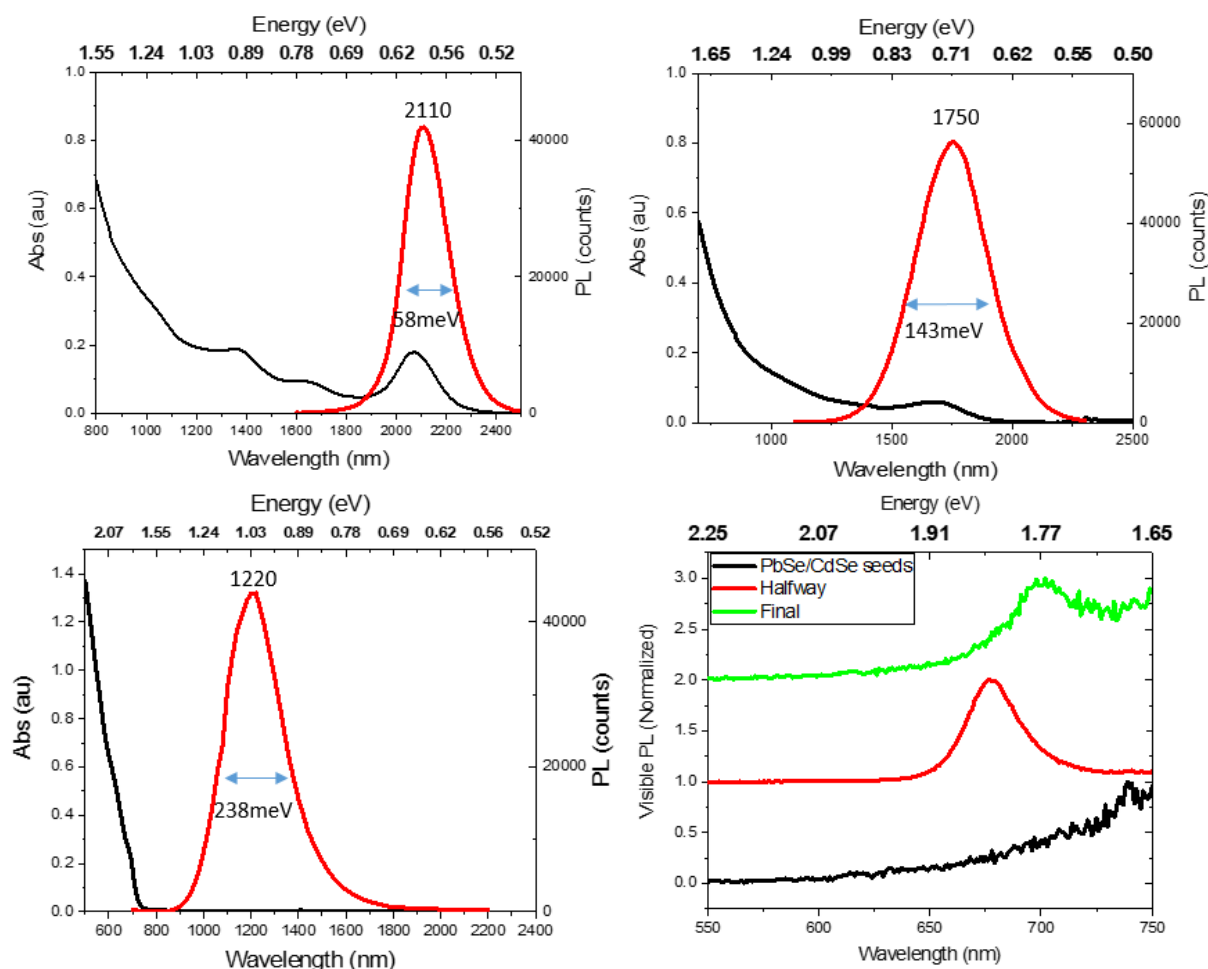
Figure 2.9 (Top left) Absorption and PL of PbSe cores, (top right) PbSe/CdSe seeds, (bottom left) final PbSe/CdSe/CdSe. (Bottom right) progression of visible emission during additional CdSe shell growth, note drifting of visible PL at higher wavelengths is due to correction factor of the instrument.

Figure 2.10 shows TEM images of PbSe/CdSe/CdSe QDs synthesized using slow injection via syringe pump (2 mL/hr) of Se in ODE and CdOA, the final shell thickness was roughly 3 nm. Shell thickness was found by calculating core diameter using ***Equation 1.1*** and subtracting that away from the total size based on TEM images. While these thick shell PbSe/CdSe QDs also

appear to be somewhat cubic in shape, they were not as well defined as those made via SeSUS injections.
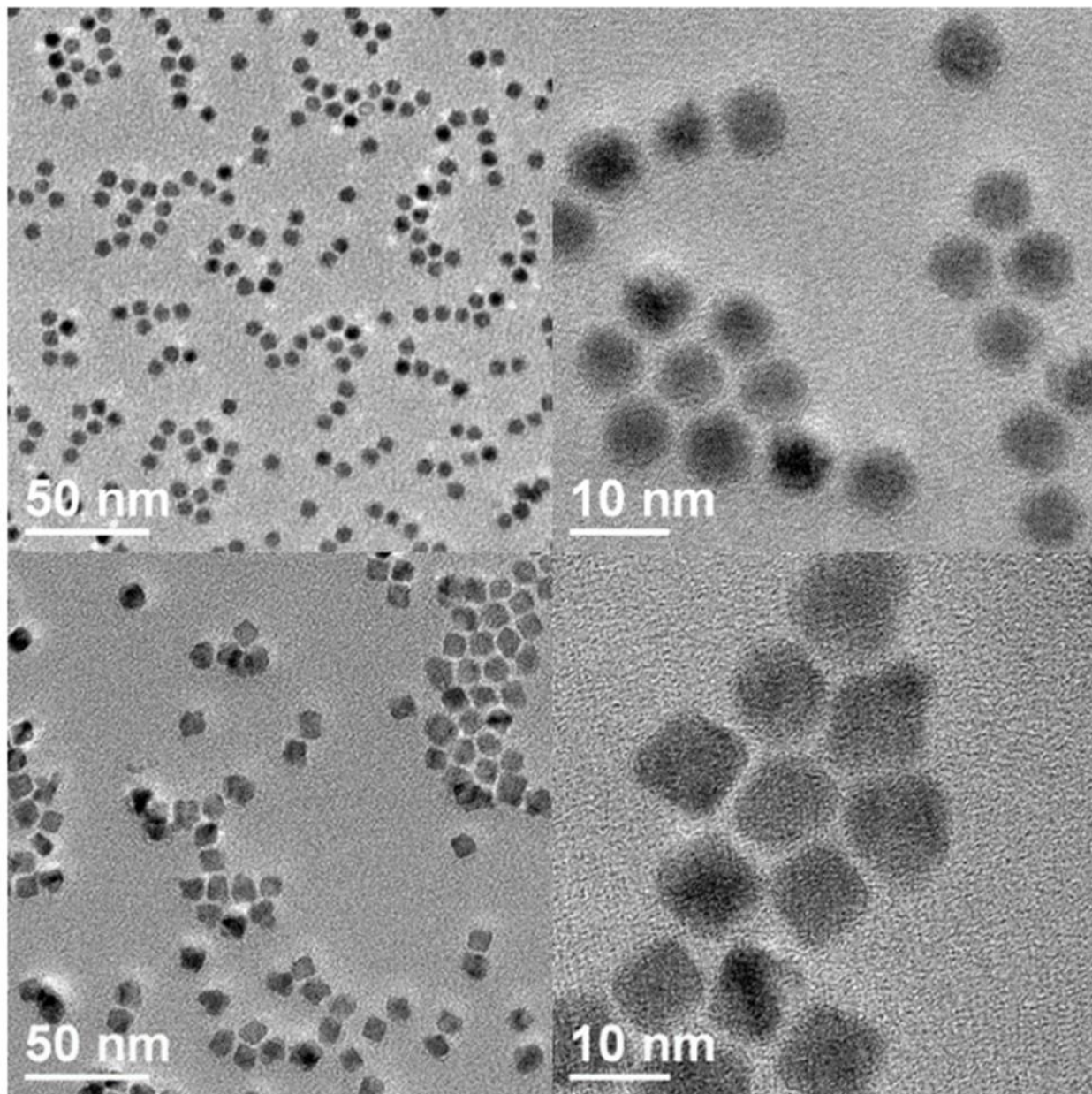
Figure 2.10 TEM images of PbSe/CdSe seeds (top) and final PbSe/CdSe/CdSe particles synthesized via slow injection with a syringe pump.

Utilizing TOPSe as a Se precursor is a method that has been employed to create thick core/shell QDs [44] with wurtzite outer shell crystal structure. TOPSe is a more reliable precursor that can be easily synthesized and stored in a glovebox for several weeks. SeSUS has small particles throughout the solution making addition of precise amounts difficult and Se shot dissolved in ODE forms conglomerates when stored overnight and requires re-heating before each use. Due to these factors, TOPSe was used as a replacement for Se in ODE for further shell growth, with slow injection via syringe pump employed as the precursor addition route.

PbSe/CdSe seeds were synthesized at a cation exchange temperature of 120°C overnight, the resulting particles exhibited weak (PLQY ≈0.01%) visible emission at 625 nm. During shell growth the NIR peak remains relatively constant, briefly blue shifting during heat up and shell growth, however it recovers and slightly narrows as the CdSe shell becomes thicker, **Figure 2.11.** Visible emission red shifted until it reached roughly 700 nm, **Figure 2.12**, indicating a thickening of the CdSe shell.
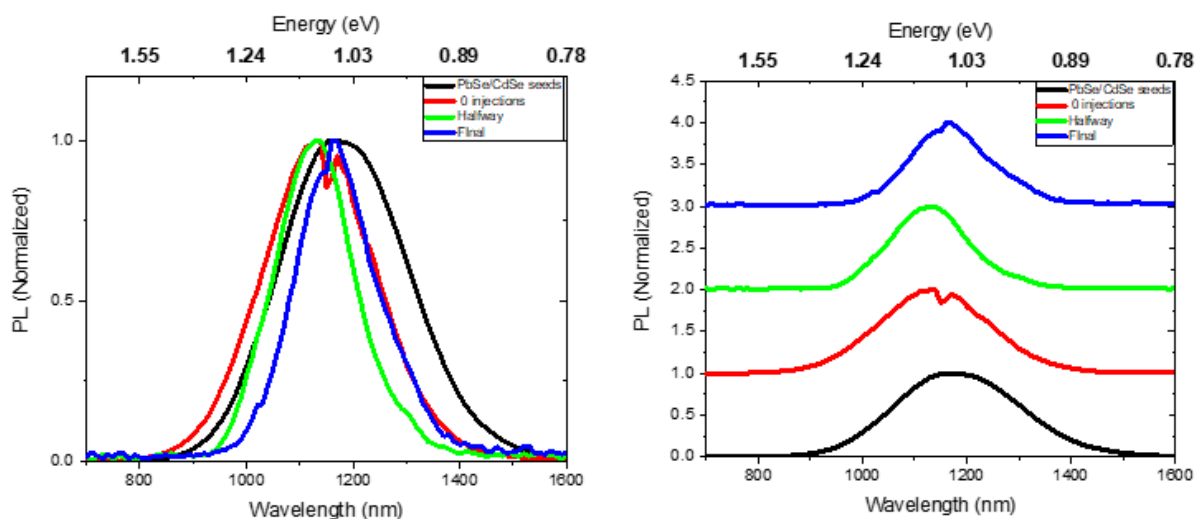
Figure 2.11 Progression of NIR PL during shell growth, peak initially slightly blue shifts but recovers as CdSe shell becomes thicker. Left and right are same spectra, right is just stacked for clearer viewing.
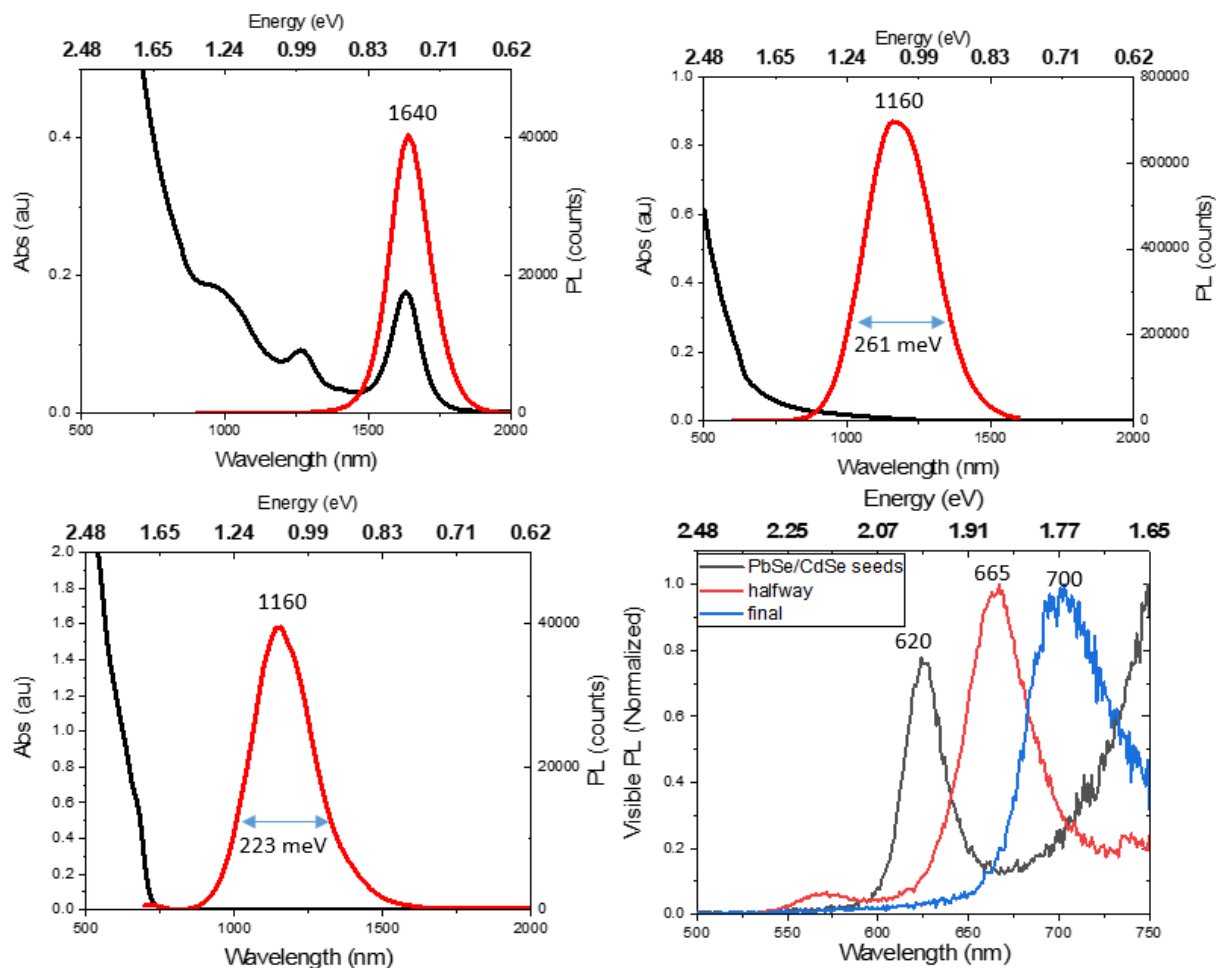
Figure 2.12 Absorption and PL spectra of PbSe core (top left), PbSe/CdSe seeds (top right), and final PbSe/CdSe/CdSe (bottom left). Progression of visible PL during shell growth (bottom right).

The TEM images of the images of the PbSe/CdSe/CdSe QDs are presented in **Figure 2.13,** showing a clear increase in the CdSe shell thickness, from ≈1.3 nm to 3 nm. The NIR PLQY of this sample is 8.9%, but the visible PLQY is still weak at less than 0.1%. Due to all the giant PbSe/CdSe/CdSe samples displaying very weak visible PLQYs, up-conversion measurements were limited to PbSe/CdSe/CdS samples presented in the next section. **Table 2.1** summarizes the results presented for giant PbSe/CdSe/CdSe QDs.

Table 2.1 Summary of PbSe/CdSe/CdSe heterostructures visible and NIR PLQYs

QD	Se precursor	NIR peak position (nm)	Visible peak position (nm)	NIR PLQY	Visible PLQY
Tetrapods	SeSUS	1550	N/A	0.4%	N/A
Cubic PbSe/CdSe/CdSe	SeSUS	1260	N/A	1.1%	N/A
Cubic PbSe/CdSe/CdSe	Se in ODE	1220	700	6.3%	0.01%
PbSe/CdSe/CdSe	TOPSe	1160	700	8.9%	0.1%
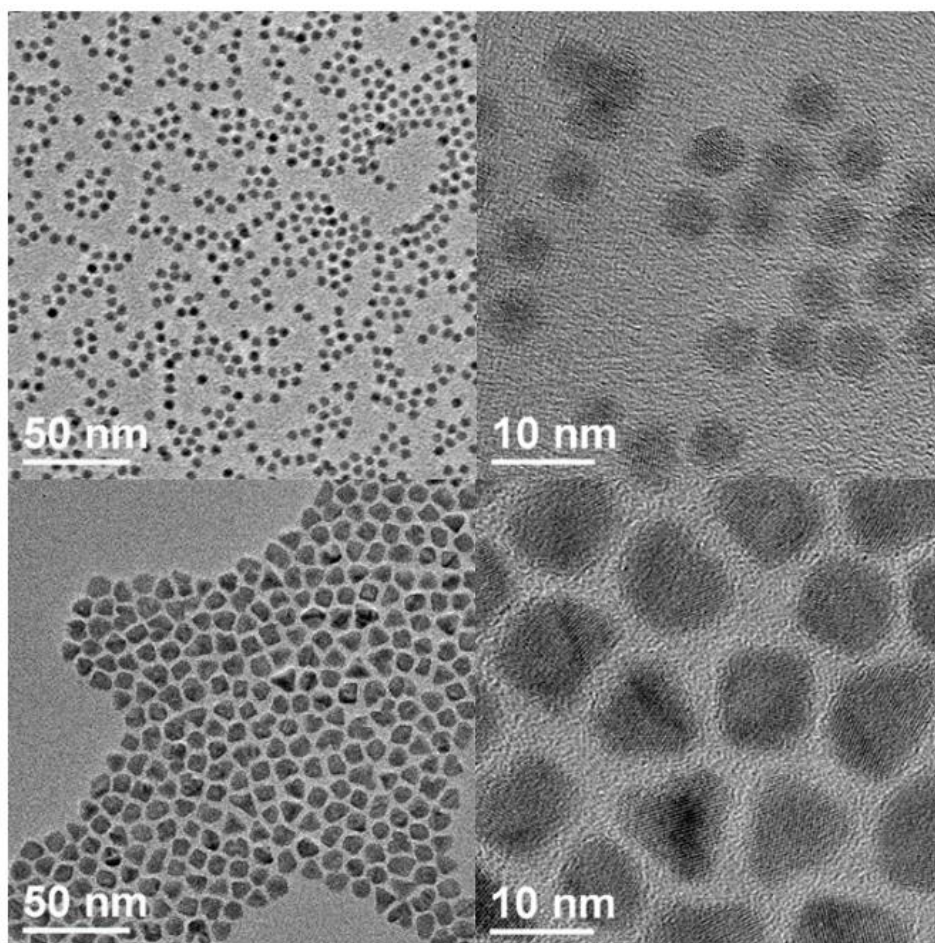
Figure 2.13 TEM images of PbSe/CdSe seeds (top) and PbSe/CdSe/CdSe QDs synthesized using TOPSe precursor

2.4.2 PbSe/CdSe/CdS QDs

PbSe/CdSe/CdS triangles:

Shelling with larger bandgap sulfides such as CdS and ZnS, has been shown to dramatically improve PLQYs of CdSe cores. Here we look at the improvement that is possible for visible emission that comes from a CdSe shell in dual emitting PbSe/CdSe QDs when capped with a thick CdS shell. Various attempts at shelling with ZnS were also tried but ZnS shell growth is performed at even higher temperatures that CdS, when using Zn-oleate as a Zn source. Diethylzinc is another option commonly used for Zn based shell growth, but diethylzinc is an extremely pyrophoric chemical, making it quite difficult to use. Therefore, CdS shell growth was the more attractive option as there have been multiple reports PbSe/CdSe/CdS heterostructure syntheses.

Thin-shell PbSe/CdSe seeds were prepared via cation exchange overnight at 80°C, resulting in roughly a monolayer thick CdSe shell. PbSe/CdSe seeds showed no visible emission, however growth of a CdS shell using alternating injections of S in ODE and CdOA, a 170°C, resulted in the appearance of visible emission at 630 nm. The NIR emission blue-shifted from 1470 nm to 1240 nm, as well as broadened to 280 meV from 106 meV, **Figure 2.14** shows the absorption and PL of the QDs before, during, after CdS shell growth.
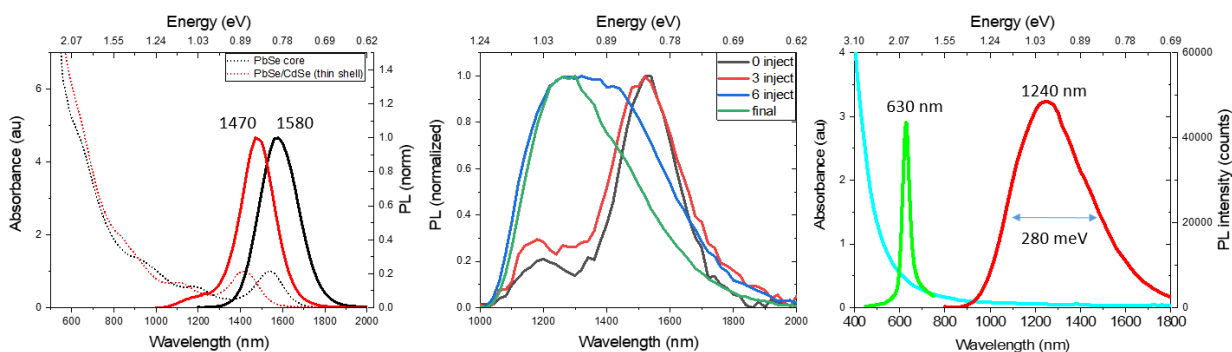
Figure 2.14 Absorption and PL spectra of PbSe cores, PbSe/CdSe seeds (left) and PbSe/CdSe/CdS triangles (right). Progression of NIR PL during CdS shell growth (middle)

Importantly the visible emission spectra have a symmetrical distribution (*i.e.* Gaussian) even when excited with 400 nm light, indicating that the sample is devoid of smaller CdS particles. TEM images, **Figure 2.15**, confirm the sample purity as well as reveal a triangular shape. We attribute the triangular shape to the lack of thickness of the intermediate CdSe, as these growth conditions typically result in tetrapod shaped nanoparticles due to the slow growth conditions and shape control controlling effect of the certain facets being more prone to growth.
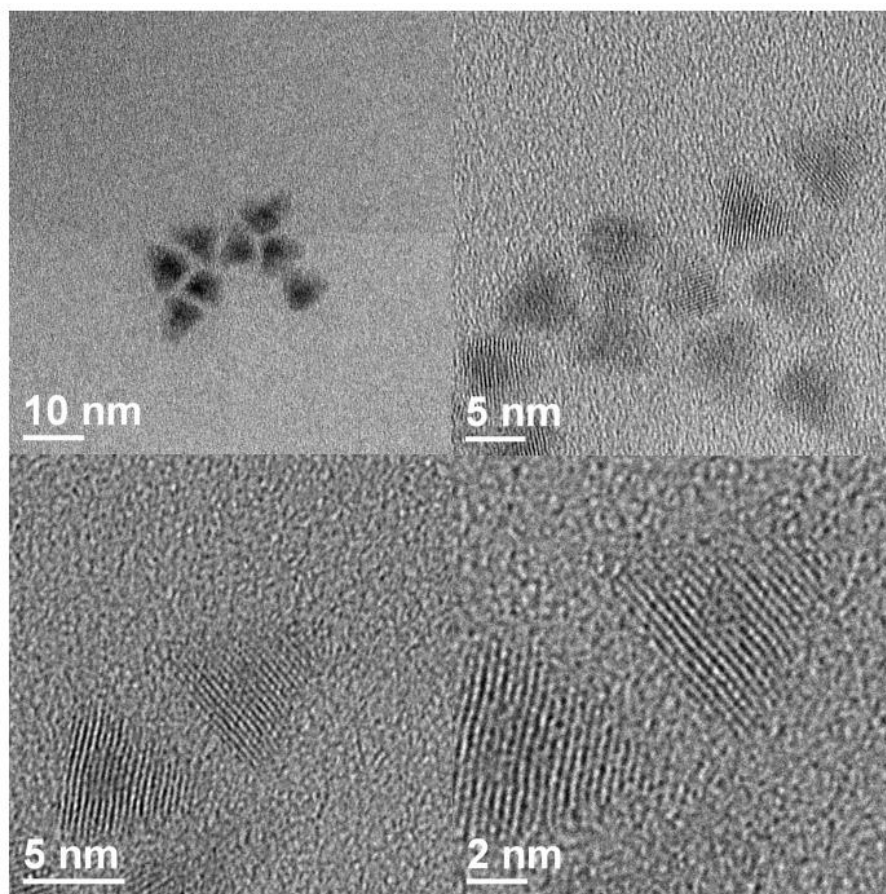
Figure 2.15 TEM images of PbSe/ CdSe/CdS nanoparticles, the presence of an abrupt interface between core and shell can be clearly seen in high resolution images.

The presence of the CdS outer shell, causes the electron to delocalize even further from the PbSe core where the hole is localized, **Figure 2.16 A, B.** This results in an increase in the IR

PL lifetime, as the spatial overlap of the electron and hole is significantly reduced. The progression of PL lifetime is shown in **Figure 2.16 C**, the lifetime increases from 300 ns to 700 ns to 2100ns, for PbSe cores, thin-shell PbSe/CdSe QD and PbSe/CdSe/CdS triangle respectively.
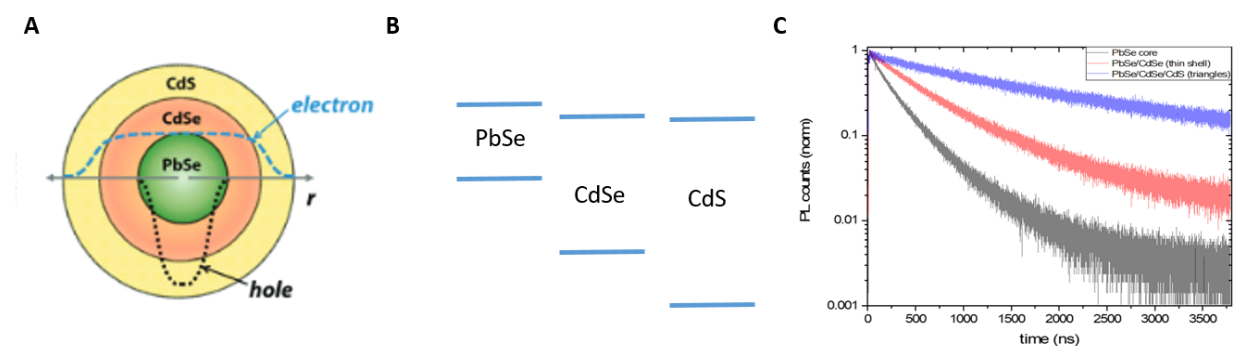
Figure 2.16 (A) schematic of the electron and hole delocalization in the PbSe/CdSe/CdS nanocrystals reprinted from reference [43] **(B)** schematic of the energy band offsets in PbSe/CdSe/CdS nanocrystals. **(C)** IR PL lifetimes of PbSe cores (black), thin shell PbSe/CdSe QDs (red) and PbSe/CdSe/CdS triangles (blue), excitation wavelength 800 nm.

PbSe/CdSe/CdS tetrapods:

Thicker intermediate CdSe shells results in tetrapod shaped nanocrystals under the same growth conditions that were used in the previous section for triangles. The formation of CdS arms rather than a uniform shell is attributed to the low shell growth temperatures, resulting in in a super saturation of the precursor at the more reactive facets followed by a surge in one dimensional growth. The {111} facet of the cubic zinc blende structure is atomically identical to the {0001} facets of the hexagonal wurtzite structure promoting growth on the facets [80]. The resulting tetrapods have "arms" ranging from 4-6 nm in length as well as a slightly (≈ 1 nm) larger core than the PbSe/CdSe seeds, see TEM images in **Figure 2.17.**
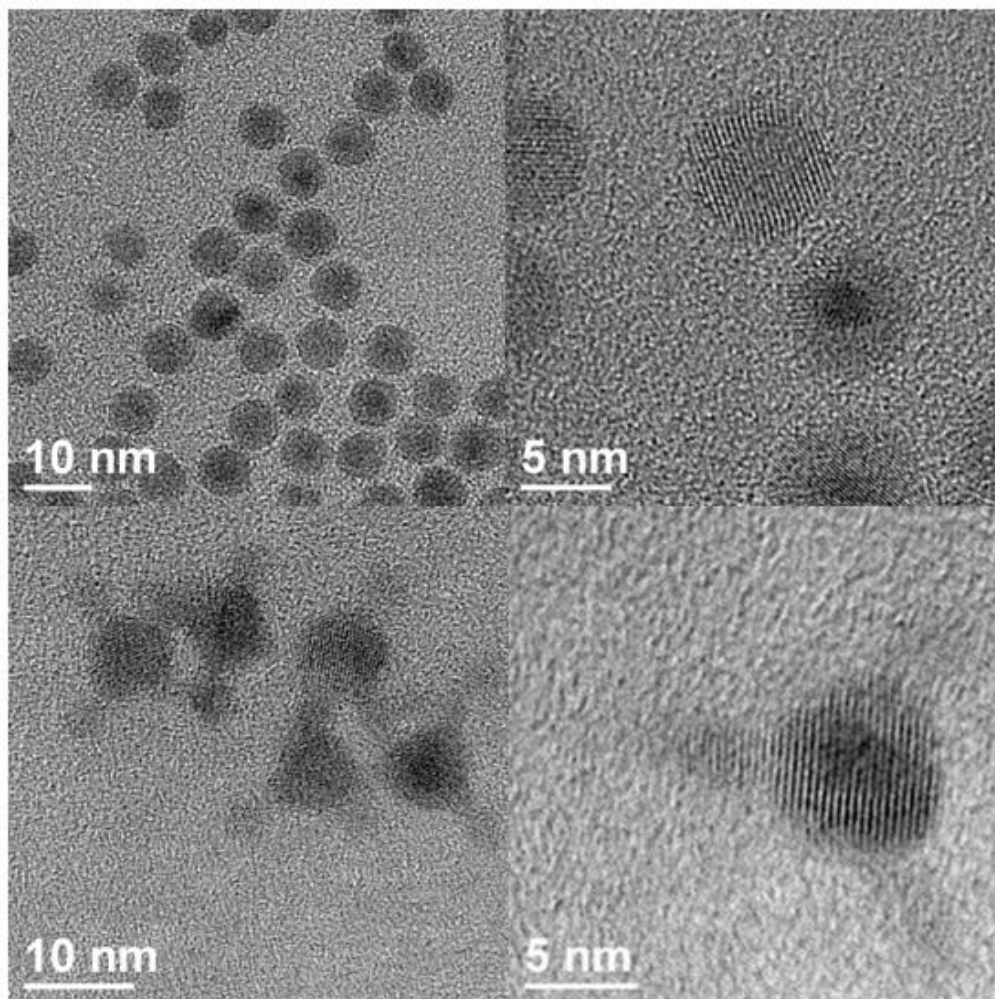
Figure 2.17 TEM images of PbSe/CdSe seeds (top) and PbSe/CdSe/CdS tetrapods (bottom)

PbSe/CdSe seeds were prepared by cation exchange reaction at 120°C, resulting in a shell thickness of roughly 1.6 nm. The thicker CdSe shell acted as a protective layer during additional CdS shell growth as the NIR peak did not noticeably blue shift. The IR PLQY was however significantly impacted dropping from ≈ 5 % down to 2.8 %. However, based on the IR PL peak width of the PbSe/CdSe seeds and tetrapods being nearly identical, **Figure 2.18,** we can assume that the structural integrity of the core was maintained during the CdS arm growth.
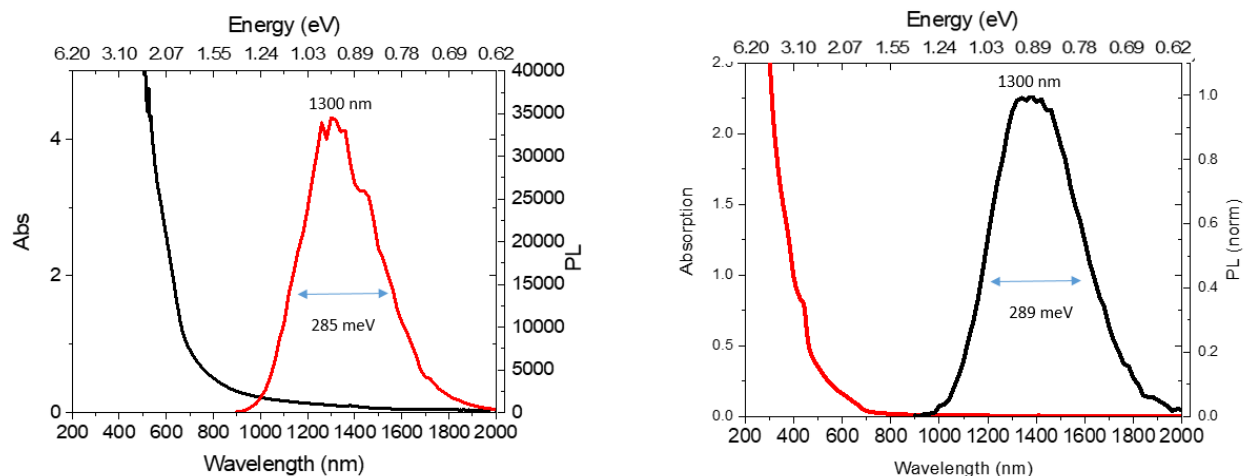
Figure 2.18 Absorption and PL of PbSe/CdSe seeds (left) and PbSe/CdSe/CdS tetrapods (right)

The PbSe/CdSe seeds showed weak ($\approx$ 0.05% PLQY) emission in the visible regime at 675 nm. Visible emission efficiency was significantly improved after CdS growth to 1%, while maintaining the peak position. Excitation with 500 nm and 400 nm light sources did not shift the peak position, however there was a slight tail at the blue end of the emission when excited with 400 nm light, **Figure 2.19.** This tail could be attributable to the CdS arms, as CdS can be excited with 400 nm light while 500 nm light does not have enough energy, or possibly residual CdS particles that were not able to be removed during cleaning. The IR PL lifetime became drastically longer after CdS growth increasing from $\approx$ 2 µs up to $\approx$11 µs in radiative lifetime, **Figure 2.19** (right). The reduction in PLQY in the IR could be a result of non-radiative losses occurring within the nanocrystal, which would be consistent with the significant increase in the radiative lifetime [81]. The ultra-long radiative lifetimes in these nanocrystals could be valuable in QD based solar cells, where the long time apart for the electron and hole could make collecting these carriers in a PV cell more likely.
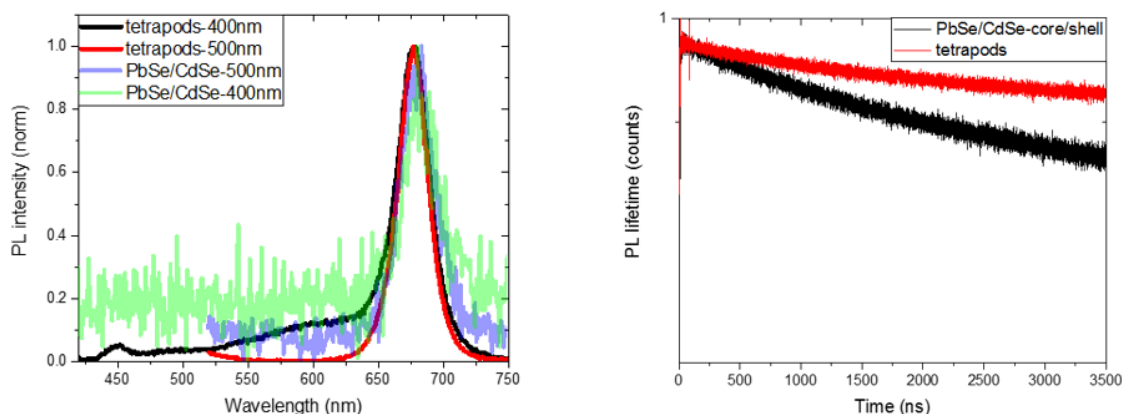
Figure 2.19 Visible PL peaks of PbSe/CdSe seeds and PbSe/CdSe/CdS tetrapods when excited by different wavelengths (left). IR PL lifetime measurements of PbSe/CdSe seeds and PbSe/CdSe/CdS tetrapods (right), excitation wavelength 800 nm.

PbSe/CdSe/CdS core/shell/shell

In an effort to improve the visible emission efficiencies, which could be a result of poorly passivated CdSe surfaces, we increased the CdS shell growth temperature to 240°C to form a uniform shell around the PbSe/CdSe seeds. PbSe/CdSe QDs were prepared in the same manner as those used for the tetrapod synthesis, cation exchange overnight at 120°C. CdS shells were synthesized by alternating injections of S in ODE and CdOA at 240°C with 10 minutes between each injection. There is only a slight shift in the PL peak during shell growth (from 1180 nm to 1170 nm) and the peak width remains relatively constant after CdS shell growth. Visible emission remains in the same spot after CdS shell growth, but the PLQY increases to 5% after initially being less than 0.1%. The absorption and PL spectra as well as the visible emission spectra are presented in **Figure 2.20**; note that the visible emission remains symmetrical in shape

even when excited with 400 nm light, indicating the lack of CdS sub ensemble particles, an observation that is confirmed via TEM imaging, **Figure 2.21.**
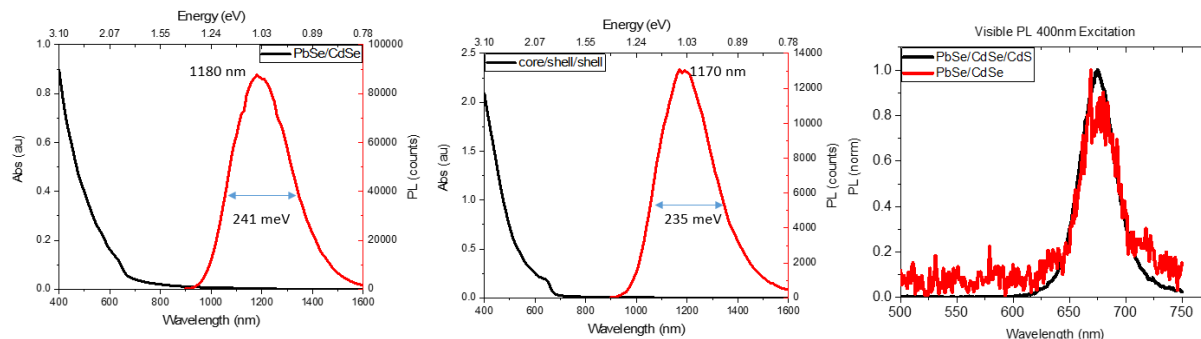
Figure 2.20 Absorption and NIR PL of PbSe/CdSe seeds (left) and PbSe/CdSe/CdS QDs (middle). Visible emission of PbSe/CdSe and PbSe/CdSe/CdS QDs when excited with 400 nm light source (right).
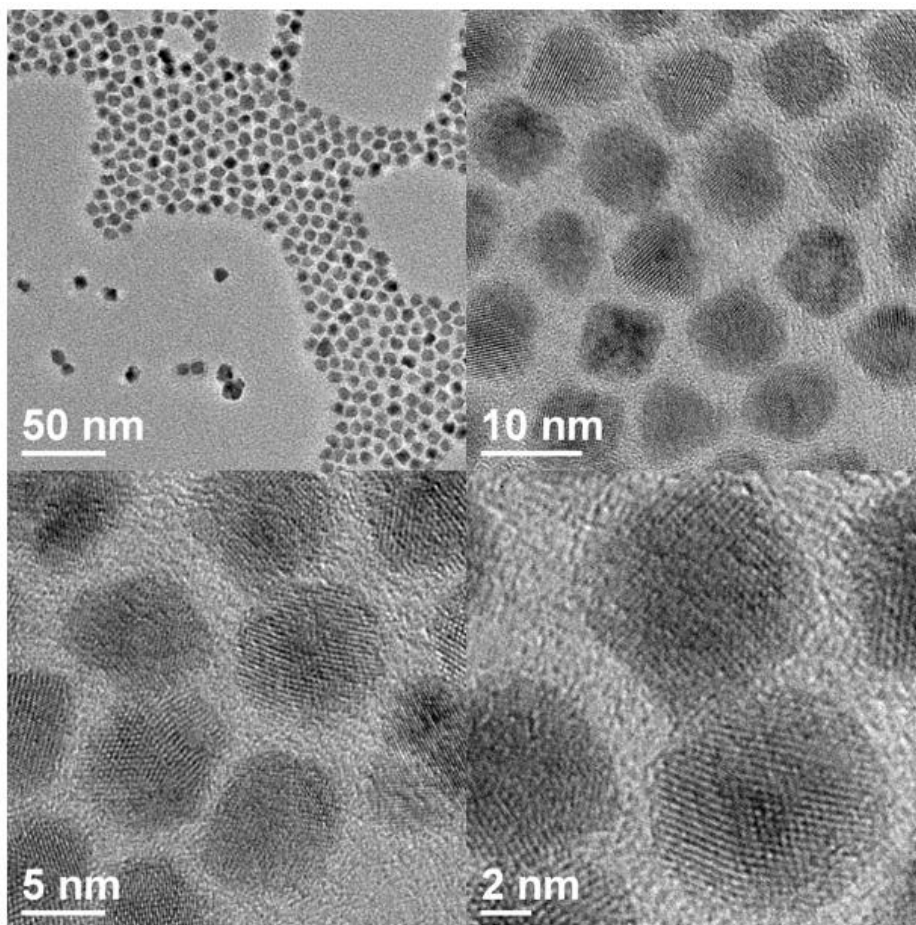
Figure 2.21 TEM images of PbSe/CdSe/CdS QDs

Lifetime measurements of the NIR PL show that the radiative lifetime of the

PbSe/CdSe/CdS QD is ≈ 16 µs when measured with a pulsed laser at 800 nm excitation with a

slow rep rate of 15 kHz, **Figure 2.22**. In **Table 2.2** the PL peak positions, quantum yields, NIR

lifetimes of PbSe/CdSe/CdS heterostructures are summarized.

Table 2.2 Summary of PbSe/CdSe/CdS nanocrystal optical properties

PbSe/CdSe/CdS nanocrystal	NIR PL peak position (nm)	NIR PLQY	NIR PL radiative lifetime (µs)	Visible emission peak (nm)	Visible PLQY
Triangle	1240	2.3%	2.1	630	0.7%
Tetrapod	1300	2.8%	11	675	1%
Core/shell/shell	1170	1.9%	16	675	5%
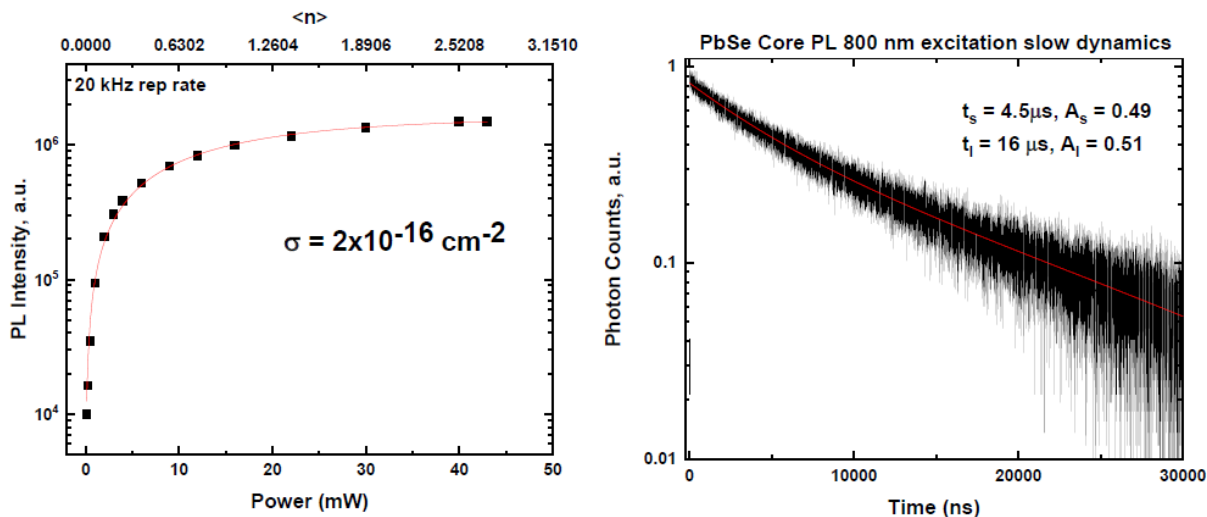
Figure 2.22 The NIR PL lifetime measured using SSPD with 800 nm pump, 4 ps resolution, 15 kHz rep rate for slow dynamics (right). Calculated absorption cross-section of PbSe/CdSe/CdS QDs at 800 nm (left)

By measuring NIR PL lifetimes at increasingly high excitation intensities we can find the

point at which saturation occurs, from this the absorption cross-section at 800 nm for the QD can

be calculated, as presented in **Figure 2.22.** An absorption cross-section of 2 X 10^{-16} cm^2 is

derived from these measurements, which is slightly lower than those calculated for thick shell

PbSe/CdSe QDs [74]; however this value is conceivable due to the growth of CdS lowering the

overall absorption of the QDs at 800 nm, which is seen in the simple absorption spectra

presented in **Figure 2.20.**

Next we study upconverted emission from the shell when excited with 800 nm pulses

with a pulse duration of 180 fs. The pump photon energy is below the band gap of the CdSe/CdS

shell, and therefore, excitation of shell emission is possible only via one (or combination) of the

up-conversion mechanisms shown in **Figure 2.3.** The shell emission closely resemebles the

emission seen when excited with 400 nm excitation, **Figure 2.20** (right). The upconverted PL

scales quadractically with excitation power, **Figure 2.23**, which is to be expected for 2 photon

absorption.
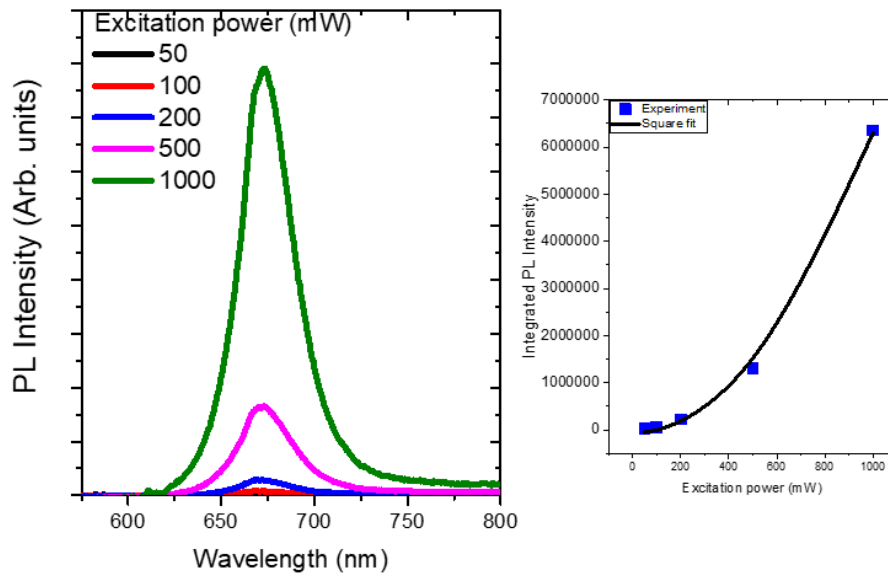
Figure 2.23 Up-convert emission when excited with 800 nm pulses at varying excitation powers

(left), integrated PL intensity as a function of excitation power (right).

Up-conversion dynamics were measured with 800 nm pump, 250 kHz rep rate. The up-conversion dynamics did not depend on excitation power so only the least noisy sample in presented (roughly 1.3 excitons per dot), **Figure 2.24**. The up-converted PL dynamics show a very fast component ($\approx$ 200 ps) in which about 50% of the decay occurs.
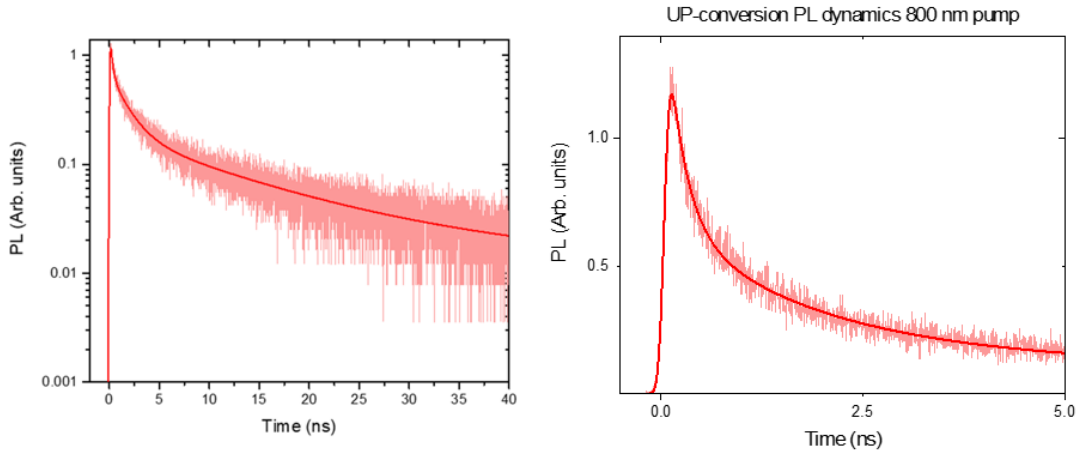
Figure 2.24 Up-conversion dynamics of PbSe/CdSe/CdSe QDs when excited with 800 nm pulses. Right and left are same data, right is just zoomed into short time scales and displayed on a linear scale.

The quadratic nature of the up-converted PL with relation to excitation power suggests that the predominant form of up-conversion in the sample is simple 2 photon absorption. In order to identify if Auger assisted up-conversion is indeed occurring a simple 2 pulse measurement using delayed pulsed excitation is performed in which the length between pulses is varied. If only 2 photon absorption is occurring this should result in linear relationship between the up-conversion intensity and pulse delay. However if Auger assisted up-conversion is present, the up-converted PL intensity would eventually become independent of duration between pulses, as the duration between pulse becomes longer the electrons in the intermediate state would have

time to relax back to the core state before absorption of the second pulse could be used to promote the intermediate state electron into the shell. A deviation from linearity would clearly show that 2 electrons were indeed being excited into an intermediate state by a single pulse and then a coulomb interaction between them results in one electron being promoted to the higher energy shell state. **Figure 2.25** shows the raw data in terms of PL intensity for these 2 pulse measurements, while **Figure 2.26,** graphically displays the up-converted intensity as a function of duration between pulses. Clearly as the pulse delay becomes longer the up-conversion intensity eventually strays from linearity (after about 0.5 ps between pulses), from that point on the up-converted PL intensity remains relatively constant.
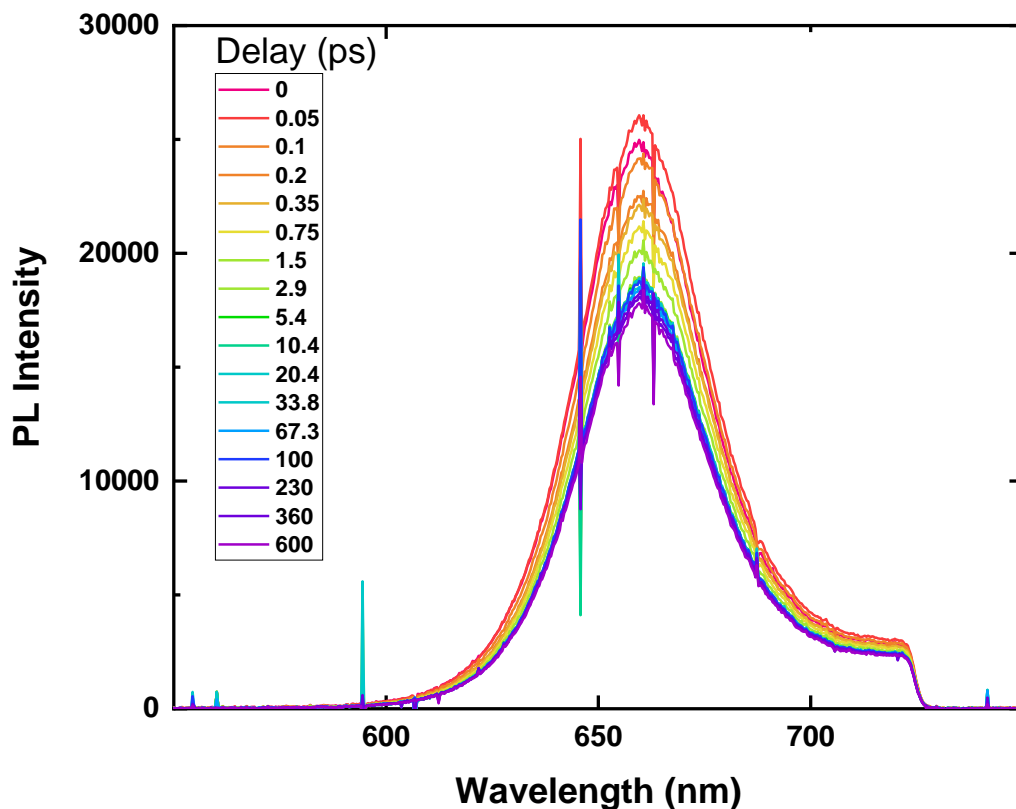
Figure 2.25 Up-convert PL intensity as a function of pulse delay. Note the slight shifting in PL peak is attributed to the use of a different detector
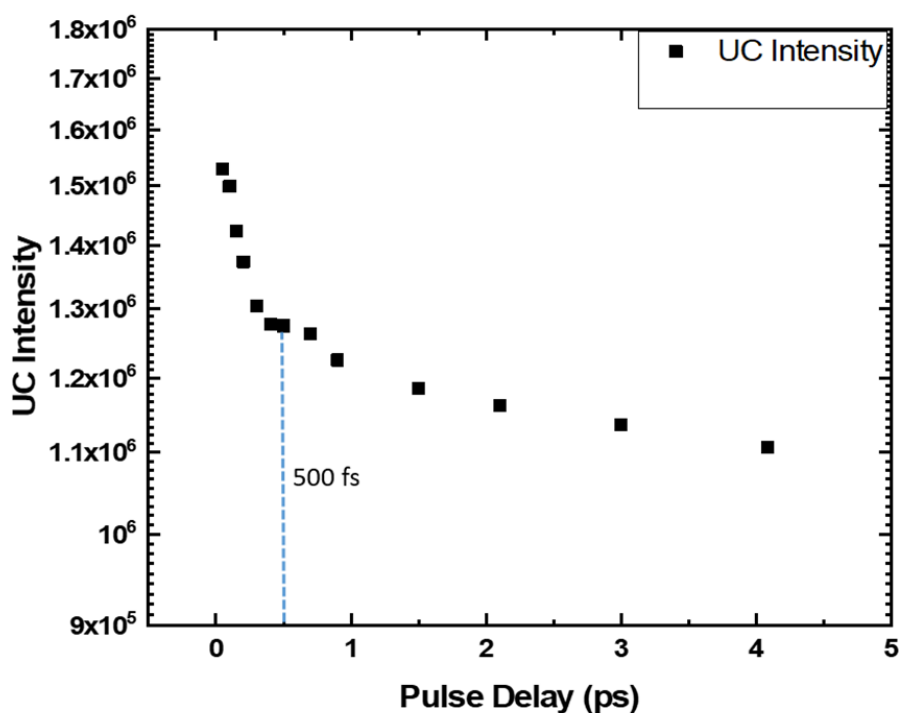
Figure 2.26 Up-converted PL intensity as a function of delay between pulses, the intensity starts to become independent of pulse duration after 500 fs.

Using the values of the power dependent up-converted PL intensity, shell emission QY, and absorption cross-section (σ) we can estimate the 2-photon absorption cross-section (δ_{2PA}). Absorption cross-section (σ) can be converted to the molar extinction coefficient (ε) in units of cm^{-2} with the following equation:

$$\sigma = 3.8235 \times 10^{-21} \, \varepsilon \qquad\qquad \textit{Equation 2.1}$$

After the molar extinction coefficient is found, **Equation 1.5** (printed below for reference) can be used to calculate the concentration (2.1 x 10^{-6} mol/L).

$$C = \frac{A}{\varepsilon L} \qquad\qquad \textit{Equation 1.5}$$

δ_{2PA} can then be estimated using **Equation 2.2**, where we used the PbSe/CdSe QDs engineered for Auger assisted up-conversion as a reference sample.

$$\delta_{2PA} = \delta_{2PA}^r * \left(\frac{UPL/C*QY}{UPL^r/C^r QY^r}\right) \qquad \text{Equation 2.2}$$

Where *UPL* is the power dependent up-converted PL intensity (taken from pulse measurements **Figure 2.23**), *C* is the concentration, *QY* is the PLQY from the shell (5% in this case). Variables with an *r* superscript are values taken from the reference sample from the paper by Makarov *et al.* [28]. The calculated δ_{2PA} is 1.5 x 10^{-46} cm^4*s, which is about an order magnitude lower than those calculated for thick shell PbSe/CdSe QDs [28]. The δ_{2PA} combined with the core exciton lifetime τ_1 value and time constant found in **Figure 2.26,** where the up-converted PL starts to become independent of pulse delay τ^* can be used to calculate the Auger up-conversion cross-section δ_{AU} with **Equation 2.3**.

$$\delta_{AU} = \sqrt{\frac{2}{\pi}} \left(\frac{\tau_1}{\tau^*}\right) \delta_{2PA} \qquad \text{Equation 2.3}$$

The calculated value of δ_{AU} is 3.8 x 10^{-39} cm^4*s, from this value the Auger up-conversion quantum yield (QY_{AU}) can be calculated using **Equation 2.4**.

$$QY_{AU} = \frac{\delta_{AU}}{(2\tau_1\sigma^2)} \qquad \text{Equation 2.4}$$

The calculated QY_{AU} is ≈0.3% which is quite low, but is higher than that which is reported for thick shell PbSe/CdSe QDs of 0.2% [28]. The low value for QY_{AU} is attributed to low PLQY of the core, which can be explained by poor passivation and possible trap states at the core shell

interface, as well as the broad distribution in core and shell size as indicated by the relatively broad (235 meV) IR PL peak.

2.5 Summary

In this section we synthesized two types of giant QDs, PbSe/CdSe/CdSe and PbSe/CdSe/CdS heterostructures. Showing that additional CdS shell growth on PbSe/CdSe/CdS QDs significantly increases the visible PLQY of the CdSe shell emission. The effect of growth conditions, such as temperature and precursor choice, show a significant effect on the final structural properties of the nanocrystals. Growth of a thick CdS shell or CdS arms in the case the tetrapod structure results in long exciton lifetimes, due to the degree of hole localization to the PbSe core and electron delocalization as far out as the CdS shell, which can be a valuable asset to application such as solar cells. These QD heterostructures are an example of a unique class of tunable, dual-emitting, dispersible fluorophores that may be useful for unique types of labeling and PL microscopy, especially when the IR emission falls within the tissue transparency energy window. Finally, this type of structure-based control over carrier relaxation may ultimately prove useful for "hot-carrier" photovoltaics, or for improving the efficiencies of desirable processes that compete with cooling, such as Auger assisted up-conversion.

Chapter 3: PbSe Quantum Dot Devices

3.1 Introduction

In the previous section we focused on engineering single QDs and how they interact with photons in solution, with experimental setups with laser excitations. These scenarios are valuable for learning about the fundamental properties of QDs, however understanding QD film behavior when excited with photons or an applied voltage can be more valuable for the implementation of QDs in real world devices. PbSe QDs are of interest for a wide range of optoelectronic device applications that seek to take advantage of their size-tunable optical properties and amenability to low-cost solution-based processing [82]. PbSe quantum dots (QDs) have the potential to improve upon current photodetector technologies in the near-IR and mid-IR spectral regions [51,83]. Size tunable emission ranging from 1-4 µm [23], the possibility of carrier multiplication [84], and various developed methods such as quantized Ostwald ripening [85] to improve the size distribution to as little 5% within an ensemble, are all advantageous properties for photodetection purposes. Improving capabilities in these regions is of significant consequence for applications such as; environmental monitoring [86], motion sensing [87], and fiber-optic communications [88]. Additionally, the high Z number of PbSe QDs make them promising candidates for detection of higher energy photons such as X-rays and gamma rays; however, for these purposes the development of thick uniform films is vital.

Despite these promising properties early QD devices suffered in performance due to low carrier mobility as a result of long insulating ligands that stabilize QDs when they are in colloidal solution, but cause discontinuities between QDs when they are made into a film [89]. Layer-by-layer ligand exchange employed during QD film preparation, in which long native ligands in a thin QD film are replaced by shorter ligands through exposure to a solution containing more

strongly binding short ligands, was an early solution to improve QD spacing issues within films [46,52]. However, layer-by-layer ligand exchange is only successful if the QD film is sufficiently thin to allow complete solution penetration and can result in non-uniform films as it must be performed repeatedly when producing a thicker film.

In 2017 Lin *et al*. [32] introduced a universal method for in-solution ligand exchange of PbSe QDs with short ionic ligands, allowing for the deposition of thicker films and removal of post deposition ligand exchange step. Resulting devices showed carrier mobilities on the order of 10^{-2} cm^2/Vs, without the help of atomic-layer-deposition (ALD) infilling with alumina, which has been shown to increase carrier mobility up to 7 cm^2/Vs [63].

Surface ligands have been shown to affect carrier type [90,91] and energy band position [56] in PbSe QD films. Despite these findings, to date there has been very little study of the effect surface ligands have on the intrinsic carrier density of a QD film. Carrier density is an important factor in devices such as solar cells, where higher carrier densities allow for creating *p-n* junctions, and photodetectors, in which lower carrier densities lead to lower dark currents and in turn more sensitive detectors. Kagan *et al.* studied the effect of stoichiometric imbalances on PbSe QD film carrier densities through both evaporation of cationic and anionic species onto films [60], as well as through treatment with $PbCl_2$ and $NaSe_2$ solutions [59]. However, both of these studies used post fabrication treatments of PbSe QD films which can be time consuming and laborious. Herein we present intrinsic carrier density modulation in PbSe QD films prepared in a single deposition step with QDs in which ligand exchange is performed in solution.

Results on carrier density modulation are combined with simple mobility measurements to identify ligands that could be well suited for applications in which high carrier mobility combined with relatively low carrier concentrations would be valuable, such as high energy

photon or alpha particle detectors. Mobility measurements are performed using simple field-effect-transistors (FETs), fabricated on Si/SiO2 substrates. FETs are unipolar transistors that use an electric field to drive carrier flow within the device: source (where the carriers enter the channel) and drain (carriers extracted from the channel) electrodes are separated by a semiconductor channel through which the carriers flow. The conductivity between the drain and source terminals is controlled by an electric field generated by the voltage difference between the body (QDs) and the gate of the device [92]. Many FETs include a thin insulating layer to separate the gate from the body of the device. FETs can be either *p*-type or *n*-type depending on the type of carrier flow that is prevalent within the device, a characteristic that can be altered by modifying the QDs surface chemistry and composition. FETs are used to amplify weak signals making them ideal for research purposes before incorporating QDs into more complicated devices such, such as solar cells and photodetectors. Examining the carrier transport properties of QD films by incorporating them into FETs allows determination of the effect that each tunable parameter has on the carrier mobility and conductivity without having to account for the added variables that come with integrating QDs with other functional layers of a more complex device structure. A simple schematic of 2 types of FETs is presented in **Figure 3.1**, in this work we use the bottom contact architecture using *p*-doped Si as our gate electrode, as these are easier to fabricate and do not require deposition of an additional dielectric layer between the QDs and a floating gate electrode.
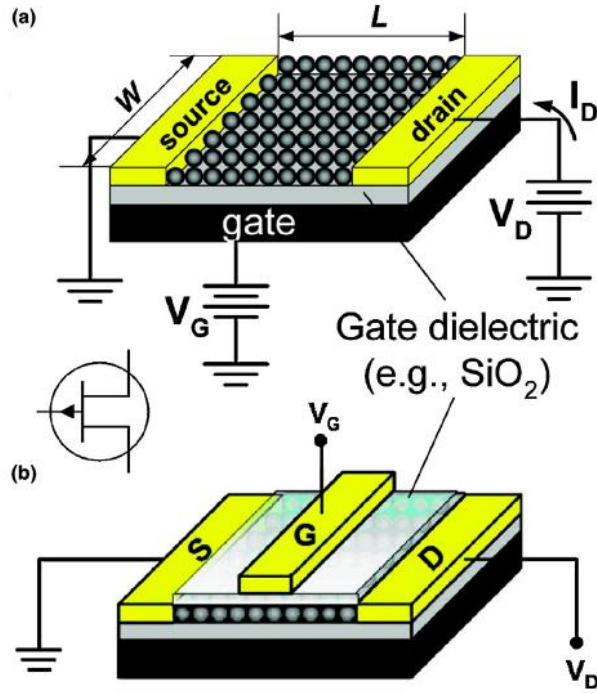
Figure 3.1 Schematic of a bottom gate (a) and top gate (b) FTE with a thin SiO2 insulating layer between the gate and the body (QDs) of the device. L is the channel length, W is the width, reprinted from reference[92]

FET operation is based on applying voltage to the source and gate of the device, injecting charges into the channel, when the voltage reaches a certain threshold the channel becomes conductive. After this threshold is reached, drain-to-source current increases linearly until a "pinch off" drain voltage is achieved at which point the current saturates. In the case of QD FETs the threshold voltage (V_T) corresponds to the point where the deep traps are filled allowing transport to occur, effectively a measure of the initial concentration of charge carriers[92]. Along with the threshold voltage, the current on-to-off ratio, subthreshold slope, and the field-effect mobility are key figures of merit for FETs. The field-effect mobility is different in the linear and saturated regimes and can be calculated by the following equations:

$$I = \left(\frac{W}{L}\right)\mu_{lin}C_i(V_G - V_T)V_D \qquad \qquad Equation\ 3.1$$

$$I = (\frac{W}{2L})\mu_{sat}C_i(V_G - V_T)^2 \qquad\qquad Equation\ 3.2$$

where I is the current, W is the channel width, L is channel length, C_i is the capacitance density

of the gate insulator, V_G is the gate voltage, V_D is the drain volatge, V_T is the threshold voltage,

and μ is the field-effect mobilty [93].

Capacitance devices used for the determination of carrier densities, are fabricated in as

simple sandwich structure devices, **Figure 3.2,** in which bias can be applied to *p*-doped Si

substrate. Proving that carrier density can indeed be controlled by simply changing the surface

ligand of a PbSe QD would be a important result, that would be applicable for the

implementation of PbSe QDs in many different device structures moving forward.
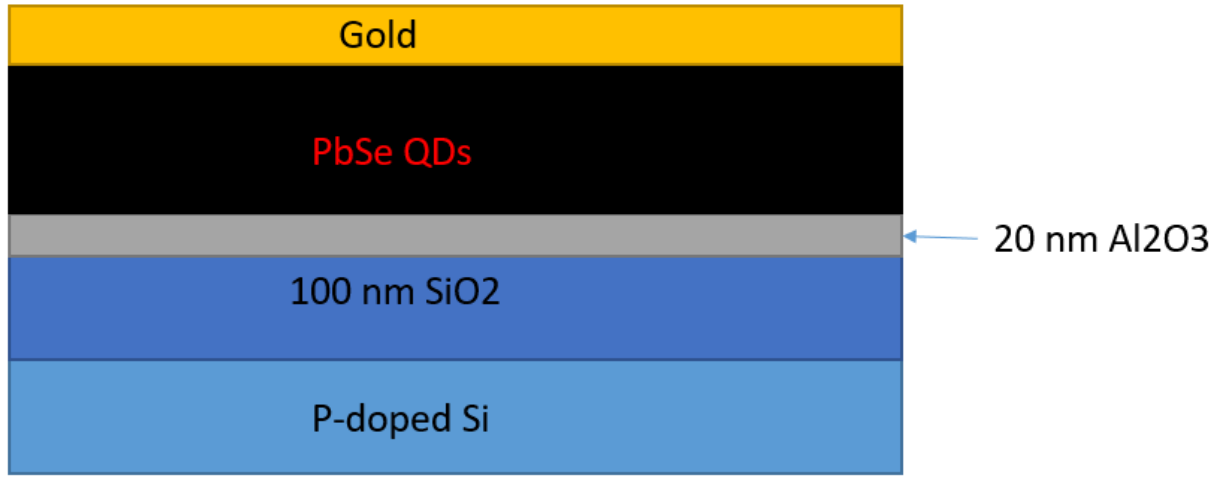
Figure 3.2 Schematic of a devices used for C-V measurements

3.2 Experimental Methods

Synthesis of PbSe QDs: PbSe QD preparation and ligand exchange was performed using

a modified recipe presented by Lin *et al.* in 2017. In short, 4 mmol of PbBr$_2$ + 4 mL of OLA +

12 mL ODE were loaded into a three-neck flask and degassed for 1 hour at 110°C. After

degassing the flask was placed under N$_2$ and the temperature was set to 160°C, when temperature

was reached, a solution of 0.5 ml 2M TOPSe + 2 mL OLA + 0.1 mL DIP was injected into the solution and the flask temperature was lowered to 140°C. The solution was allowed to react for 2 minutes before being removed from the heating mantle and cooling to room temperature. Purification was performed using a mixture of chloroform ($CHCl_3$) and acetonitrile, in order to prevent stripping of surface OLA ligands [36]. Following the first purification the QD solution was allowed to sit for 1 hour in $CHCl_3$ and then subsequently centrifuged at 5000 rpm for 1 minute to remove unreacted $PbBr_2$, after which the purification was performed 2 more times. Ligand exchange was performed by dissolving desired ligand (*e.g.* KI) in 5mL of N, N-dimethylformamide (DMF), at a concentration of 20 mg/mL, followed by addition 3mL of PbSe QDs in $CHCl_3$ (10-15 mg/mL). The mixture was then agitated for 10 seconds followed by centrifugation to crash out PbSe QDs which were re-dispersed in 2,6-difluoropyridine (DFP).

Fabrication of devices for C-V measurements: Devices for C-V measurements were prepared using *p*-doped Si substrates with 100 nm thermally grown SiO_2 layer purchased from WaferPro. 20 nm of Al_2O_3 was grown onto the substrate via ALD using a Savannah S300 ALD system. Substrates were prepared for QD deposition by sonication for 10 minutes with DI water, acetone, and isopropanol respectively. After sonication, substrates were cleaned using an O_2 plasma cleaner for an additional 10 minutes. QD films were prepared by spin-coating a solution of PbSe QDs ($\approx$ 30-40 mg/mL) in DFP at 600 rpm for 2 minutes; most samples required 2 applications of spin-coating to prepare films between 150-500 nm in thickness. 50 nm gold contacts with dimensions of 5x5 mm were deposited on top of the QD film via thermal evaporation through a mask. After deposition of the gold contact, devices were annealed on a hot plate at 150°C for 20 minutes; all device preparation was done in an inert atmosphere glove box.

Fabrication of FETs for mobility measurements: FETs were prepared on *p*-doped Si

substrates with either 100 or 300 nm thermally grown SiO_2 (depending on availability at the time

of device preparation). Substrate cleaning prior to QD deposition was done in the same manner

as mentioned above for capacitive devices. FETs were prepared with both top and bottom

contacts: for top contact QDs were deposited via spin-coating before deposition of gold contacts,

for bottom contact gold contacts were deposited, then QDs were deposited. The channel length

(L) is 100 µm while the channel width (W) is 2000 µm. Device edges were cleaned with acetone

after QD deposition to prevent current leakage. Devices were annealed at 150°C for 20 minutes.

Fabrication of PbSe QD radiation detectors: ITO glass was cleaned with sonication in

acetone for 10 minutes, followed by ozone cleaning for another 10 min. Then PbSe QDs with a

concentration of ~50 mg/mL were spin-coated onto an ITO glass substrate at 300 rpm for 10 min

in a N2-filled glovebox. After annealing the QD film at 150°C for 20 min, the top Au contact

was deposited by thermal evaporation through a shadow mask to achieve 100 nm thickness.

3.3 Characterization Techniques

FET, photodetector, radiation detector, and C−V characterization were conducted using a

semiconductor device parameter analyzer (B1500A, Agilent) in a N2-filled glovebox. The probe

contacts were placed onto electrodes using a dc probe positioner (DPP205-M-R-S, Aztec

Enterprises, Inc.). For C−V measurements, the top (metal) and bottom (*p*-type Si substrate)

contacts were connected to the low and high terminals, respectively. The C−V curve for each

device was measured at a frequency of 1 kHz. In PbSe radiation detector measurements,

illumination was provided by a white light LED source with a maximum intensity of 25.9 W/cm^2

that was attenuated using neutral density filters. We used a spring-loaded pin to make a soft

contact on the Au contact and measured the current response from the conducting ITO to Au contact in the dark and upon light illumination.

Transmission electron microscope (TEM) images were taken using a JEOL 2010 TEM, using QD samples drop cast from a dispersion onto carbon-coated copper grids. Absorption spectra were measured by a PerkinElmer Lambda 950 spectrophotometer. Near infrared (NIR) PL spectra were taken using a custom-built apparatus. Samples were excited using the mechanically chopped light from an 808 nm laser, and emission was spectrally dispersed using a grating monochromator and recorded using a liquid-N2-cooled InSb detector with lock-in amplification. The PL quantum yields (QYs) were determined relative to IR-26 (in 1,2-dicholorethane, $QY = 0.048\%$)[78]. FTIR spectra were taken on a Nicolet 4700 FT-IR from Thermo Electron Corporation. Film thickness and morphology were assessed using atomic force microscopy (AFM), conducted with a Nano IR2 AFM with Anasys software. Samples were prepared by using a razor blade to scratch the QD film, removing QDs but not scratching the substrate. Measurements were done by placing the cantilever tip near the scratch and scanning an area that encompassed at least one edge of the scratch.

3.4 Results and Discussion

Figure 3.3 shows absorption and photoluminescence (PL) spectra of PbSe QDs with selected ligands, as well Fourier transform infrared spectroscopy (FTIR) spectra and TEM images to confirm ligand exchange. From FTIR spectra (**Figure 3.3 B**) it is clear that the C-H stretch signature at ≈ 2900 cm^{-1} is removed from the samples in which ligand exchange has taken place, indicating a complete removal of OLA ligands, which is confirmed by TEM images (**Figure 3.3 C**) by the closer packing of QDs with shorter ligands.
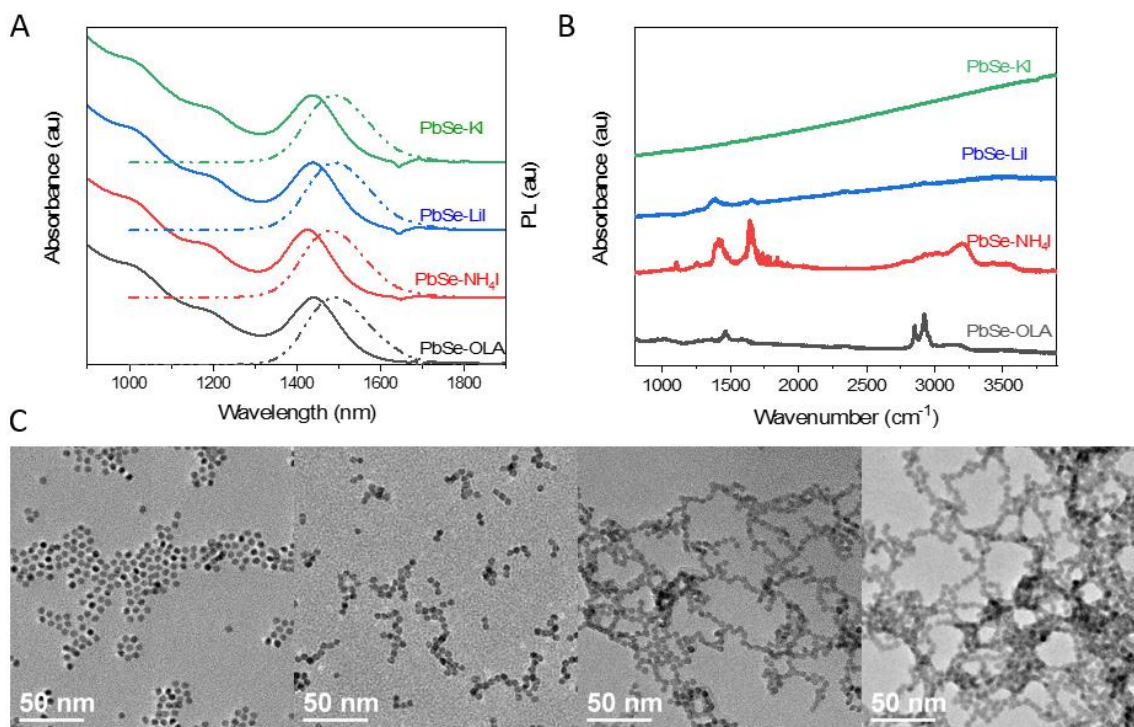
Figure 3.3 (A) Absorption and PL spectra of PbSe QDs with OLA, NH4I, LiI, and KI ligands. **(B)** FTIR spectra of the same PbSe QDs presented in figure A. **(C)** TEM images of PbSe QDs with (from left to right) OLA, NH4I, LiI, and KI ligands respectively.

3.4.1 Quantum Dot Field-Effect-Transistors

PbSe QD films can be tailored to show *n*-type behavior when they are treated with chemicals such as hydrazine [57] or halides [90,94], or infilling with alumina [63]; while treatment with thiols, such as EDT [52,58,95], short chain acids [91], or exposure to air leads to *p*-type behavior [96]. Exposure to air is not an ideal circumstance because the oxide layer that forms introduces traps that can hinder charge transport [97], however it is an effective method to produce *p*-type or ambipolar behavior in PbSe QD films. In this report we implement an in-solution ligand exchange with primarily halide base ligands (*i.e.* LiI, KI, PbI$_2$, KBr, etc…), producing primarily *n*-type devices, while some devices display ambipolar behavior. Device cleaning used to separate

devices on a single substrate as well as clean the edges of the substrate is an important step for

reducing current leakage; **Figure 3.4.**
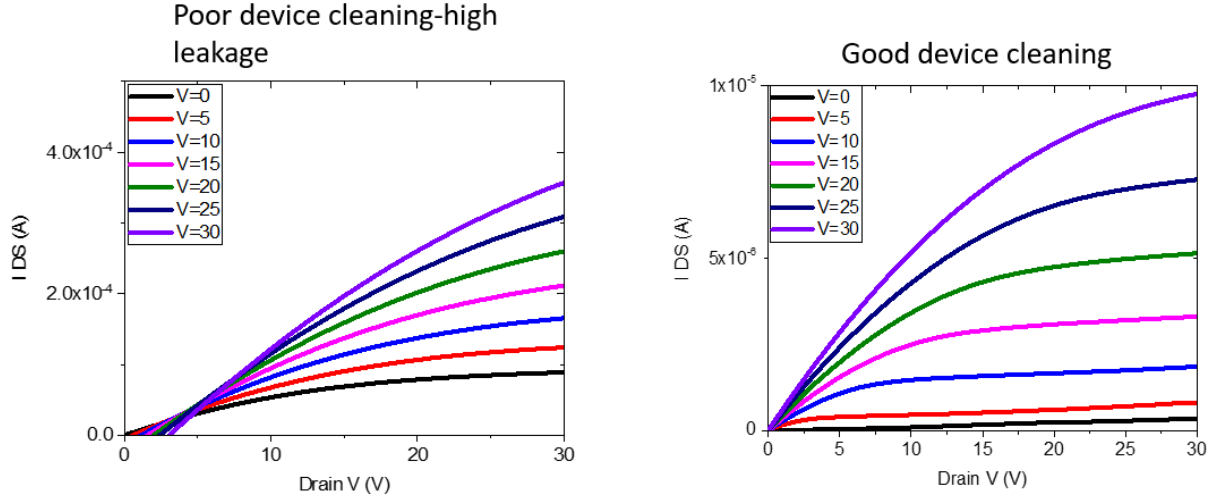
Figure 3.4 Examples of PbSe QD FETs with good (right) and poor (left) cleaning after deposition.

Carrier mobilities were calculated in the saturation regime, using the square root of the

transfer curve and *Equation 3.2.* Measurements of the transfer curve were taken by maintaining

a constant source to drain voltage (V_D) and measuring the output current (I) over a range of gate

voltages (V_G). An example of a typical transfer curve, as well as the points which were utilized to

extract electron mobilities is presented in **Figure 3.5.** The forward and reverse threshold voltage

(V_T) can be used to estimate the amount of trapped charges in the QD film, using *Equation 3.3.*

While the on/off ratio can be determined by dividing the current at high gate voltages (on

current) by the current at the lowest point of the transfer curve (off current).

$$n = \frac{C_i \Delta V_T}{e} \qquad\qquad Equation\ 3.3$$
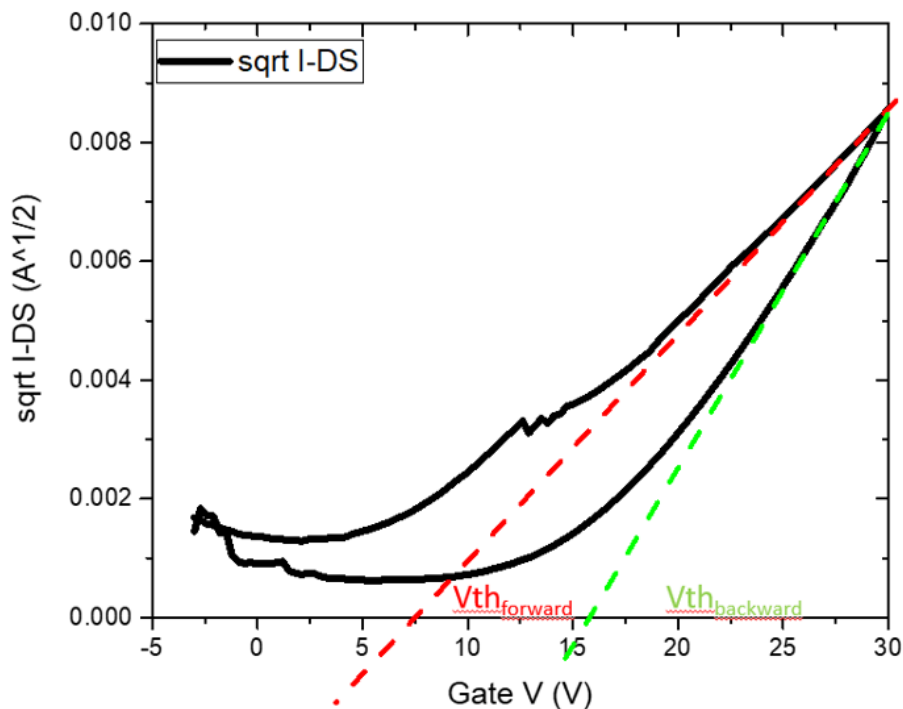
Figure 3.5 Example of a typical transfer curve, slope at high gate voltages, in the forward direction, are used to calculate carrier mobility.

Mobilities for Different Ligands

QD mobility has a strong dependence on ligand type, as well as whether the gold contacts were deposited before or after deposition of the QD film. Devices in which gold contacts were deposited on top of QD film display nearly an order of magnitude higher mobilities, which we attribute to better contact between the film and the gold, lower contact resistance, and better contact between the measuring probe and the QD film. **Table 3.1** summarizes the effect of contact placement for 3 separated ligands (NH_4I, LiI, and KI).

Table 3.1 Effect of contact placement on QD film carrier mobility

Ligand	Bottom contact mobility (cm^2/Vs)	Top contact mobility (cm^2/Vs)
LiI	.0021 ± .0013	.0425 ± .0303
KI	.0073 ± .0025	.0226 ± .0069
NH$_4$I	.0391 ± .0085	.1175 ± .0152

All the QD films prepared in this section were either *n*-type or ambipolar with an *n*-type dominance. KBr and ZnI$_2$ showed the most ambipolar behavior of all the ligands utilized, however these ligands suffered from poor electron mobilities (3.3 x 10^{-4} and 2.4 x 10^{-4} cm^2/Vs respectively). The ligand displaying the highest electron mobility was NH$_4$I (0.1175 cm^2/Vs), which was about 3 times higher than the next highest mobility which belonged to LiI. In general, the I$^-$ containing ligands displayed higher carrier mobilities than ligands containing some of their other halide counterparts (Br$^-$ and Cl$^-$). This trend is in agreement with what is typically seen in QD solar cells where ligand such as tetrabutylammonium iodide have been shown to increase PV efficiency. A surprising outcome from this experiment is even ligands containing thiols such as NaSCH$_3$ still produce films with predominantly *n*-type behavior, although they are slightly ambipolar. This is an indication that the *p*-type behavior typically seen in PbSe QD films treated with thiols such as EDT could be somewhat a result of excess sulfur atoms between to the PbSe QDs within a film. The output curves of 6 selected ligand are presented in **Figure 3.6,** while transfer curves measured under 30 V bias are presented in **Figure 3.7.** Both output and transfer curves confirm strong *n*-type behavior of the QD films. From the transfer curves we can also derive the on/off ratio, which is the ratio of current in the on-state vs current in the off-state, an important figure of merit in high performance FETs. In typical commercial FETs this ratio is around 10^6, while these PbSe QD FETs only display on/off ratio on the order of 10.
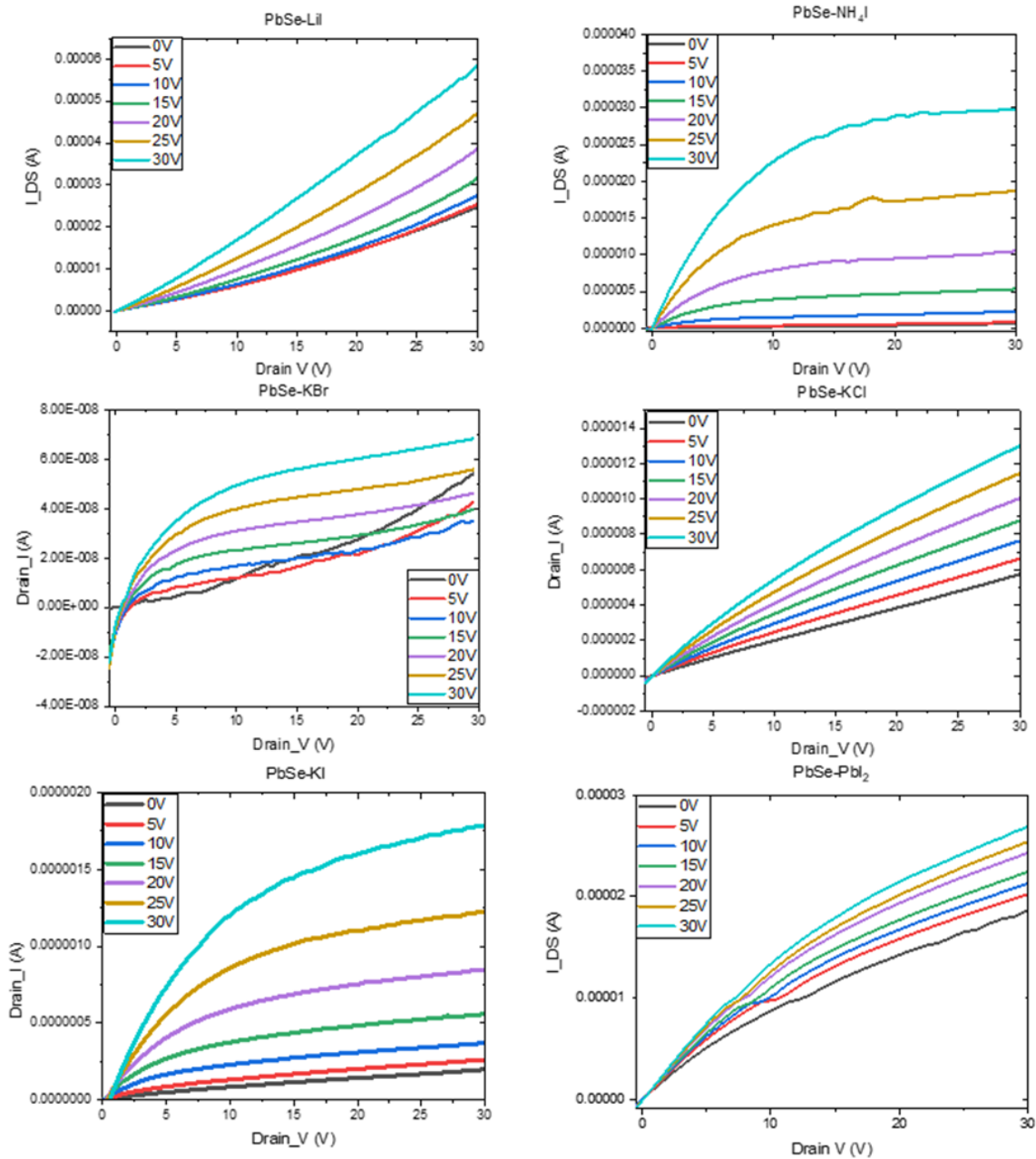
Figure 3.6 Typical output curves for PbSe QD FETs utilizing 6 selected ligands. On the left had side we have LiI, KBr, and KI (from top to bottom), while the right had side displays NH₄I, KCl, and PbI₂ (from top to bottom).
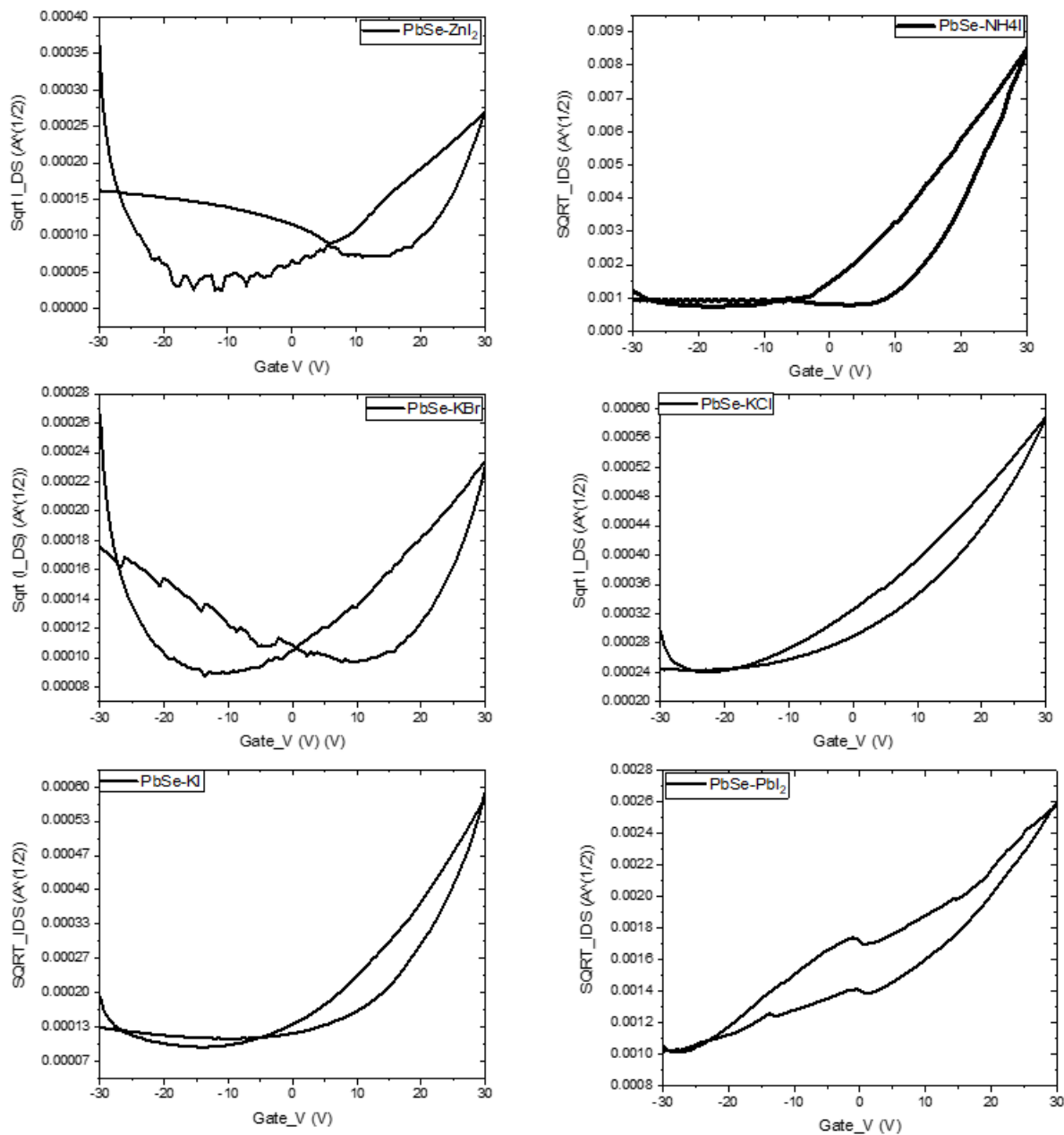
Figure 3.7 Saturation transfer curves measured at drain to source voltage of 30 V for PbSe QD films of various ligands. Left hand side (top to bottom) ZnI_2, KBr, and KI. Right hand side (top to bottom) NH_4I, KCl, and PbI_2

A summary of the figures of merit measured for PbSe QD films of various ligands can be seen in **Table 3.2**, including electron mobility on/off ratio, and average number of trapped

charges. The number of trapped charges is determined by the hysteresis between the forward and

reverse scans in the transfer curve measurements; this value gives an estimate of the number of

surface trap states located within the QD film.

Table 3.2 Summary of electron mobility, number of trapped charges and on/off ration for PbSe
QD films prepared with various ligands. Note all mobility values were derived from devices with
top gold contacts.

Ligand	Electron mobility (cm^2/Vs)	Number of trapped charges $(1/cm^2)$	On/Off ratio
LiI	$.0425 \pm .0303$	$1.9 \times 10^{12} \pm 7.0 \times 10^{11}$	19.4 ± 0.7
PbI$_2$	$.0039 \pm .0003$	$1.1 \times 10^{13} \pm 2.0 \times 10^{12}$	2.2 ± 0.5
ZnI$_2$	$.0002 \pm 3 \times 10^{-5}$	$3.7 \times 10^{13} \pm 2.6 \times 10^{12}$	4.7 ± 2.3
KI	$.0226 \pm .0069$	$8.6 \times 10^{12} \pm 1.5 \times 10^{12}$	5.8 ± 1.0
KBr	$.0003 \pm .00002$	$2.4 \times 10^{12} \pm 8.9 \times 10^{11}$	3.2 ± 1.1
KCl	$.0088 \pm .0037$	$9.2 \times 10^{12} \pm 2.0 \times 10^{12}$	2.3 ± 0.2
NH$_4$I	$.1175 \pm .0152$	$3.6 \times 10^{12} \pm 7.8 \times 10^{11}$	20.0 ± 4.6
NaSCH$_3$	$.0005 \pm .0002$	$3.3 \times 10^{13} \pm 7.3 \times 10^{12}$	9.7 ± 2.0

Effect of Size on carrier mobilities

QD size has powerful effects on QDs in solution, however QD size has also been shown

to affect the electrical properties within a PbSe QD film. Hole mobilities tend to increase with

QD size, while electron mobilities have been shown to peak when PbSe QD diameter is around 6

nm before falling off [98]. Herein we present a study on the electron and hole mobilities NH$_4$I

capped PbSe QD films, both with and without ALD in infilling with alumina. FETs were

fabricated using a bottom contact geometry which resulted in slower mobilities but allowed for

easier fabrication of devices. For ALD in-filling devices had to briefly be exposed to air, as we

do not have and ALD system built into the glovebox; in order to maintain consistency between

ALD in-filled devices and non-ALD in-filled devices we also exposed the non-ALD devices to

air briefly ($\approx$ 1 minute). The non-ALD in-filled devices displayed ambipolar behavior, while the

ALD in-filled devices were predominantly *n*-type. In-filling with alumina via ALD is accomplished by increasing the exposure time for each deposition step, essentially allowing the precursors to diffuse into the QD film, filling the voids between QDs. A schematic of the ALD in-filling process is presented in **Figure 3.8**.
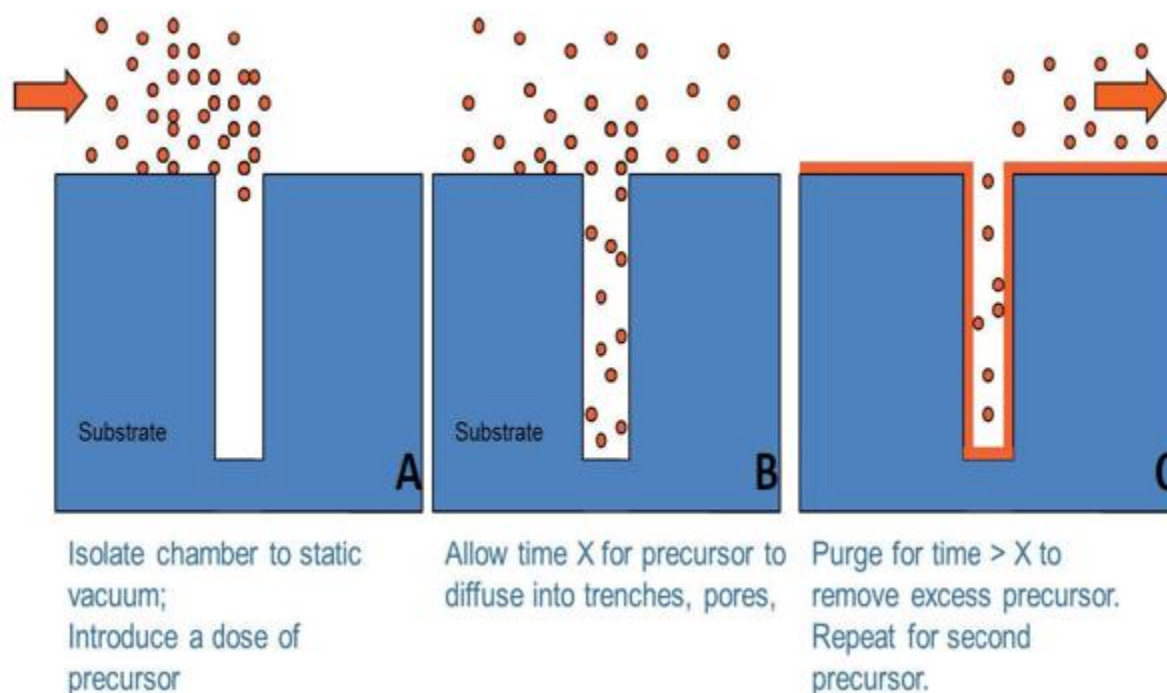
Figure 3.8 Schematic of the principle of exposure mode reprinted from the ALD user manual reference [99]. **(A)** Introduce precursor into the chamber **(B)** Allow time for precursor to diffuse into the spaces within the film **(C)** purge reaction chamber of unreacted precursors.

PbSe QDs were synthesized with diameters ranging from 4.9 to 13.1 nm; note: for larger cubic particles the "diameter" was measured from edge to edge not diagonally across the QD. NIR PL peaks of the particles ranged from ≈1400 nm to ≈3100 nm, and the PLQY systematically decreased from ≈5% for the smallest particles to > 1% for the largest particles. The PL spectra of the QDs are presented in **Figure 3.9,** as the PL peak pushes further into the infrared there is some

absorption due to the organic passivating ligands that causes the PL peak to be somewhat non-uniform [23].
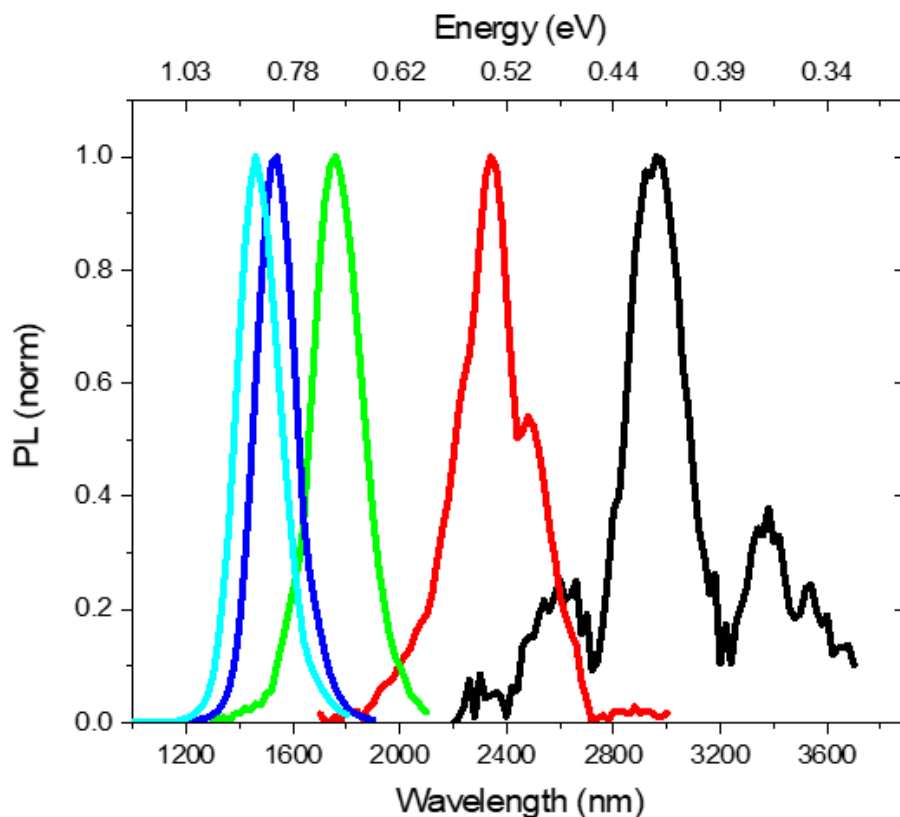
Figure 3.9 PL spectra of QDs ranging from 1400 nm to 3100 nm

PbSe QDs were prepared via the amine synthesis route, allowing for facile exchange to NH$_4$I passivating ligands. TEM imaging were used to analyze QD size before and after ligand exchange, as well as confirm closer packing of QDs on drop-cast films, **Figure 3.10.** The effect of ligand length on QD packing seems to be more pronounce in smaller QDs than larger QDs, however this could be a result of OLA ligands being stripped during the purification to prepare PbSe QD for TEM imaging.
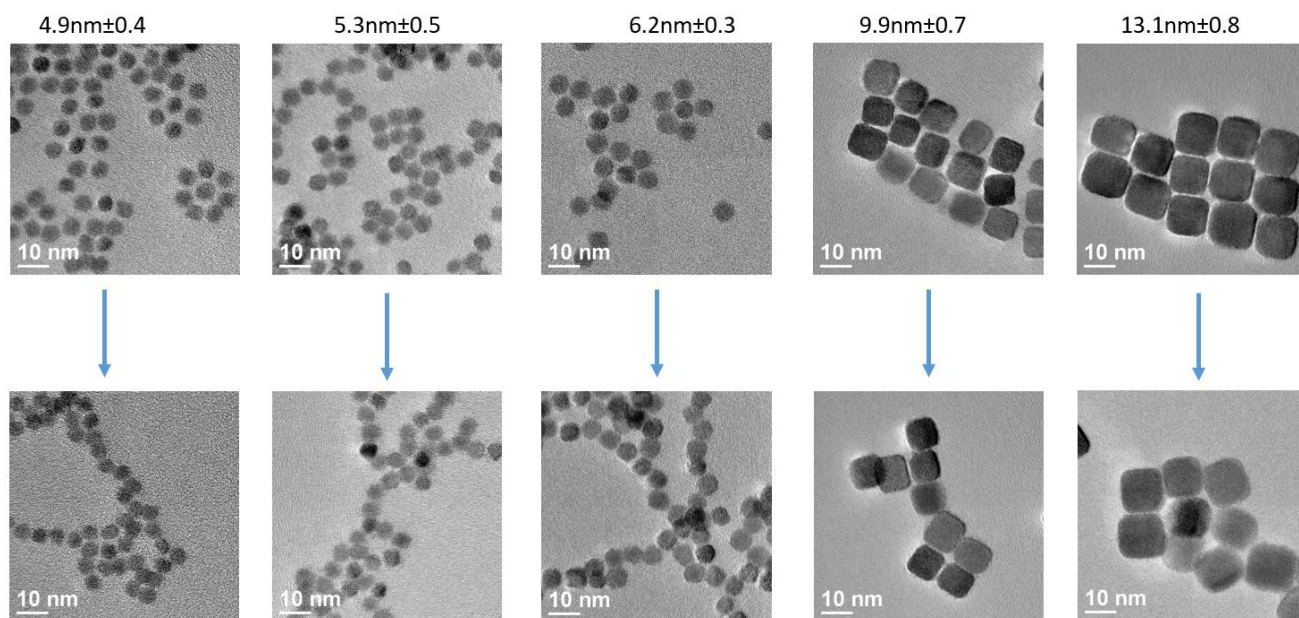
Figure 3.10 PbSe QDs of various sizes with OLA capping ligand (top), and after ligand exchange with NH₄I (bottom).

Transfer curve measurements on QD films without ALD in-filling show ambipolar behavior, along with reduced electron mobilities, likely as a result of the additional surface traps states due to QD film oxidation. The amount of trapped charges is also significantly higher in PbSe QD films exposed to air for a short period of time, compared to those that were only handled in inert atmosphere conditions from the previous section. In-filling with alumina increased the electron mobility in PbSe QD films with a smaller diameter; however, as the QDs became larger the effects became less pronounced, and non-ALD films displayed a slightly higher electron mobility for the largest QDs (0.035 vs 0.023 cm^2/Vs). Hole mobilities show almost no effect to ALD infilling for smaller QDs; in-fact for large QDs where the hole mobility is higher, in-filling with ALD decreased the hole mobility. One very noticeable impact of ALD in-filling is the reduction in trapped charges: nearly every film showed about an order of magnitude lower trapped charges when they had alumina in-filling. We attribute this to the

alumina passivating surface traps. **Figures 3.11 and 3.12,** display typical saturation regime transfer curves of the QD films; measurements were taken at a source-drain voltage of 30 V. **Figure 3.13 and Table 3.3** summarize the electron and hole mobilities, on/off ratios, and number of trapped charges for film of each size of QD.
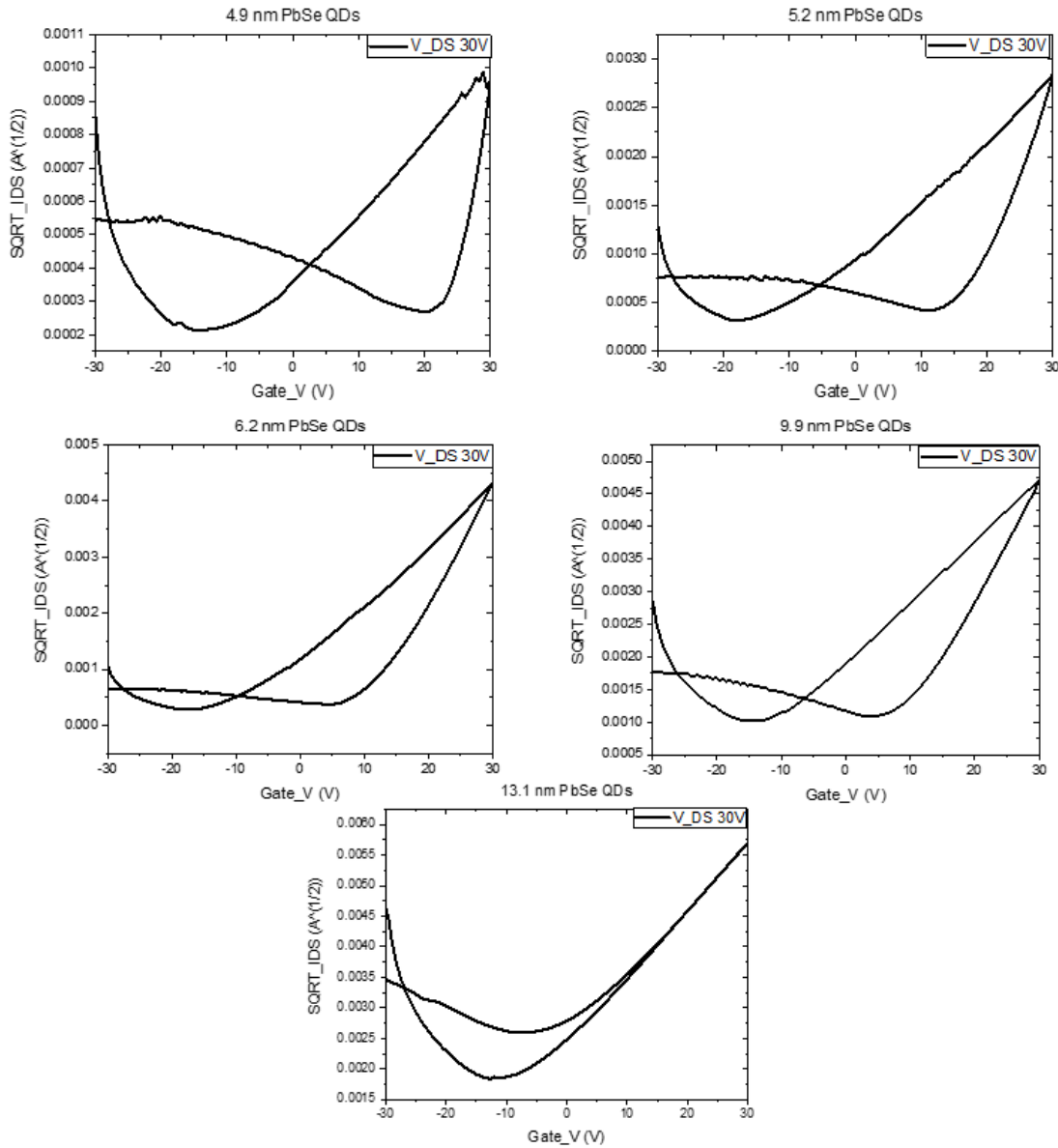
Figure 3.11 Saturation transfer curves of PbSe QD films of various sizes capped with NH$_4$I ligands. 4.9 and 5.2 nm diameter QD films (top), 6.3 and 9.9 nm QD diameters films (middle), and 13.1 nm QD film (bottom).
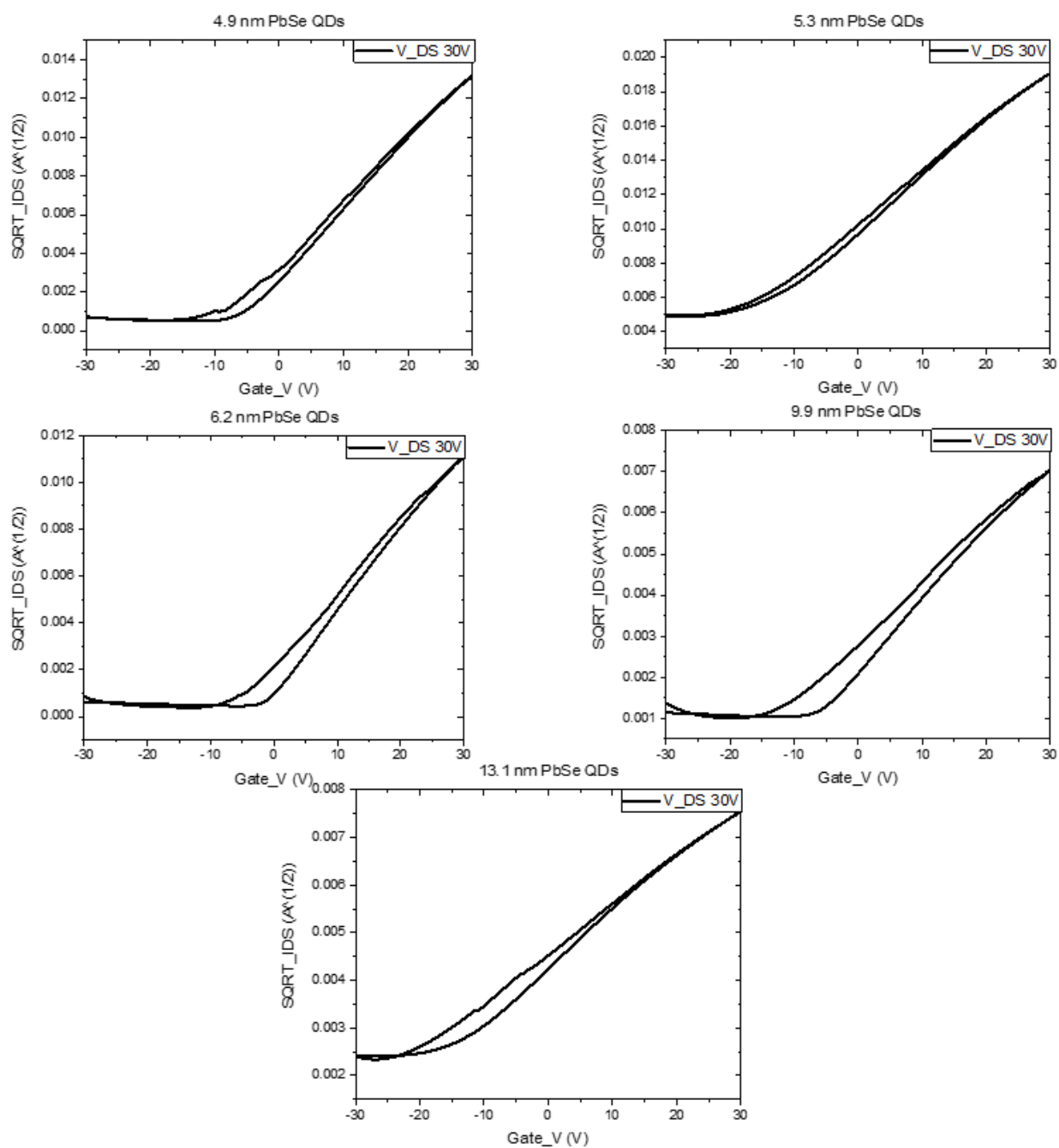
Figure 3.12 Saturation transfer curves of PbSe QD films of various diameters with ALD in-filling with alumina. 4.9 and 5.2 nm QD films (top), 6.2 and 9.9 nm diameter films (middle), and 13.1 nm diameter QD films (bottom).
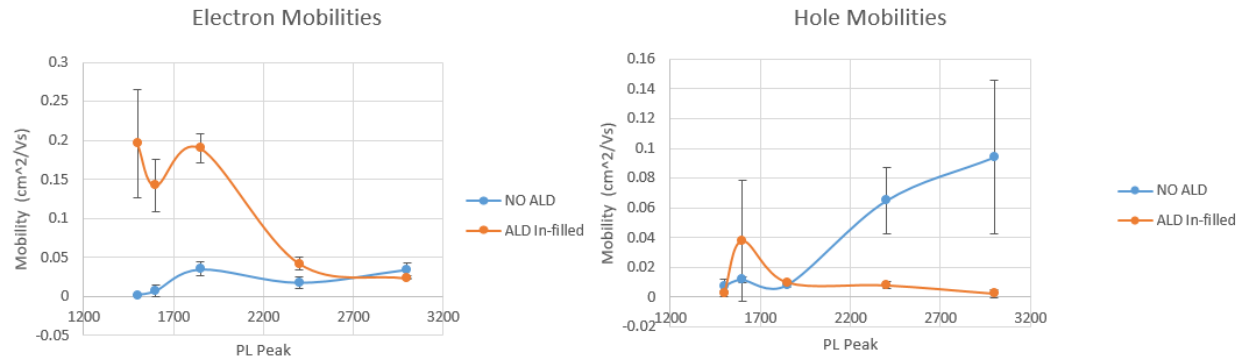
Figure 3.13 Graphical represntation of the electron and hole mobilites as a function of QD PL peak, for alumina in-filled and non-ALD QD films

Table 3.3 Summary of electron mobility, number of trapped charges, and on/off ratio for NH_4I capped PbSe QD films of various diameters with and without ALD in-filling.

PbSe QD diameter (nm)	Electron mobility (cm^2/Vs)	Electron mobility with ALD (cm^2/Vs)	Number of trapped charges $(1/cm^2)$	Number of trapped charges with ALD $(1/cm^2)$	On/Off ratio	On/Off ratio with ALD
4.9	$0.002 \pm .001$	$0.193 \pm .071$	$6.9 \times 10^{12} \pm 8.1 \times 10^{11}$	$4.3 \times 10^{11} \pm 5.2 \times 10^{10}$	5.0 ± 1.1	16.5 ± 3.1
5.3	$0.007 \pm .002$	$0.144 \pm .033$	$7.2 \times 10^{12} \pm 9.5 \times 10^{11}$	$3.8 \times 10^{11} \pm 2.0 \times 10^{10}$	7.8 ± 1.7	4.8 ± 0.7
6..2	$0.035 \pm .009$	$0.191 \pm .015$	$3.5 \times 10^{12} \pm 6.3 \times 10^{11}$	$4.7 \times 10^{11} \pm 5 \times 10^{10}$	12.0 ± 2.1	17.8 ± 2.9
9.9	$0.018 \pm .008$	$.042 \pm .008$	$5.3 \times 10^{12} \pm 7.4 \times 10^{11}$	$1.9 \times 10^{12} \pm 3.2 \times 10^{11}$	4.3 ± 0.6	7.0 ± 1.1
13.1	$0.035 \pm .008$	0.023 ± 0.001	$1.1 \times 10^{12} x 9.8 \times 10^{10}$	$4.3 \times 10^{11} \pm 3.7 \times 10^{10}$	2.5 ± 1.0	3.4 ± 0.7

The trends for electron and hole mobilites follow those presented by Liu *et al.* [98] with a peak in electron mobility at a QD diameter of 6 nm (PL peak ≈ 1800 nm) followed by a down turn, while hole mobilities increase with QD diameter. We do see a slight up turn in electron mobility for our largest dots, which is not shown by Liu *et al.*, however the size of dots (diameter ≈13.1 nm) used in this study was outside the range of their study.

3.4.2 Quantum Dot Capacitive Devices

Capacitive devices with a sandwich structure device configuration, as shown in **Figure 3.2,** can be used to calculate the carrier density of a QD film. Carrier density is a crucial property for devices such as photodetectors, where high carrier density can cause increased dark currents and the necessity to operate at high bias voltages. A typical C-V measurement performed at 1 kHz and the corresponding AFM measurement of film thickness is shown in **Figure 3.14**. C-V measurements must be made at low frequencies because at high frequencies the trapped charges at interface between QD and SiO_2 are measured due the charge dynamics in QD layer not being able to follow the fast frequency. In order to calculate overall number of charges present in the QD film, *Equation 3.3* is implemented, followed by division by the contact area (25 mm^2) and film thickness to find the carrier density (e$^-$/cm^3) in the QD film.

$$Q = \int_{V_T}^{V_G} C(V_G) dV_G \qquad\qquad Equation\ 3.3$$

The threshold voltage (V_T) can be found at the point at which the charges begin to accumulate (denominated by an upturn in the capacitance), while the V_G is labelled as the point where the capacitance saturates. In order to account for the charges produced by the Si the capacitance change seen during C-V measurements on blank substrates is subtracted.
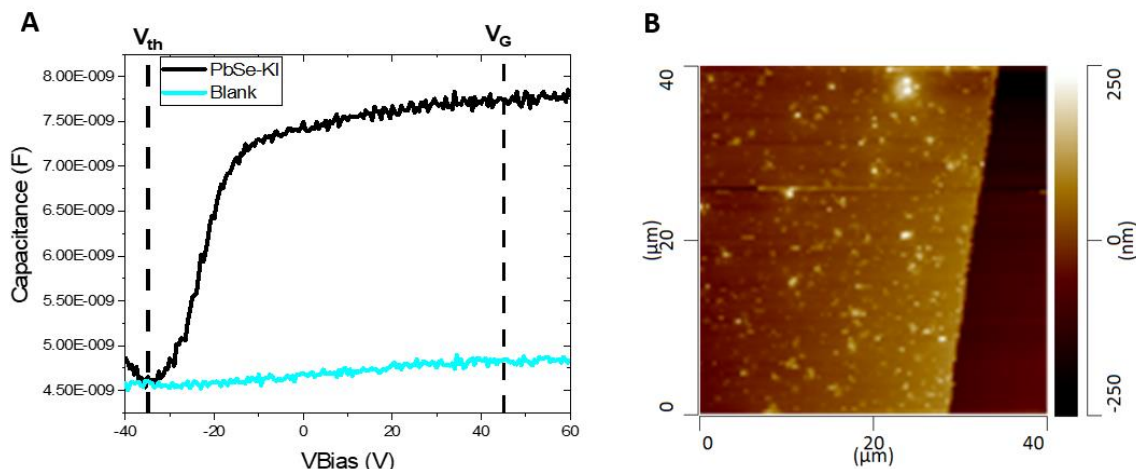
Figure 3.14 (A) Graph of Capacitance vs Voltage for measurements taken at a frequency of 1 kHz for PbSe-KI QD films and blank substrate (note blank substrate value is shifted down to threshold voltage capacitance of PbSe-KI film in order to account for change in total charges the Si is responsible for). **(B)** AFM scan of PbSe-KI film measured in (A)

Low frequency C-V measurements were done on several PbSe QD films, with various capping ligands and various film thicknesses. Carrier density was calculated using the forward scans, and measurements were performed multiple times, both on the same device and on separate device located on the same film in order to ensure that values were consistent. **Figure 3.15**, displays C-V scans performed at 1 kHz for various QD films, showing that the clear ability to modulate carrier density through choice of capping ligand.
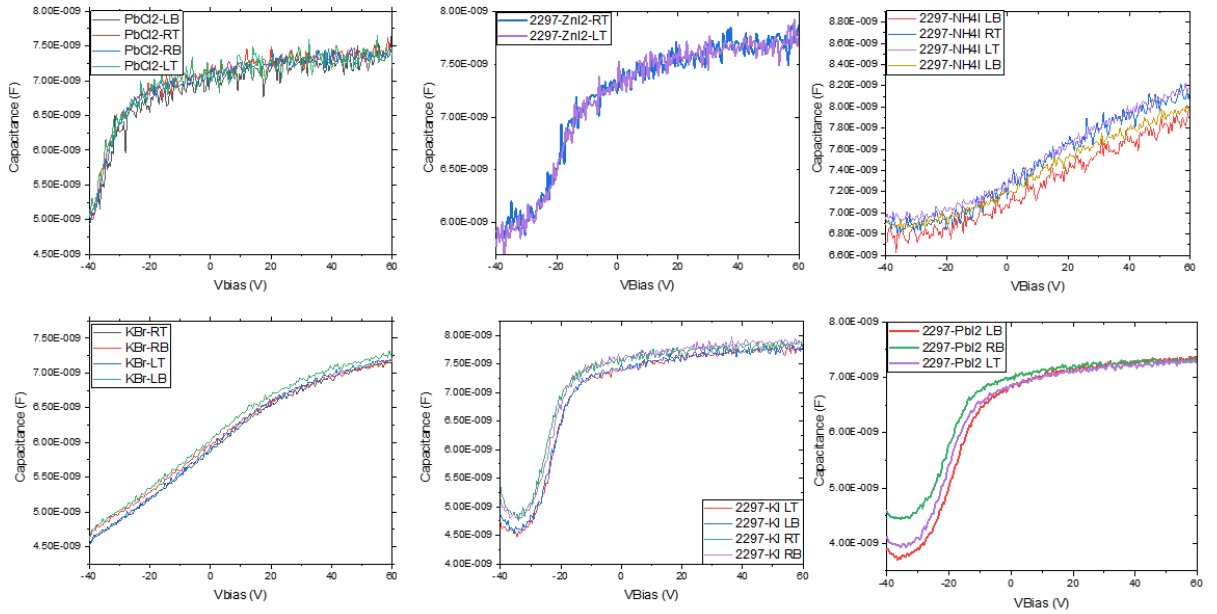
Figure 3.15 Forward C-V scans of PbSe QD films utilizing different ligands. $PbCl_2$, ZnI_2, and NH_4I (top). KBr, MI, and PbI_2 (bottom)

In order to ensure that the amount of charges remain constant over time and after repeated measurements, multiple measurements were made on the same film with about 15 seconds between each measurement, **Figure 3.16**. This allows us to ensure that the carrier density doesn't degrade overtime, and that charges are intrinsic to the QD film. Repeated measurements also probe whether the QD film remains charged after the previous measurement or if the device returns to its baseline of carriers. From **Figure 3.16**, we can see that the device does return to a baseline of carriers, and that the forward and reverse scans are nearly identical, which is important for implementation into detectors as each incident photon should have a reliable reading that is not affected by the previous event.
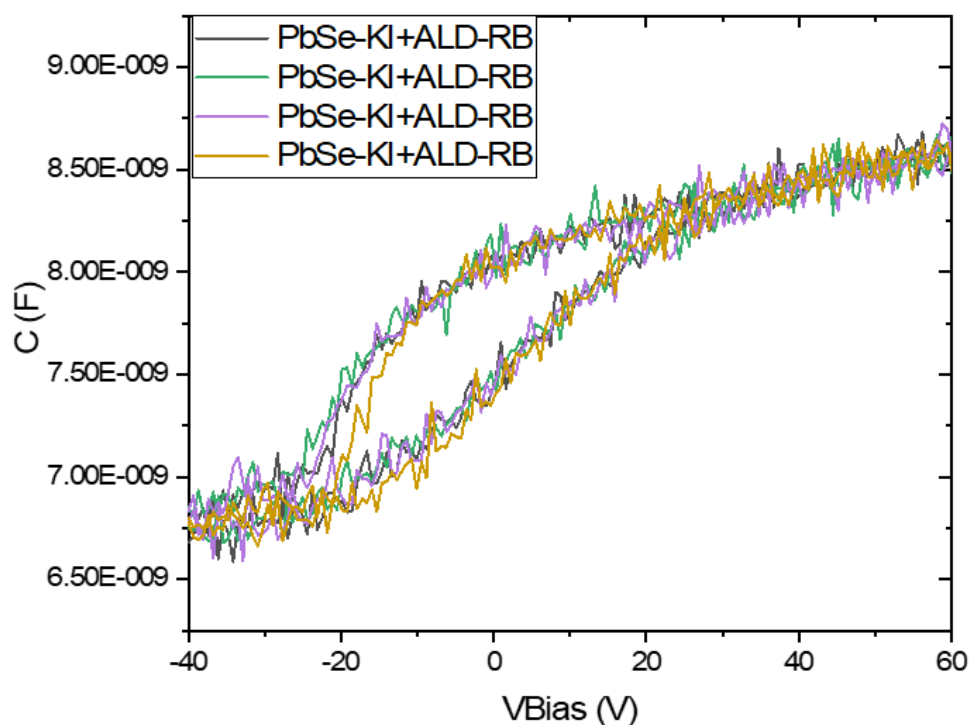
Figure 3.16 Output of repeated C-V measurements done on the same device, each measurement last about 1 minute, with 15 seconds between the subsequent scan.

Air exposure has long been a detrimental factor for PbSe devices due to them being prone to oxidation. However, halide treatments improve the air stability of PbSe QDs [22]. In order to determine the resilience of our devices to air exposure, we prepared 2 devices using KI capping ligands, one in air and another in ambient conditions. The device prepared in air displayed much lower carrier concentrations (5.55×10^{16} vs 1.23×10^{17} electrons per cm^3) which is to be expected. However, the device that was prepared in inert conditions and subsequently exposed to air showed very little negative effects to air exposure. This resilience to air exposure could be the result of the top gold contact behaving as protective layer, similar to the role of alumina encasing that Law *et al.* [63] demonstrated. **Figure 3.17** shows the forward and reverse C-V scans of both devices as well as the C-V measurement after the device prepared in inert conditions is exposed

to air. Surprisingly, the device prepared in ambient conditions did not display ambipolar behavior, we attributed this the film thickness, as films for C-V measurements were between 150-500 nm while films for FETs in the previous section were only about 20-40 nm.
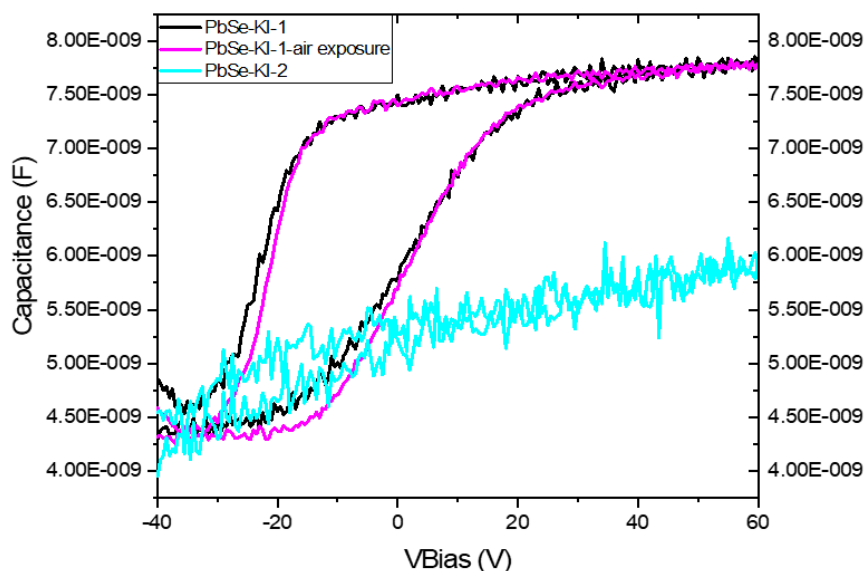
Figure 3.17 Comparison of C-V measurements PbSe QD films capped with KI ligands prepared in inert atmosphere and ambient conditions. File prepared in inert atmosphere at subsequently exposed to air showed very little degradation due to oxidation

Figure 3.**18** shows the calculated carrier density values for films of PbSe QDs with various ligands. In general, passivation with I^- anions display the highest carrier densities, which is understandable given their abundant use in QD solar cells often resulting in higher efficiencies. Pb^{2+} containing ligands also display higher electron densities compared to many of the other ligands tested, which is in agreement with what Kagan *et al.* [59] observed when making QD films with Pb rich surfaces. Overall a range of carrier densities spanning from ≈ 4.0 x 10^{16} to 2.1 x 10^{17} electrons per cm^3 is realized.
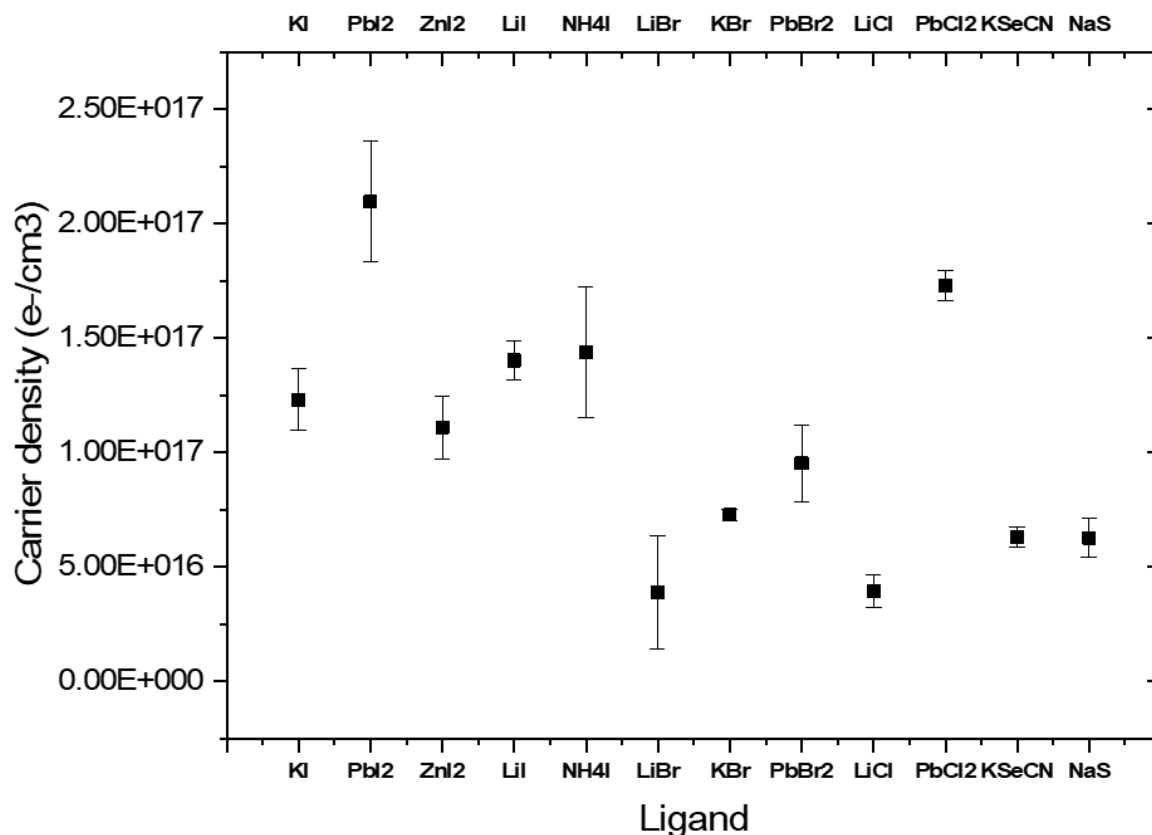
Figure 3.18 Calculated electron densities for PbSe QD films with various capping ligands.

Table 3.4 combines the results of carrier density calculations with FET electron mobilities using the same ensemble of QDs. NH4I displays an impressive mobility of 0.13 cm^2/Vs, which is a factor of 3 higher than LiI, even though they have similar carrier densities. PbI_2 exhibits carrier mobilities an order of magnitude lower than LiI despite having higher carrier density, while KBr clearly shows the lowest mobility and density. These results can be used to implement PbSe QDs capped with ligands that display high mobilities with manageable carrier densities into high energy photon detectors, where high dark currents are an inhibiting factor to detector sensitivity.

Table 3.4 Electron mobilities and densities PbSe QD films with various selected capping ligands

Ligand	Electron Mobility (cm^2/Vs)	Carrier Density (cm^{-3})
LiI	0.042 ± 0.030	$1.40E+17 \pm 8.43E+15$
KI	0.022 ± 0.007	$1.23E+17 \pm 1.34E+16$
NH_4I	0.130 ± 0.018	$1.44E+17 \pm 2.87E+16$
PbI_2	0.004 ± 0.0003	$2.09E+17 \pm 2.65E+16$
KBr	0.0003 ± 0.0001	$7.26E+16 \pm 2.32E+15$

3.4.3 Radiation Detection

In the previous two sections we have identified KI and NH_4I as ligands with relatively high mobilities and workable carrier densities. Here we implement PbSe QDs capped with these ligands into simple photodetectors and alpha radiation detectors. Alpha radiation measurements were made in dark conditions using various Americium 241 (^{241}Am) sources as the source of alpha radiation. PbSe QDs with 1S absorption peaks at 1150 and 1550 nm (1.1 and 0.8 eV respectively), **Figure 3.19 (A),** were synthesized using the amine route, and ligand exchanged with KI and NH_4I. Devices fabricated with the larger QDs capped with NH_4I utilized ZnO as a hole blocking layer between the bottom ITO electrode and the QDs in an effort to reduced dark current, **Figure 3.19 (B).** Schematics of the two types of devices fabricated can be seen in **Figure 3.19 (C and D)**. In short, a thick PbSe QD film was prepared via spin-coating a concentrated (≈60 mg/mL) solution of QDs onto ITO glass and a top gold contact (50 nm) was prepared vis thermal evaporation through a mask.
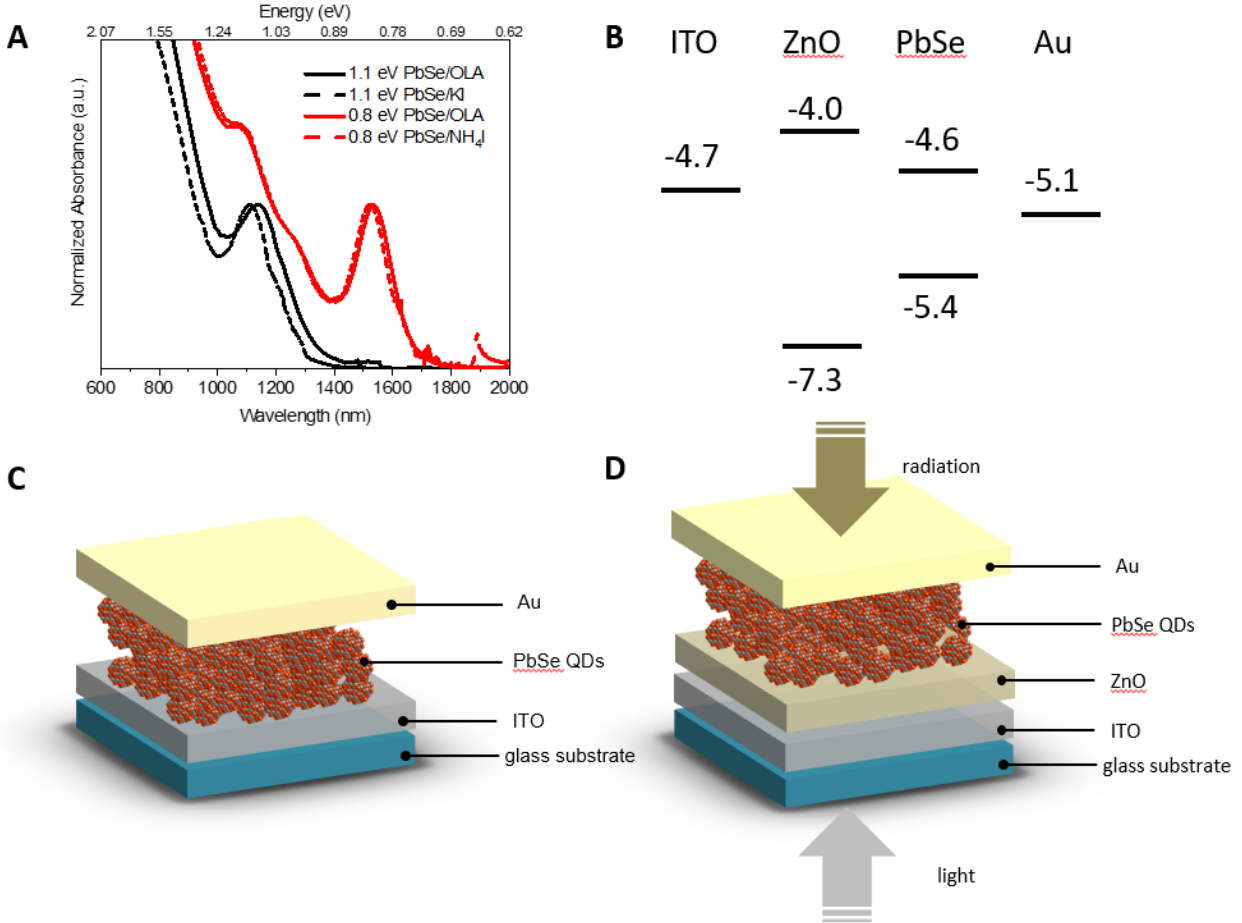
Figure 3.19 (A) Absorption spectra of PbSe QDs used in radiation detection measurements **(B)** Band position of layers in radiation detection devices utilizing ZnO as a hole blocking layer **(C)** Schematic of a radiation detection device without ZnO hole blocking layer **(D)** Schematic of device with hole blocking ZnO layer

To ensure that devices were indeed responsive to incident photons, a control experiment in which photocurrent response to varying intensities of incident light was performed. In **Figure 3.20 (A),** the results of the control experiment show that photocurrent as a result of incident light is nearly linear with intensity, with values of 1.94, 3.16, and 3.92 nA for incident illuminations of 13.6, 21.8, and 25.9 W/cm^2 respectively at 20 V bias. Response to alpha radiation began to deviate slightly from the dark current values when exposed to a 1 µCi source, however the

response became significant when exposed a 10 µCi source, **Figure 3.20 (B).** Exposure to 100 µCi alpha source shows even higher photocurrent than the exposure the 10 µCi source indicating that strength of radiation can be detected by PbSe QDs, however the response isn't linear as it was with incident light.
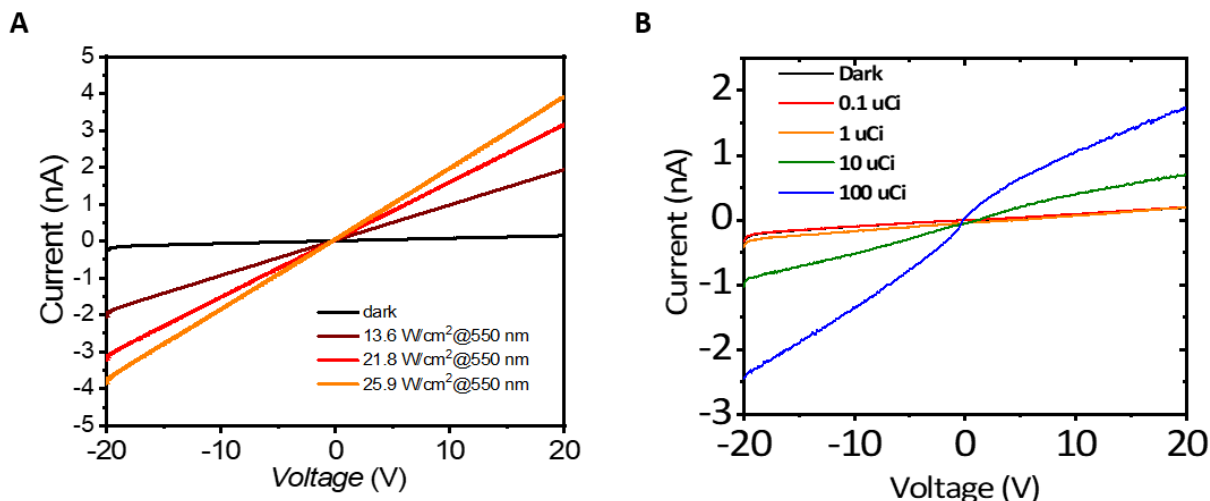
Figure 3.20 (A) Photoresponse of PbSe QD films capped with NH$_4$I ligands utilizing a ZnO hole blocking layer to different light intensities **(B)** Response of same QDs as in (A) to exposure to vary degrees of alpha radiation

Forward and reverse scans during alpha source exposure were performed, for the strongest sources there is some hysteresis at positive bias voltages, as seen in **Figure 3.21 (A)**. An important parameter in detection applications is the signal-to-noise ratio, which is ratio of current during a detectable event versus the dark current. Signal-to-noise ratio for the device incident with 100 µCi source peaks at low positive biases (≈45 at 10 V bias) and settles at around 18 at 100 V positive bias, **Figure 3.21 (B)**. Signal-to-noise ratios at negative biases are slightly lower than they are at positive biases. Improvement of signal-to-noise ratios can possibly be accomplished by utilizing an additional layer of a conductive 2D material (see next Chapter) to

improve carrier mobility for increased signal during a detectable event; however, this may also increase dark current. Another option is to implement a more robust hole blocking layer.
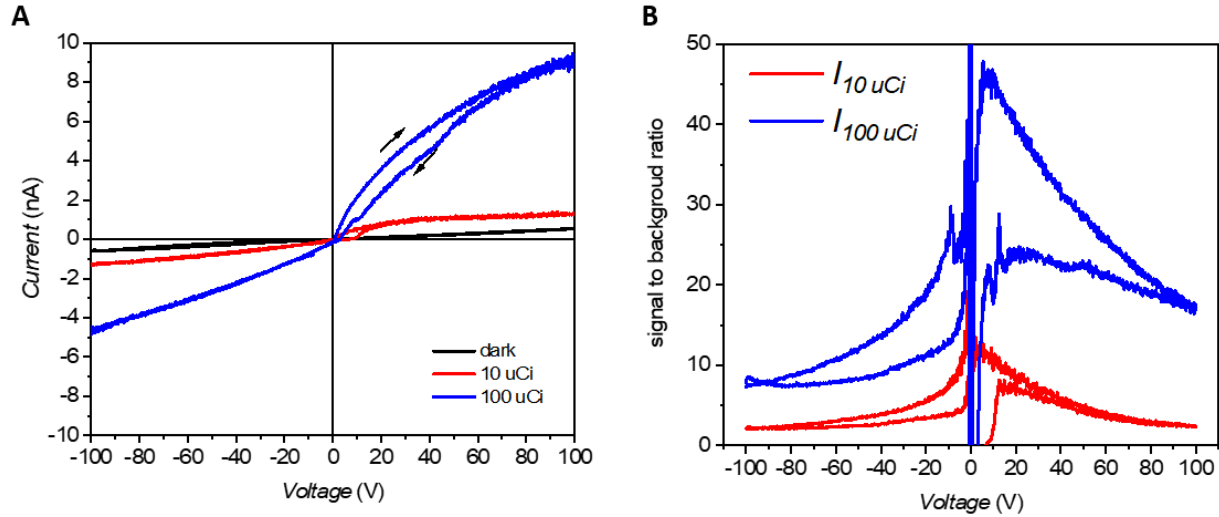
Figure 3.21 (A) Output current of PbSe-NH$_4$I QDs with ZnO hole blocking layer in dark conditions as well as under exposure to 10 and 100 µCi alpha sources. **(B)** Signal to noise ratio of devices

On/off characteristics measured using a paper to block alpha radiation at a bias of -20 V with a 10 µCi source, show that the device does respond and the current during the on state (higher negative current in this case) is consistent. The rise and decay times are quite long though with values of 0.14 and 0.20 seconds respectively, **Figure 3.22**, but this may be a result of the measurement conditions, as these measurements did not employ a mechanical shutter to block/allow radiation. Minimizing rise and decay times is of great importance in detectors that see a high number of detectable events or detection of fast-moving particles, as a lapse in time can result in a loss of a significant amount of data about said event or particle.
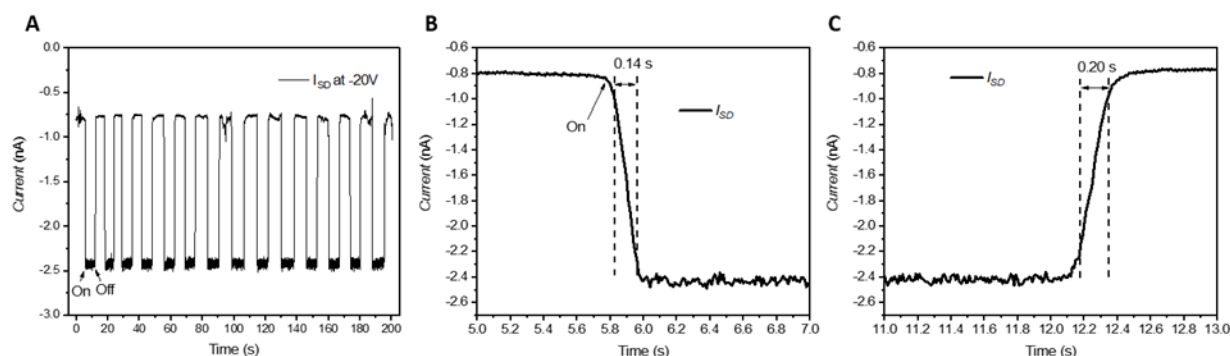
Figure 3.22 (A) On/Off characteristics of PbSe-NH$_4$I devices using ZnO hole blocking layer. **(B)** Decay time after exposure to alpha source is removed. **(C)** Rise upon exposure to alpha radiation. All measurements performed at a bias of -20 V

Recovery of devices after prolonged periods of exposure to radiation is an important variable, as the ability to detect a future event should not be hindered by the detection of previous events. PbSe QD devices capped with KI ligands, with no hole blocking layer, show a reduction in dark current after soaking in radiation for 16 hours. However, the output current upon exposure to an alpha source of 100 µCi is relatively consistent, only showing a slight decrease after soaking, **Figure 3.23 (A)**. In **Figure 3.23 (B),** the output current of measurements made 2 minutes apart on the same device, PbSe with NH$_4$I ligands and a ZnO hole blocking layer, is shown to be repeatable. Repeatability is another important factor for a detector, as events with the same magnitude of detectable radiation should result in the same output regardless of the amount of time between events. The effect of distance between the source of radiation and the detector is probed in **Figure 3.23 (C).** Minimal effect is registered under negative applied bias, however under positive bias there is a noticeable difference in magnitude of output current. Accurately determining distance can be a valuable asset in surveying applications.
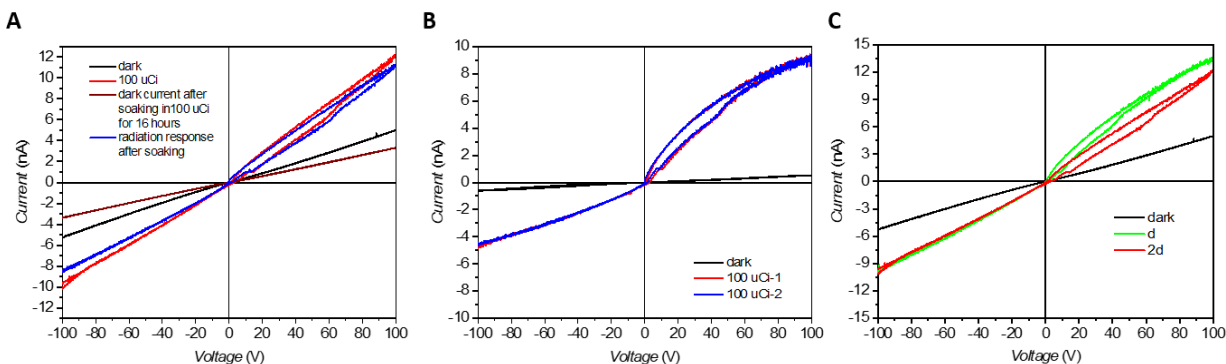
Figure 3.23 (A) Response of PbSe-KI devices before and after soaking in radiation for 16 hours. **(B)** Repeatability of measurements on PbSe-NH₄I devices with hole blocking ZnO layer, measurements were taken 2 minutes apart. **(C)** Effect of distance of alpha source from device (PbSe-KI)

In the final measurements, we tried to determine whether PbSe QD films have sensitivity to gamma rays, which is a much more penetrating form of radiation. Measurement of gamma ray sensitivity is determined by using a paper to block the alpha radiation emitting from the [241] Am sources, essentially allowing only gamma radiation to incident the devices. Results of preliminary gamma radiation studies are shown in **Figure 3.24**. There is minimal response to gamma radiation in both the NH₄I and KI capped PbSe QD films, however for the KI films the signal is slightly above the range of error bars of measured dark current at high bias voltages. Possible routes for improvement of gamma radiation include producing thicker films to increase the stopping power of the devices and incorporating either a 2D layer or some other material to improve carrier transport within the film.
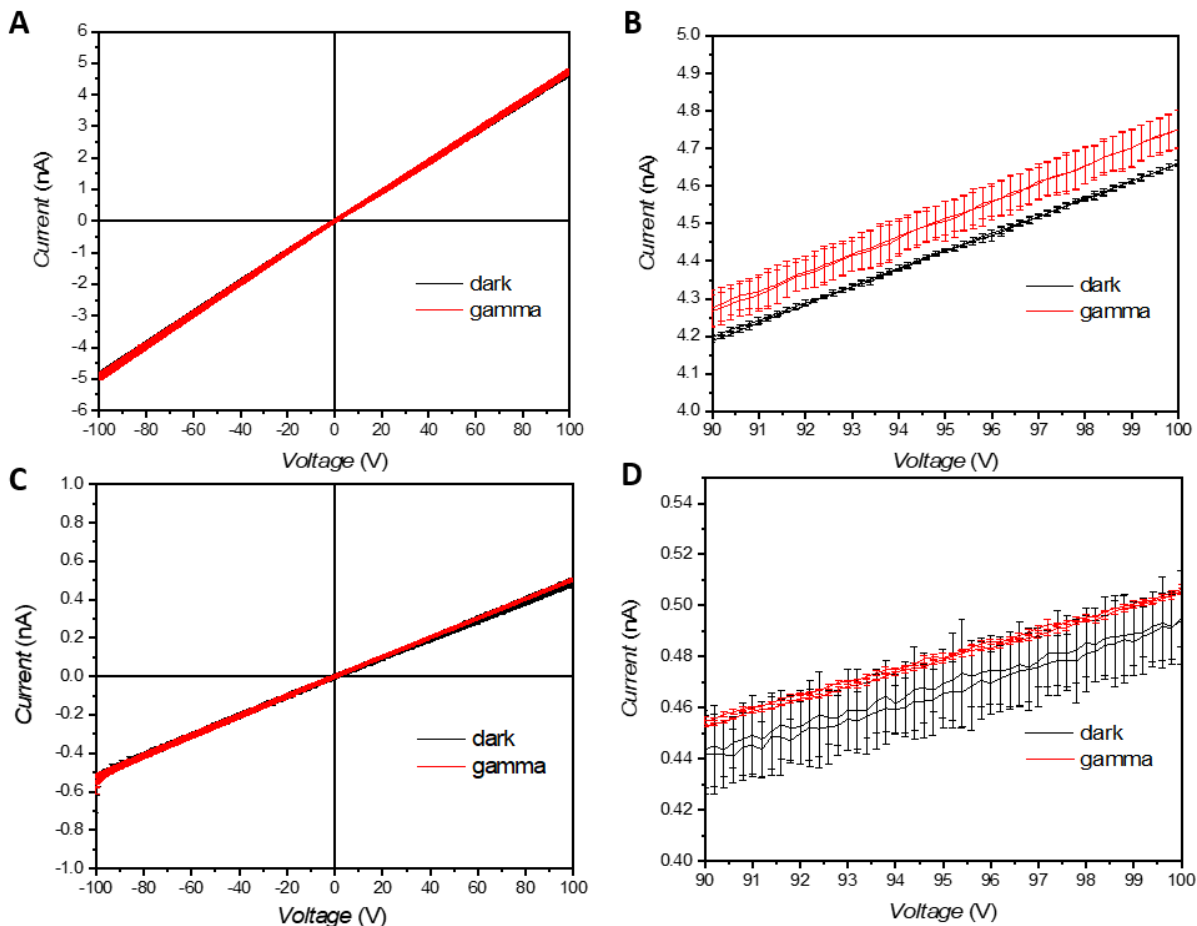
Figure 3.24 (A) Response under gamma radiation of PbSe-KI devices **(B)** Same as (A) zoomed in at high bias voltages **(C)** Gamma radiation response of PbSe-NH$_4$I devices utilizing a ZnO hole blocking layer **(D)** same as (C) zoomed in at high bias voltages.

3.5 Summary

In this section PbSe QDs were synthesized using the amine synthesis route, facilitating facile in-solution ligand exchange to shorter ionic ligands. The electron mobility of PbSe QDs capped with various ligands was probed using simple FET devices to determine which ligands displayed the fastest mobilities, with NH$_4$I reaching a mobility of on the order of 0.1 cm^2/Vs. The location of the gold electrodes played a crucial role in the measured mobility, with contacts

located on top of the QD film displaying around an order of magnitude higher mobilities. Capacitance devices were fabricated to determine the intrinsic carrier density of PbSe QD films. For the first time it was explicitly shown that carrier density modulation can be accomplished through in-solution ligand exchange, which is less laborious than previous examples of carrier density modulation which all employed post deposition film treatments that can require several hours to accomplish. Combining results of carrier mobility and carrier density measurements, KI and NH4I were identified as ligands that could be implemented into radiation detectors. PbSe QD films showed tangible response to incident alpha radiation, the magnitude of which was tunable by the applied bias. To our knowledge this is the first report of response to alpha radiation in PbSe QD films. Factors for improving dark current and device sensitivity still need to be explored, especially for the detection of high energy radiation such as gamma rays. Current devices show modest response to gamma radiation; however, these results are only slightly outside the error of dark for PbSe QD devices utilizing KI as a capping ligand and fall within dark current error for NH4I capped devices.

Chapter 4: Critical Review of Hybrid PbE (E= S, Se) Colloidal Quantum Dot- Layered 2D Material Hybrid Photodetectors

4.1 Introduction and Background

Lead chalcogenide (PbE, E= S, Se) quantum dots (QDs) are desirable materials for implementation in photodetectors because of their potential for improving upon current technologies in the NIR and mid-IR spectral regions [51,83,100,101]. Improving capabilities in this region is of large consequence for applications in environmental monitoring [86,102,103], motion sensing [87], fiber-optic communications [88,104], X-ray detection [105], and biological imaging [106], where Pb based QDs have been shown to be less destructive to cells than there Cd based counterparts when coated with silica. PbE QDs have size-tunable bandgaps from 800 nm – 4000 nm (1.55 eV - 0.31 eV) [23,107], as shown in **Figure 4.1 (A)**, and their solution processability allows for facile integration onto both rigid and flexible substrates through spin-coating, dip-coating, and ink-jet printing [49,83]. The ease with which QD solutions can be integrated, as sensitizers for the NIR wavelength regions into current silicon based technologies, which are based on CMOS architectures make them ideal candidates for further study [108]. Along with the profound effect size has on the properties of QDs, altering the surface chemistry via ligand exchange or other post-deposition treatments can also greatly alter the physical and electronic properties of QD films [56,58,66,82,95,98,109], affecting properties such as carrier type and the smoothness of the QD film. Quality PbS QD photodetectors were initially reported in 2005 by Sargent, *et al.* [45]; during the years since then many efforts have been made to understand and improve QD devices [37,50,82,110-112].

Successfully absorbing incident photons and collecting the photogenerated carriers from the QD film is paramount to fabricating QD-based photodetectors. PbE QDs are strong absorbers that efficiently convert incident photons into electron-hole pairs (excitons), even displaying carrier

multiplication, which is the generation of multiple excitons per single absorbed photon with an energy of 2 or more times greater than the bandgap of the QD [24,84,113]. The discovery of carrier multiplication in PbE QDs created momentum for the QD solar cell path [114-120], which led to many studies and advancements on carrier transport in QD films [50,98,121,122]. Many of the lessons learned by studying other QD devices such as solar cells [54,55,123-130] and, in the case of visible emitting QDs, LEDs [89,131-133] can be applied to QD photodetectors because the key point of focus in many of these studies was enhancing carrier mobility and collection.

Low carrier mobility in QD films, which prevents photogenerated carriers from being collected before recombining with the opposite carrier or with a "trap" state, continues to be a pressing issue for the improvement of QD devices [50]. QD films intially suffered from very poor charge transport because of long insulating ligands [46,89,134]. Colloidally synthesized QDs are stabilized in solution by long organic ligands that are attached to the QD surface, which prevent them from precipitating out of solution when in colloidal form, but inhibit charge transport when QDs are incorporated into a film. In order to decrease the inter-QD spacing within films, long chain ligands can be either be exchanged with other shorter ligands [46,52,58,98] or stripped off all together [135,136]; often, this is accomplished by application of layer-by-layer deposition techniques. Layer-by-layer ligand exhange is a process in which a QD film is deposited onto a substrate, typically by dropcasting or spin-coating, and then subsequently exposed to a solution of a shorter ligand (*e.g.* 1,2-ethanedithiol in acetonitrile), affecting replacement of native ligands and allowing QDs to come into closer contact. Ligand exchange is only effective for a deposited QD film sufficiently thin to allow for complete solution penetration, and typically results in voids or "cracks" due to the loss of volume previously taken up by longer ligands. Thus, repetition is required, making layer-by-layer deposition laborious and time consuming, particularly for thicker films. In 2017 Lin *et al.* [32]

introduced a universal method for in-solution ligand exchange of PbE QDs with short ionic ligands, allowing for the deposition of thicker films and removal of post deposition ligand exchange step. Regardless of approach, decreased QD-QD spacing improves the mobility of carriers through increased coupling, making it easier for charge transport to occur either by tunneling or thermally assisted carrier hopping [50,98]. It has also been observed that majority carrier type [109] (*i.e.* *n*-type [90] or *p*-type [91]) as well as the position of valence and conduction band [56] can also be controlled by modifying the surface chemistry of the QDs through ligand exchange, as shown in **Figure 4.1 (B)**. Altering the positions of energy bands via ligand exchange can open pathways of band-alignment engineering in which a QD film's energy levels can be altered to better interact with other layers in the device [55], a technique that was used, for instance, to create a "carrier funneling" effect in QD solar cells [123,124]. Modifying the composition of QDs, either on the surface via ligand exchange or "colloidal atomic layer deposition" [60], or interally through impurity doping [21], also leads to significant effects on the electronic transport properties of the QD film. In one example, **Figure 4.1 (C)** shows the transition from *p*-type to *n*-type transport with the addition of excess Pb on the surface of PbSe QD solids, indicating the role of surface stoichiometry on transport characteristics. Gas-phase atomic layer deposition (ALD) of materials such as alumina has been used to great success for improving carrier mobility [63,64], unlocking carrier multiplication in PbE films [66], and improving air stability. In ALD, a substrate is coated with a material one atomic layer at a time by controlled exposure to one or more reactive gas- or vapor-phase precursors. For QD films, the film can be encased by a layer of the material on top of the film, generally enhancing stability, and/or "infilled", wherein essentially all voids between QDs are filled with the material [64], which produces enhanced QD-QD coupling and correspondingly larger effects on transport. As the extreme case of enhanced mobility, the

possibility of band-like transport in highly coupled QD solids is being pursued vigorously, with some promising prospects, including report of carrier mobilities of QD films reaching values [65] of 24 cm^2/Vs.
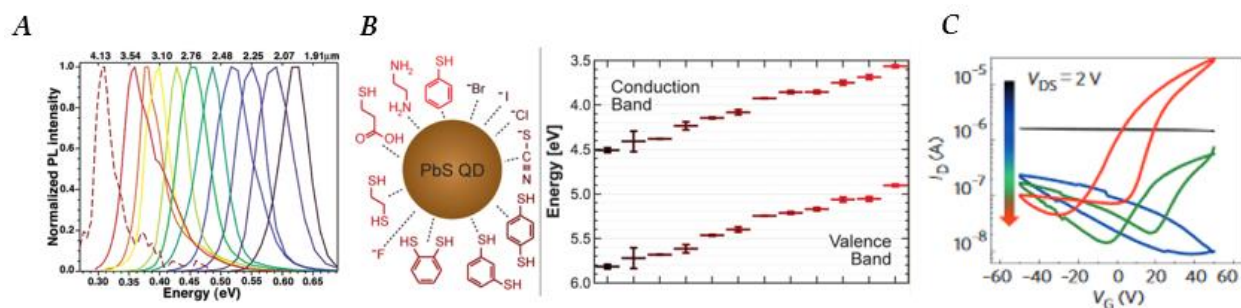
Figure 4.1. **(A)** Photoluminescence spectra of PbSe QDs of varying sizes, as an indication of bandgap tunability; **(B)** Illustration of a PbS QD with various types of ligands (left), and the corresponding (by color) conduction and valence band energy levels each ligand produces (right). The positions of the valence and conduction bands of PbS QDs with different ligands are presented in the graph to the right. Beginning with Br$^-$ (brown color, lowest band postions) moving clockwise around the schematic of the QD until it reaches benzenethiol (red color, highest band positions). **(C)** Transfer characteristics of a 5.9 nm PbSe QD film after solid-state exchange with Na$_2$Se (black), which removes long oleate ligands and enriches the surface in Se, and subsequently upon PbCl$_2$ treatment for durations of 1 h (blue), 6 h (green) and 12 h (red) at 65 °C, which enriches the surface in metal. I$_D$, drain current; V$_G$, gate voltage; V$_{DS}$, drain–source voltage. *Figures reprinted (adapted) with permission from; (A) Ref. [23]. Copyright (2004) American Chemical Society. (B) Ref. [56]. Copyright (2014) American Chemical Society. (C) Ref. [60]. Copyright (2014) American Chemical Society*

However, these values pale in comparison to those of layered 2D materials such as graphene, which can have carrier mobilities of up to [137] 15000 cm^2/Vs. Layered 2D materials have been of interest for optoelectronic devices due to their promising characteristics and physical versatility,

since the successful isolation, through micromechanical cleavage, of a single graphene layer in 2004 [138]. Layered materials have strong in-plane bonding but weak layer-to-layer bonding through van der Waals interactions, enabling cleavage or exfoliation into two-dimensional layers of single unit cell thickness [139,140]. Graphene is an especially interesting material for broadband photodetection purposes because it has zero band-gap, meaning that it absorbs light over a wide range of photon energies, from the UV to far-infrared [141-145]. Additionally, graphene displays ultrafast carrier dynamics [146-148], tunable optical properties via electrostatic doping [149-151], and high carrier mobility [152-155]. The high carrier mobility enables ultrafast conversion of photons to electrical currents or voltages [156,157]. However, the lack of a bandgap in graphene makes it difficult to fabricate devices with low dark current and high on/off ratios because of the presence of free carriers. Techniques such as fabricating graphene nanoribbons via nanostructuring [158-160], nanopatterning to create a graphene nanomesh [161,162], and chemical functionalization [163-166] have been used to engineer a bandgap in graphene [167]; however, these processes often lead to dimished mobilty and add unwanted steps and cost to the fabrication process.

Although graphene has been at the foreront of layered 2D materials research, transition metal dichalcogenides (TMDs) and other layered 2D materials such as phosphorene [a single 2D layer of black phosphorous (BP)] have also shown promise for potential applications in which a non-zero bandgap is advantageous [140,168]. Phosphorene has a unique 2D structure [see **Figure 4.2 (B)**], which causes it to display anisotropic carrier mobility [169], meaning that mobility within the plane is dependent on the direction in which the carrier is traveling. Phosphorene is also highly unique in that it displays *p*-type characteristics [169], and a high work function [170] making it a valuable material for hole transport and hole injection [171]. **Figure 4.2** shows the energy band structures of graphene, phosphorene, and MoS_2, a TMD that is one of several that display a transition from

indirect to direct bandgap as the sample is reduced from bulk to single monolayers [172,173], which

is key for efficient photon absorption [139]. Photodetectors utilizing layered 2D materials have been

widely reported [157,171,174-180] as have studies on charge transport and electronic properties of these

materials [181-188]; however, the relatively low absorption, attributable to the atomically thin profile

[189], remains a serious challenge.
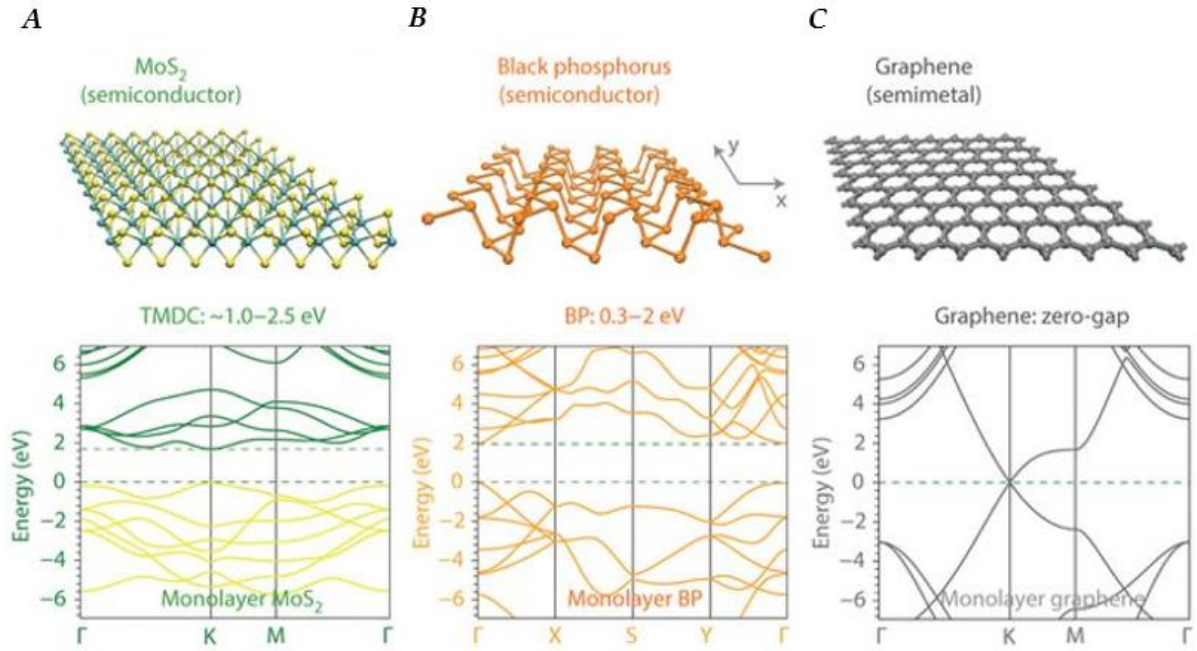
Figure 4.2. Single-layer atomic structure (top) and band structure (bottom) of selected 2D layered materials of interest. **(A)** MoS_2. **(B)** Phosphorene (black phosphorous). **(C)** Graphene. *Figures (A-C) reprinted with permission from ref [140]. Springer Nature COPYRIGHT (2014).*

An attractive option is to combine QDs with layered 2D materials in hybrid devices that allow

one to harness many of the desirable features of QDs, including strong, size tunable absorption,

long exciton lifetimes and advanced phenomena such as carrier multiplication, while exploiting

the excellent charge transport properties of 2D materials. Accordingly, in a typical hybrid QD-2D

photodetector, the QD layer acts as the light-absorbing, charge-generating layer, while the 2D layer

acts as the transport layer [190], with charge transfer between the layers being a key process for optimization. Such charge transfer affected by various parameters such as ligand length (*i.e.* QD-2D spacing) and relative band alignement [191], in a similar manner to the role these factors play in charge transfer within QD-only films as discussed above. In this section, we will briefly review types of photodetectors and their figures of merit and then discuss recent advancements in hybrid QD-layered 2D photodetectors, with emphasis on graphene-QD hybrid and TMD-QD hybrid devices.

4.2 Types of Photodetectors

A. *Photoconductors*

A photoconductor is a two-contact optoelectronic device in which two ohmic source and drain electrodes are seperated by a photoactive layer [*i.e.* a QD film; **Figure 4.3 (A)**]. Operated under an applied bias, photoconductors detect temporary changes in the carrier mobility, density, or both under incident illumination due to photogeneration of carriers in the photoactive layer [192]. Under a moderate field, the majority carriers (which can be either holes or electrons, depending on the material) have a higher mobility than the minority carriers. This results in the majority carriers having a shorter transit time to traverse the photoactive area to an electrode, while minority carriers remain left behind. If holes, for example, are the majority carrier, as they are swept out of the detector, charge neutrality is maintained by additional holes supplied from the other electrode. Therefore, effectively, holes can circulate the detector many times during the carrier lifetime, resulting in gain (a measure of how much the response departs from linear dependence) [83,193]. Higher gain leads to detectors with high responsivities, but also higher noise levels which hinders high sensitivity applications [87]. Taking advantage of differential carrier mobility also means photoconductors typically have slower response times than a photodiode, due to the temporal

response also being determined by the lifetime of the trapped carriers. Photoconductors are more common for IR applications such as thermal imaging [194] and motion detection [195].

B. Phototransistors

Phototransistors are essentially photoconductors bridged by a "gate" electrode, typically a metal or degenerately doped semiconductor separated by a dielectric spacer layer. The gate electrode provides the ability to modulate transport using an applied gate voltage; a schematic of a simple phototransistor can be seen in **Figure 4.3 (B)**. Phototransistors function in a similar manner as field-effect-transistors (FETs) and are even referred to as optical FETs (OFETs) on occasion [37]. Applying a gate bias introduces charges into the conductive channel, which can be used to tune transport by, *e.g.* filling trap states [37], as in the case for devices based on *p*-type lead chalcogenide QD films, for which introduction of holes by a negative applied bias increases the conductivity. Phototransitors have become a preferred architecture of the hybrid QD-2D detectors because the level of control offered by the ability to modulate carrier dynamics and concentrations within the device allows for more versatility than a typical photoconductor.

C. Photodiodes

Photodiodes employ an internal electric field established within the absorbing layer of the device to enhance the efficiency with which photogenerated carriers are separated and subsequently collected. The internal electric field is created by the pairing of materials with majority carriers of opposite charge, which interdiffuse and undergo recombination near the junction to create a depletion region featuring a charge gradient and built-in field. The field favors very fast, unidirectional transport by drift for photogenerated electrons and holes (in opposite directions, respectively), largely preventing recombination. In contrast carriers generated outside the depletion region travel by much slower diffusion to reach either an electrode or the depletion

98

region [193], allowing more time for recombination; accordingly, the size of the depletion region is an important factor in performance. An example of a *p-n* junction photodiode device structure is presented in **Figure 4.3 (C).** Photodiodes are typically operated under moderate reverse bias to create an even wider depletion region to minimize transit time as much as possible, but not too wide or transit-time effects will limit the response frequency [193]. Photodiodes are often categorized by the types of materials forming the junction (*e.g.* Schottky junction, *p–n* junction, *p-i-n* junction), but the principles of separating and collecting photogenerated charges using a built-in electric field are similar [83], and the relation between device thickness and carrier diffusion length (as determined by carrier lifetime and mobility) is critical to performance. For reference, among QD-based devices, PbE QD solids have exhibited record-high diffusion lengths of up to 230 nm [62]. Photodiodes have a gain of 1 unless operated in avalanche mode, under large reverse biases, where impact ionization and carrier multiplication can result in gains higher than 1. Photodiodes can also be operated under a zero-bias condition; however under reverse bias condition the device can have greater bandwidth and wider linear dynamic range. Applications requiring fast response times are heavily reliant on photodiodes [193], as current commercially available photodiodes can have response times as fast as 35 ps.
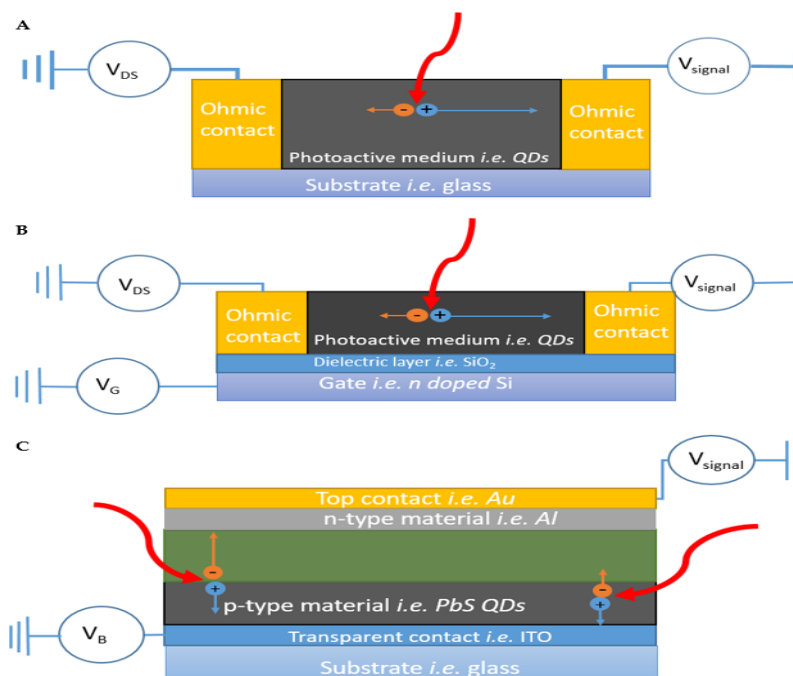
Figure 4.3. (A) Schematic of a photoconductor device. Incident photons [thick red curved arrows] cause electron-hole pairs to form within the photoactive region [black]. A constant applied voltage [V_{DS}] causes electrons [orange circles] and holes [blue circles] to traverse the photoactive region towards their respective electrodes at different speeds, indicated by the different lengths of orange and blue arrows (in this example holes are traveling faster). As hole are collected at the drain electrode, new holes are injected at the source electrode to maintain charge neutrality; as holes circulate through the device gain is achieved. **(B)** Schematic of a phototransistor device. Operation is similar to a photoconductor, but the device is fabricated on a substrate that allows for the possibility of applying a gate voltage [V_G] to tune transport in the photoactive area. **(C)** Schematic of a photodiode device. A *p-n* junction enhances charge transport by creating an internal electric field. The green shaded region indicates the depletion region, which can be tuned by altering the bias voltage [V_B]. Carriers generated in the depletion region are quickly separate and are collected, while carriers generated outside of the depletion region must avoid recombination while they diffuse to either depletion region or contact. All devices are displayed as having a current readout; this signal is typically converted into voltage by a load resistor for easy readout using an oscilloscope.

4.3 Figures of Merit

Figures of merit [192,193,196] that account for device variables, such as device active area, response time, and spectral region are key for evaluating and comparing detector performance. The first measure of how effective a photodetector can be is how efficiently incident photons are converted into electron-hole pairs and subsequently collected as photocurrent. The external quantum efficiency (*EQE*) is a measure of how well the device absorbs and converts incident photons into photocurrent, while the internal quantum efficiency (*IQE*) is a measure of how efficiently absorbed photons are converted into photocurrent. The incident photon flux (ϕ_{in}) can be calculated by dividing the incident power by the energy of the incident photon. Similarly, the absorbed photon flux (ϕ_{abs}) can be calculated by multiplying the ϕ_{in} by the fraction of light that is absorbed [197].

$$EQE(\lambda) = \frac{\left(\frac{I_{ph}(\lambda)}{q}\right)}{\phi_{in}(\lambda)} \qquad\qquad Equation\ 4.1$$

$$IQE(\lambda) = \frac{\left(\frac{I_{ph}(\lambda)}{q}\right)}{\phi_{abs}(\lambda)} \qquad\qquad Equation\ 4.2$$

In the preceding equations, q is the elementary charge and I_{ph} is the photocurrent, which can be calculated by $I_{ph} = I_{illum}-I_{dark}$, where I_{illum} is the photocurrent under illumination and I_{dark} is the dark photocurrent. The fraction of light absorbed by a QD layer can be calculated with the Beer-Lambert law; for many films this equation can be written in terms of optical thickness *(τ)*, which can be expressed as $\tau = L\sum_{i=1}^{N} \sigma_i n_i$, where σ_i and n_i are the attenuation coefficients and number densities of each attenuating species in the absorbing medium. The absorbance can then be calculated with the relationship *A = τ/ln10.* Ellipsometry can also be used to determine refraction indexes and

extinction coefficients of materials, which can then be used to create a model for photon absorption [114,198].

The responsivity *[R (λ)]* of a detector is a measure of the electrical signal output relative to the optical signal input, similar to the *EQE*. The units of *R(λ)* are A/W and it can be calculated by the following equation [192]:

$$R(\lambda) = \frac{EQE(\lambda)q\lambda}{hc} \frac{1}{\sqrt{1 + \omega^2\tau^2}} G(\lambda) \qquad \text{Equation 4.3}$$

where λ is the wavelength of the incident photons, *h* is Planck's constant, *c* is the speed of light, ω is the modulation frequency, τ is the time constant, and *G (λ)* is the photoconductive gain. Photodiodes have a gain of 1 unless they are operated in avalanche mode, while for photoconductors and phototransistors the gain is equal to the majority carrier lifetime divided by the transit time *[G (λ) =$\tau_{lifetime}$ /$\tau_{transit}$]*. Transit time can be calculated from the carrier mobility and bias voltage by $\tau_{transit} = L^2 / (\mu V_{bias})$ [197].

Noise equivalent power [*NEP(λ)*] is a measure of the detector sensitivity, defined as the optical power at which the signal-to-noise ratio (SNR) is 1, giving the minimum power the detector can effectively detect per square root of bandwidth [192], and is obtained using:

$$NEP(\lambda) = \frac{\sqrt{\overline{I_n^2}}}{R(\lambda)} \qquad \text{Equation 4.4}$$

where I_n is the total noise current, and *NEP (λ)* is in units of W/Hz$^{1/2}$. Total noise current is the sum of all the noise sources, which includes low-frequency flicker noise (*1/f*), thermal noise (*I_{th}*) and shot noise (*I_{sh}*). The root-mean-square value of thermal noise and shot noise current is given by $I_{th} = \sqrt{4kTB/r}$ and $I_{sh} = \sqrt{2qBI_{dark}}$, respectively, where *k* is Boltzmann's constant, *T* is absolute temperature, *r* is the resistive element source contributing to noise, *B* is the noise bandwidth, and *I_{dark}* is the dark current [101].

The most useful figure of merit is the detectivity [$D^*(\lambda)$], which accounts for different configurations and detector areas [101], allowing for comparison across all devices. The $D^*(\lambda)$ of a photodetector is expressed in units of Jones (cm Hz$^{1/2}$/W), and is obtained using the following equation:

$$D^*(\lambda) = \frac{\sqrt{A}}{NEP(\lambda)} \qquad\qquad Equation\ 4.5$$

where A is the detector active area (cm^2). $D^*(\lambda)$ is proportional to $R(\lambda)$, and it is also an indirect function of applied bias, temperature, modulation frequency, and wavelength [101,192]. When reporting $D^*(\lambda)$ the value should be accompanied by the measurement conditions to ensure that presented values are both correct and can be properly used for comparison of multiple devices.

The linear dynamic range [DR (λ)] shows the range over which the photocurrent increases linearly with increasing incident optical power and provides for the range of optical power over which detector should be utilized. Ideally, R (λ) should remain constant with the increase of optical intensity. DR (λ) has units of decibels (dB) and is expressed as:

$$DR(\lambda) = 20log\frac{P(\lambda)_{max}}{NEP(\lambda)} \qquad\qquad Equation\ 4.6$$

where $P(\lambda)_{max}$ is the incident optical power when the photocurrent saturates [192].

4.4 Graphene QD Hybrid Detectors

As described above, graphene has been an attractive material for photodetection applications since its discovery, due to high carrier mobilities and potential broad spectrum applicability [197], and QDs are of interest because of strong, tunable light absorbance. Sensitizing graphene-based photodetectors with PbE QDs can improve D^* of a device by improving absorption in the short-wave IR and visible regions. Photon absorption in a layer of QDs creates electric charges that can then be transferred to the graphene for fast transport. In the case of phototransistors and

103

photoconductors, the high carrier mobility combined with the long carrier lifetimes in the QD layer would potentially allow the carriers to circulate the device many times before recombining, leading to high gains.

In 2012 Konstantatos et al. [190] reported a hybrid graphene/PbS QD phototransistor with ultrahigh gain, sparking much interest in the system and inspiring many variations to be fabricated in the following years. In the seminal device, single and bilayer graphene flakes were prepared by mechanical exfoliation and deposited on Si/SiO$_2$ substrates, followed by gold contact deposition and, finally, PbS QD deposition via spin-coating. Ligand exchange from oleic acid to EDT was performed during the QD deposition phase through a layer-by-layer approach, with a resulting film thickness of ≈80 nm. A schematic of the device can be seen in **Figure 4.4 (A)**. The photo-generated holes in the PbS QD layer are transferred to the graphene layer while the photo-generated electrons remain trapped in the PbS QD layer. Due to the high hole mobility in graphene, these carriers are allowed to circulate in the device, while charge conservation in the graphene channel is enabled by hole replenishment from the source electrode for every hole collected at the drain, resulting in a gain of 10^8 electrons per photon. The vast improvement of the gain led to an *R* on the order of 10^7 A/W and a *D** of 7×10^{13} Jones. A short gate voltage pulse can be used to purge the charge carriers from the QD layer as shown in **Figure 4.4 (D)**, effectively resetting the device and increasing the operating speed, which is advantageous for imaging applications.

Later in the same year, Sun et al. [199] used chemical vapor deposition (CVD) rather than mechanical exfoliation to prepare the graphene transport layer. CVD allows for precise control over thickness, as well as the possibility of fabricating larger area devices than what is feasible with mechanically exfoliated graphene. Upon deposition of PbS QDs capped with pyridine ligands onto un-doped graphene, the measured Dirac point shifts from 0 V to 50 V, indicating *p*-type

doping of the graphene layer, as can be seen in **Figure 4.4 (B)**. Along with this shift in the Dirac point, there is a sizable decrease in electron mobility from 1000 cm^2/VS to 440 cm^2/Vs while the hole mobility remained unchanged at 1000 cm^2/Vs. Responsivity of the detector was found to be affected by the thickness of the QD layer, with a saturation point occurring at ≈150 nm, as can be seen in **Figure 4.4 (C)**. The devices using CVD grown graphene showed R values of 1×10^7 A/W, similar to that of detectors using mechanically exfoliated graphene.

Ligand length has a significant effect on the efficiency of charge transfer from QDs to graphene [200], as can be seen in **Figure 4.4 (E)** by the more apparent shift in the Dirac point of the graphene/QD system when a shorter capping ligand is utilized, indicating increased coupling between graphene and QDs. **Figure 4.4 (F)** shows the responsivity of the QD/graphene system can reach values on the order of 1×10^9 A/W with shorter capping ligands such as thioglycerol (TGL) (length 0.5 nm). Ideally, photocurrent as a function of incident photon energy of devices should closely follow the absorption features of the QDs used, as seen in **Figure 4.4 (G),** indicating increased sensitivity in the range where QDs are strongly absorbing. Laser shock imprinting has also been used as a method to improve contact between graphene and QDs in graphene/PbS QD/graphene sandwich structure [201], resulting in improved response time and current on/off ratio.
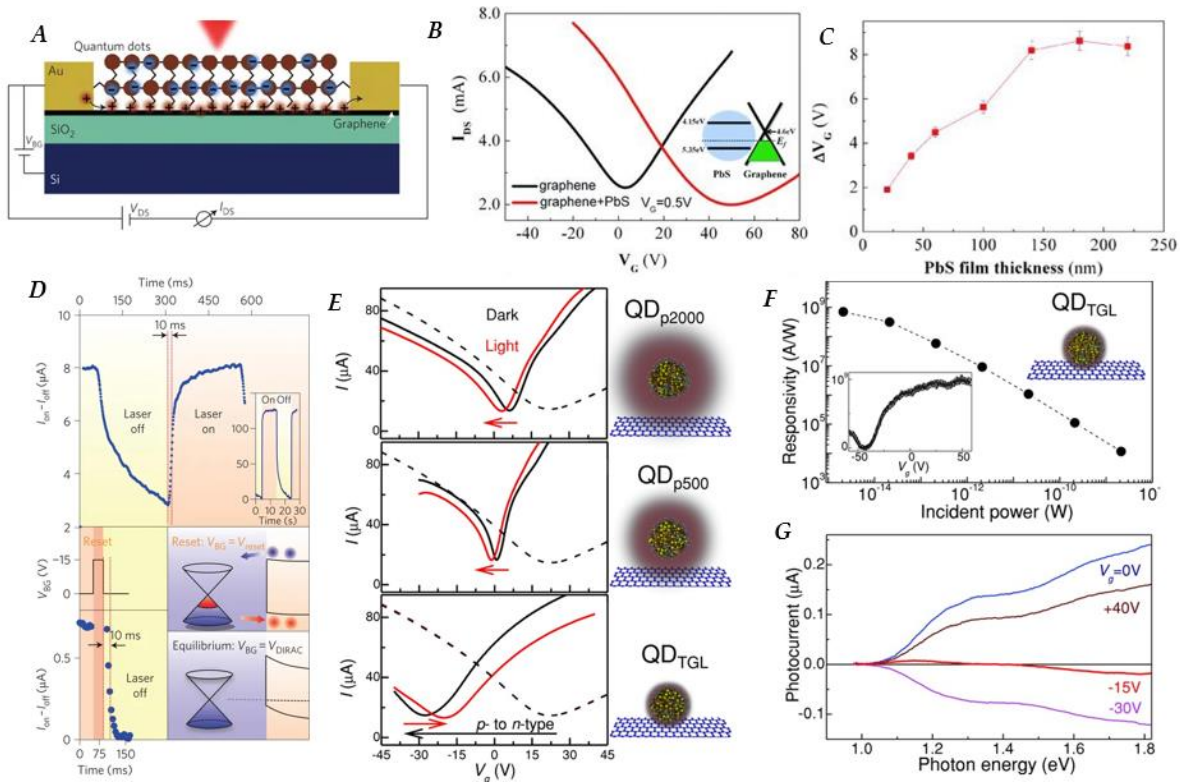
Figure 4.4 (A) Schematic representation of a typical graphene-QD hybrid phototransistor, in which graphene acts as gate modulated transport layer for holes; **(B)** Transfer characteristics ($I_{DS} \sim V_G$, V_{DS} = 0.5 V) of bare un-doped graphene transistors before (black) and after the deposition of PbS QDs on the graphene film (red). *P-type* doping in the graphene film is indicated by the transfer curve becoming asymmetric and the Dirac point shifting to a positive gate voltage ($\sim$ 50 V) after deposition. Inset: Energy diagram of the heterojunction of PbS QD and graphene (valence and conduction band values of the PbS QD are 5.35 eV and 4.15 eV respectively, while the value for graphene reads 4.6 eV)**. (C)** Horizontal shift of the transfer curves ($I_{DS} \sim V_G$, V_{DS} = 0.5 V) of the hybrid graphene-PbS QDs devices with different thicknesses of PbS QDs layers under irradiation with 6.4 mW cm^{-2} of 895 nm light. Saturation after 150 nm indicates that any carriers generated further than 150 nm from graphene layer are not collected; **(D)** [Top] Photocurrent response as a function of time of a hybrid graphene-PbS QDs phototransistor. The temporal response indicates a rise time of ~10 ms, and two different fall times on the order of 100 ms (50%) and 1s (see inset, measured at a higher power of 267 pW). [Bottom] temporal response of a bilayer graphene phototransistor after the laser is turned off and application of

106

a reset pulse for 10 ms. The fall time is reduced from several seconds to ~10ms (insets: energy diagrams showing effect of reset pulse lowering potential barrier allowing electrons trapped at graphene-QD barrier to escape); **(E)** Transfer characteristics (I_{DS}-V_G, V_{DS} = 0.1V) of *p*-doped graphene phototransistors before (dashed lines) and after (black) deposition of PbS QD with varying ligand length (schematic not to scale) red line is transfer curve under illumination with unfocused laser light (λ = 514 nm) with P = 10 W m^{-2}. Size of shift after deposition is an indication of coupling between graphene and QD layer; shift upon illumination is an indication of charge transfer of photoexcited carriers. **(F)** Responsivity as a function of incident power for hybrid detector using short TGL ligands (inset: responsivity as a function of V_G) (G) Photocurrent dependence on photon energy of the incident light (P $\approx$ 10^{-11} W) at different gate voltages for same device as Figure F. *Figures reprinted by permission from: (A and D) Ref. [190]. Springer Nature COPYRIGHT (2012); (B and C) Ref. [199].* John Wiley and Sons COPYRIGHT (2012), (E, F, and G) *Ref. [200]. John Wiley and Sons COPYRIGHT (2015).*

Multi-heterojunction phototransistors synthesized by spin-coating alternating graphene and PbSe QD layers show the importance of using graphene as the bottom layer of the device [202], with graphene bottom layer device displaying electron and hole mobilities of μ_E = 147 cm^2/Vs and μ_H = 137 cm^2/Vs, while QD bottom layer devices showed μ_E = 14 cm^2/Vs and μ_H = 59 cm^2/Vs. Intercalation of graphene layers within a PbS QD film also improves the charge carrier extraction of the device by counteracting the limitation of diffusion length in QD films. Placing graphene layers, separated by a distance less than the carrier diffusion length of the QD film, periodically through a QD/graphene film results in higher photocurrents than devices with only a bottom graphene layer [203].

Electrohydrodynamic nanoprinting of colloidal PbS QDs onto graphene FETs with varying quantum dot layer thicknesses is a potential method for realizing small footprint detectors with

high spatial resolution [204]. The responsivity of the photodetectors increases with increasing layer thicknesses up to 130 nm. However, the noise current is found to be independent of the layer thickness. Additionally, responsivity and noise current are both linearly dependent on the applied drain voltage and drain current. As a result, the specific detectivity is independent of the drain voltage, and the detector can be operated at lower drain voltage thus reducing power consumption. $D*$ values of at least 10^9 Jones are reported without degradation of the charge carrier mobilities in graphene from the electrohydrodynamic printing of QDs [204].

Response time of phototransistors with thicker QD films (>100 nm) is still regulated by the diffusion of carriers through the QD sensitizing layer. However, this can be overcome by a device architecture that combines a graphene–colloidal QD photodiode and a high-gain phototransistor; a schematic of the devices can be seen in **Figure 4.5 (A)**. Transforming the electrically passive sensitizing layer to an active one through an applied electric field in the photodiode significantly enhances charge collection, due to carrier drift instead of solely relying on diffusion [205]. The QD photodiode consists of a top-contact (*e.g.* ITO) acting as the cathode of the QD photodiode, whereas graphene acts as the hole acceptor contact and the charge transport channel for the phototransistor. Progressively increasing the bias voltage causes the depletion region to grow, enhancing efficiency of the charge collection [**Figure 4.5 (D)**]. The hybrid device architecture results in a sub-millisecond temporal response, a gain-bandwidth product on the order of 10^8, a linear dynamic range in excess of 110 dB, and very high sensitivity with experimentally measured $D*$ of 1×10^{13} Jones.

In addition to the properties described above, graphene's weak electrostatic screening effect, finite density of states and mechanical flexibility [206] makes it a versatile material for conducting electrodes. Due to its relative transparency at wavelengths greater than 1000 nm,

compared to ITO [207], there has been a push for using graphene as the transparent conducting electrode in IR detection and imaging applications. Responsivity of graphene-based and ITO-based PbS QD photodiodes from wavelengths of 1100-1800 nm operated at different reverse bias conditions are shown in **Figure 4.5 (C).** The responsivity of graphene-based vs. ITO-based PbS photodiodes are 0.112 and 0.076 A/W at 1530 nm, respectively, and increase to 0.69 and 0.50 A/W at bias of -1 V. Photocurrent response of the devices under IR illumination (1530 nm) was found to increase linearly with light power. Ambipolar vertical phototransistors [**Figure 4.5 (B)**] [208] utilizing graphene as an electrode have been fabricated using both PbS [209] and PbSe [206] QDs. In a vertical phototransistor, the channel length is determined by the film thickness, which is much shorter than a typical lateral phototransistor channel, leading to faster response times. Vertical phototransistors utilizing graphene as source electrode with PbS QDs displayed temporal response times of 14 ms, which improves to 8 ms when graphene is mixed within the QD layer, as seen in **Figure 4.5 (E and F)**, while PbSe QD detectors showed a response time of 7 ms.

Figure 4.5. (A) Schematic representation of a combined QD photodiode and graphene phototransistor device; V_{TD} creates a bias in the photodiode. **(B)** Schematic of a typical hybrid graphene-QD vertical phototransistor using graphene as an electrode. **(C)** Comparison of responsivity as a function of wavelength at various applied biases for devices using graphene and ITO as an electrode, respectively. **(D)** Energy band diagram of graphene QD interface; yellow shading indicates the depletion region in the QD layer. Top schematic is when detector is operated in only phototransistor mode, while the bottom shows the expansion of the depletion region when QD layer is used as a photodiode with an applied bias. **(E)** Photocurrent response of hybrid graphene-PbS QD phototransistor as a function of time for light on/off cycles at an irradiance of 335 mW/cm2, (V_{DS} = 1 V and V_{GS} = 1.5 V). **(F)** Zoomed in view of E to see rise and decay times of device, rise time 8ms, decay time 125 ms. *Figures reprinted with permission from; (A and D) Ref. [205]. Springer Nature COPYRIGHT (2016), (B) Ref. [208]. AIP Publishing COPYRIGHT (2016), (C) Ref. [207]. AIP Publishing COPYRIGHT (2011), (E and F) Ref. [209]. Copyright (2017) American Chemical Society.*

4.5 Merging QDs with TMDs and Other Layer 2D Materials

While graphene-QD hybrid detectors display high gain, they suffer from high dark currents due to the semi-metallic nature of graphene. Transition metal dichalcogenides (TMDs) have relatively large bandgaps (1-2.5 eV) [140], which make them interesting candidates for applications that require high sensitivity. Using 2D TMDs rather than graphene presents a trade-off in carrier mobility and ultimately gains in exchange for lower dark conductivities. In 2015 Kufer et al. [210] published the first hybrid MoS_2-PbS QD photodetector, in which micromechanically exfoliated MoS_2 nanosheets were used as electrically controllable transport layers, resulting in responsivities on the order of 6×10^5 A/W. $D*$ of bilayer and few-layer devices were found to be 2×10^{11} and 5×10^{11} Jones, respectively. At high negative back-gate bias the MoS_2 channel is depleted from free carriers in the dark state, giving the detector the potential to reach high sensitivity in the shot noise limit with $D*_{shot-noise\ limit}$ reaching up to 7×10^{14} Jones at V_G of -100 V, **Figure 4.6 (A)**. Application of a semiconducting TiO_2 buffer layer at the interface of MoS_2 and PbS QDs, as presented in **Figure 4.6 (B),** preserves the gate modulation by suppressing the high density of localized sub-band-gap states that pin the Fermi level [211]. The maintained gate control over carrier density in the conduction channel allows for low noise operation similar to pristine MoS_2 devices, resulting in a $D*$ of 5×10^{12} Jones, an improvement of more than 1 order of magnitude compared to MoS_2/PbS devices without a buffer layer [211]. **Figure 4.6 (C)** shows the responsivity as a function of irradiance as well as the decay time of MoS_2/PbS devices when a TiO_2 buffer layer is utilized.

Applying methods that were previously used in QD-only devices to provide a built-in *p-n* junction via energy level modification through ligand engineering can also have positive impacts on hybrid devices. The combination of tetrabutylammonium iodide (TBAI) and EDT is a well-known ligand combination used to create such a built-in potential in QD photovoltaics, resulting

in more efficient charge carrier separation in the QD layer. Combining a layer of EDT-treated PbS QD with a layer of TBAI-treated PbS QD along with and MoS_2 transport layer in a vertical phototransistor, as shown in **Figure 4.6 (D)**, resulted in fast response times (960 µs), and $D*$ on the order of 10^{11} Jones under applied gate voltage of -40 V [212].

The range of TMD materials used in hybrid PbE QD photodetectors has also been expanded to include WS_2 [213] and WSe_2 [214] which show higher carrier mobilities than MoS_2. Phototransistors fabricated using CVD to fabricate a *p*-type WSe_2 monolayer on Si/SiO_2 substrate, coated with PbS QDs with TBAI ligands, displayed rise times of 7 ms and a decay time of 480 ms. The responsivity of hybrid WSe_2-PbS device could be tuned by the applied gate voltage, but operating in depletion mode was not necessary, which overcomes a drawback for the MoS_2-QD hybrid device. The highest $D*$ of the device was found to be 7×10^{13} Jones, with a responsivity of up to 2×10^5 A/W, as seen in **Figure 4.6 (E)**. WS_2/EDT-capped PbS QD devices were fabricated in a similar manner resulting in rise and decay times of 153 µs and 226 µs, respectively; however, the responsivity (14 A/W), and $D*$ (3.9×10^8 Jones) of the devices were lower than the WSe_2 counterpart. Detectors utilizing both WS_2 and MoS_2 combined with larger (8.0 ± 1.7 nm diameter) PbS QDs, with an absorption peak near 1.8 µm show compelling results with responsivities of 1400 A/W, at 1.8 µm excitation operated at 1 V bias, and $D*$ as high as 10^{12} Jones at room temperature for the WS_2 based devices [215]. The devices employing larger dots showed better results using Zn_2I and mercaptopropionic acid (MPA) ligands, rather than the traditional EDT

ligand, as this ligand combination has been shown to produce higher mobilities in larger PbS QD films [216].

Figure 4.6. (A) Photocurrent response of hybrid MoS$_2$-PbS QD phototransistor as a function of time at various, relatively high gate voltages (V$_{DS}$ = 1 V, irradiance 3 µW/cm^2). **(B)** Schematics of bare MoS$_2$ phototransistor as well PbS QD/MoS$_2$ phototransistor with and without TiO$_2$ buffer layer; label colors correspond with points on the graph. Graph is On/Off ratio as a function of dark current density, demonstrating that a TiO$_2$ buffer layer helps to reduce dark current. **(C)** [Right] Responsivity as a function of irradiance for hybrid MoS$_2$-PbS QD device with a TiO$_2$ buffer layer at different gate voltages (V$_{DS}$ = 1 V). [Left] Photocurrent decay time of a light response at 67 nW/cm^2; the approximation with a single-exponential function results in a time constant of 12 ms. **(D)** Schematic of hybrid MoS$_2$-PbS QD devices using EDT and TBAI ligands to create a built in potential (energy-band diagram inset), and [right] response time of device under laser 850 nm laser illumination (P= 200 nW, V$_{DS}$= 1 V, V$_G$= 0 V). **(E)** Responsivity as a function of power density of PbS QD and hybrid WSe$_2$-PbS QD phototransistors under 970 nm illumination (V$_{DS}$ = 1 V, V$_G$ = 0 V). *Figures reprinted by permission from; (A) ref [210]. John Wiley and Sons COPYRIGHT (2015), (B and C) Ref. [211]. COPYRIGHT (2016) American Chemical Society, (D) Ref. [212]. COPYRIGHT (2018) American Chemical Society, (E) Ref. [214]. John Wiley and Sons COPYRIGHT (2017).*

Other layered 2D materials have also been used in hybrid 2D-PbE QD photodetectors. Tin disulfide (SnS2)/PbS QD hybrid photodetectors show distinct photoresponse towards photons of different wavelengths [217]. Mechanically exfoliated SnS2 nanosheets (5 layers) sensitized with EDT-capped PbS QDs and gold electrodes, yielded a broadband, spectrally distinctive photodetector which displays positive photocurrent at wavelengths below 520 nm (the cutoff absorption wavelength of SnS2) and negative photocurrent at wavelengths above 520 nm, as shown in **Figure 4.7 (A, B).** This spectral selectivity is accounted for by illumination-modulated barrier height between the gold electrode and the SnS2 nanosheet. Upon NIR illumination, only PbS QDs are absorbing incident photons, and photogenerated electrons flow into SnS2 nanosheets, reversing the *p*-type doping effect in the dark and shifting the Fermi level of SnS2 nanosheets upwards. Consequently, the contact between SnS2 nanosheets and Au electrodes is Schottky in nature, accounting for the observed negative photoconductivity. Under UV illumination, SnS2 nanosheets absorb incident photons, resulting in carrier density increasing in the SnS2 channel, which overrides the contribution from photogenerated carriers in the PbS QDs, leading to the observed positive photoconductivity [217].
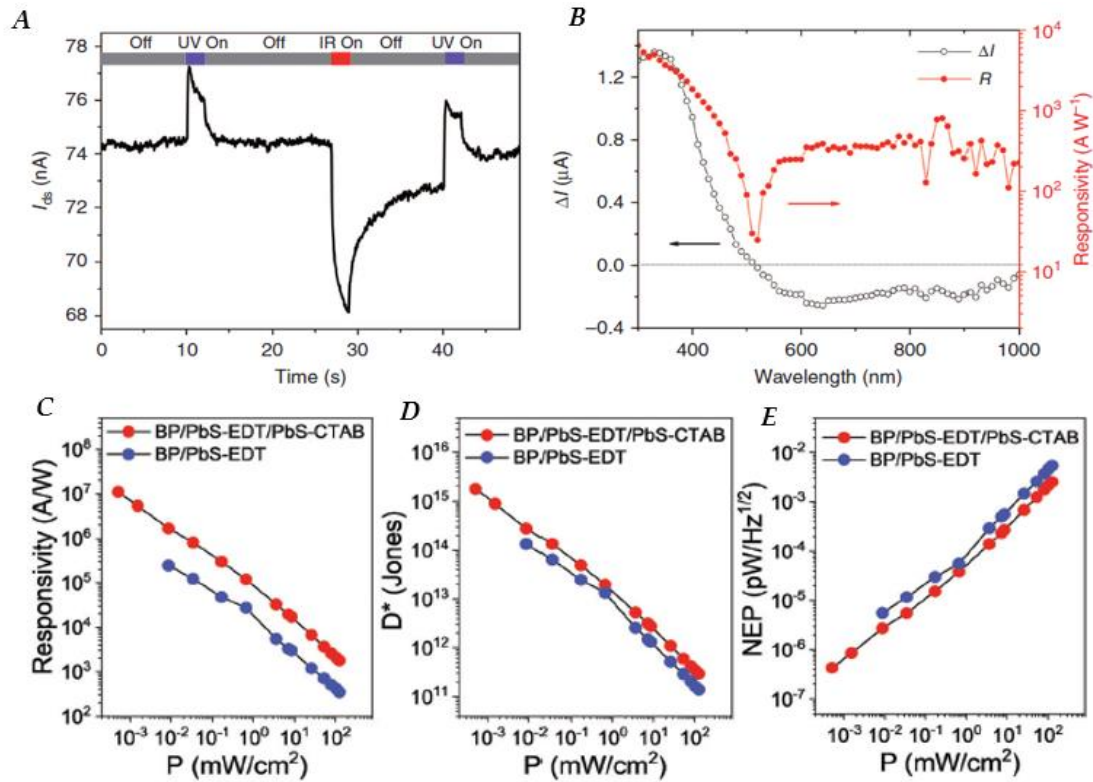
Figure 4.7. (A) Photocurrent as a function of time under illumination with 365 nm and 970 nm LED light sources, showing the spectrally distinctive characteristics of the SnS2/PbS QD photodetector. **(B)** Wavelength-dependent photocurrent and responsivity of a SnS2/PbS QD device; the light source is a xenon lamp modulated with an optical grating to generate monochromatic light with a step-size of 10 nm (V_G = 0 V, V_{DS} = 1V). **(C)** Responsivity, **(D)** Detectivity and **(E)** NEP of hybrid BP/PbS QD devices with EDT only and EDT/CTAB ligand combinations as a function of power intensity at 633 nm wavelength at V_{DS} = 1 V and V_G = 0 V. Figures reprinted with permission from; (A and B) Ref. [217]. Springer Nature COPYRIGHT (2016), (C, D, and E) Ref. [218]. Royal Chemical Society Copyright (2019).

2D black phosphorous (BP) nanosheets, also called "phosphorene", have also recently emerged as a potential candidate for photodetection devices due to high carrier mobilities and anisotropy. Phosphorene has typically suffered from formation of phosphoric acid on the surface under ambient conditions, which causes device performance to degrade. However recent work has

shown that treatment with EDT recovers the desirable properties of the device even after degradation [219]. Since EDT is also a common ligand treatment for QD devices as well, Lee *et al.* decided to combine phosphorene and PbS QDs into a hybrid photodetector, resulting in responsivities of 5.36×10^8 A/W and a *D** of 1.89×10^{16} Jones [220]. A hybrid BP/PbS QD photodetector with a cascade-type energy band structure can be fabricated by using ligand chemistry to alter the energy bands of two different layers of PbS QDs. EDT and cetyltrimethylammonium bromide (CTAB) ligands are utilized to form an additional energy barrier at the interface of bilayer QDs. A high responsivity of 1.1×10^7 A/W, a *D** of 1.75×10^{15} Jones and a low noise equivalent power of 4.3×10^7 pW/Hz$^{1/2}$ are achieved at a bias of 1 V without gate voltage modulation, as shown in **Figure 4.7 (C,D,E),** respectively. The responsivity is an order of magnitude higher compared to the phosphorene/PbS photodetector that used only EDT ligands [218]. PbSe QDs have also been integrated with 2D Bi_2O_2Se, a 2D material with a relatively narrow bandgap around 0.8 eV, in devices showing impressive responsivities on the order of 10^3 A/W, when excited with 2000 nm excitation and operated under 100 V bias [221]. Table 1 lists the devices discussed within this review along with their figures of merit.

Table 4.1: Hybrid PbE QD-layered 2D photodetectors and their corresponding Figures of merit. All detectors presented in this table are phototransistors, with one detector that from Ref. [138] utilizing a hybrid phototransistor/photodiode geometry. Ligand abbreviations correspond to: EDT = ethanedithiol, TBAI = tetrabutylammonium iodide, TGL = thioglycerol, DTG = 2,3-dimercapto-1-propanol, MPA = mercaptopropionic acid, and CTAB = cetyltrimethylammonium bromide.

QD/ Material	Ligand(s)	Excitation wavelength (nm)	Response (rise) time (ms)	Responsivity (A/W)	Detectivity (Jones)	Reference
PbSe/Graphene	EDT	808	12000	10^6	N/A	[202]
PbS/Graphene	TBAI	532	3000 (decay)	5.9×10^7	N/A	[203]
PbS/Graphene	EDT	1200	100	8×10^3	10^9	[204]
PbS/ Graphene	Pyridine	895	130	10^7	N/A	[199]
PbS/Graphene	EDT	532	10	10^7	7×10^{13}	[190]
PbS/ Graphene	TGL/DTG	532	N/A	10^9	N/A	[200]
PbS/Graphene	EDT	635	1	2×10^6	10^{13}	[205]
PbS/MoS$_2$	EDT	635	350 (decay)	6×10^5	5×10^{11}	[210]
PbS/MoS$_2$	TBAI/EDT	850	0.95	5.4×10^4	1×10^{11}	[212]
PbS/WS$_2$	EDT	808	0.153	14	3.9×10^8	[213]
PbS/MoS$_2$/TiO$_2$	EDT	635	12	10^5	5×10^{12}	[211]
PbS/WSe$_2$	TBAI	970	7	2×10^5	7×10^{13}	[214]
PbS/WS$_2$	Zn$_2$I/MPA	1800	200	1442	10^{12}	[215]
PbS/MoS$_2$	Zn$_2$I/MPA	1800	32	202	2.8×10^{11}	[215]
PbS/SnS$_2$	EDT	970	160 (decay)	1×10^6	2.2×10^{12}	[217]
PbS/BP	EDT	405	770 (decay)	5.36×10^8	1.89×10^{16}	[220]
PbS/BP	EDT/CTAB	633	N/A	1.1×10^7	1.75×10^{15}	[218]
PbSe/Bi$_2$O$_2$Se	EDT	2000	4	10^3	N/A	[221]

4.6 Outlook

Hybrid PbE QD-layered 2D photodetectors display great promise for improving detector capabilities, especially in the spectral regions beyond the 1 µm bandgap of Si-based detectors, with

much progress made in recent years. However, there are still many avenues for continued progress in improving the Figures of merit. There exists a wide and expanding array of studies of PbE QDs aimed at: controlling synthesis to improve size distribution and stability [22,85,222,223]; QD size and composition effects on the optoelectronic properties [120,128,224]; in-solution and layer-by-layer ligand exchange techniques [32,56]; and inter- and intra-layer charge transfer in QD films with other materials [50,55,225]. Many of these findings have yet to be applied to hybrid QD/2D material hybrid devices. Particularly promising directions would involve application of less-commonly used ligand/surface treatments [32,56], expanding the spectral range further into the IR by increasing QD size [23,215], and use of ALD to improve mobility [63,64]. Research and development of new layered 2D materials and techniques for improvement in synthesis of current materials is also an ongoing direction. Strides made in recent years show the great potential of PbE QD-layered 2D hybrid photodetectors on account of facile operation at room temperature, low cost, flexible substrate compatibility, and high Figures of merit. Continued progress in the field is possible through continued research, implementation of new materials, surface treatments, and device engineering.

Chapter 5: Summary and Future Research

In this dissertation PbSe/CdSe QDs synthesized via low temperature (> 130°C) cation exchange were used a seed for further shell growth of CdSe and CdS shells via modified SILAR methods. Position of visible emission peak was shown to be tunable via CdSe shell thickness, while addition of CdS shell was shown to improve PLQY from the CdSe shell. NIR PL lifetimes were significantly increased by the addition of a CdS shell, as a result of increased delocalization of the electron wavefunction into the CdS shell. Increase in NIR exciton lifetime is of significant consequence for solar applications allowing for greater possibility of carrier extraction. PbSe/CdSe/CdS QDs were also shown to exhibit Auger assisted up-conversion, via a two-pulse excitation experiment utilizing a continuous wave laser setup, in which up-converted emission intensity was found to be independent of duration between pulses at long pulse delays.

Simple PbSe devices were fabricated using an in-solution ligand exchange method. Carrier mobility and carrier density are able to be altered based on choice of capping ligand. Modulation of carrier density in PbSe QD films has only previously been shown via post deposition treatment of the QD film, therefore the ability to modulate carrier density by a factor of 5 through choice of capping ligand is significant. Fabrication of simple radiation detectors was also done, showing appreciable response to incident alpha radiation. The magnitude of current output upon exposure to alpha radiation was shown to be dependent on the strength of the source radiation and the applied bias. Minor response to gamma radiation was also observed.

A critical review of layered 2D material Pb based QD hybrid photodetectors was also presented. The introduction of 2D materials such as graphene and MoS_2 improve the gain of QD phototransistors significantly due to the high carrier mobilities of layered 2D materials. QDs act

as the absorbing layer in these hybrid devices, counteracting the lack of absorption in 2D materials due to their atomically thin profile. Devices utilizing graphene suffer from high dark currents due to the semi-metallic nature of graphene, but TMDs such as MoS_2 and WS_2 and other novel 2D materials such as black phosphorous can counteract the problem of high dark current, especially when strong voltage biases are applied.

In future work we are looking at incorporating manganese dopants into PbSe/CdSe QD heterostructures to greater improve the carrier multiplication and Auger up-conversion efficiencies. Manganese doping has already shown to increase visible emission in PbSe/CdSe QDs with a thin shell of CdS in preliminary studies. Continued work on alpha radiation detectors is currently being worked on with a group at the Los Alamos Neutron Scattering Center, where we are working on wire bonding techniques to ensure better contact of top and bottom electrodes before moving on to experimental measurements. Demonstration of alpha particle and gamma ray sensitivity in solid state detectors comprised of PbSe QD films is a significant step toward solid state radiation detectors based on QD films. The high attenuation efficiency and facile solution processing make PbSe QDs an ideal candidate for further study in solid state radiation detectors.

References

(1)   Do we need to revisit the Bohr exciton radius of hot excitons? https://arxiv.org/abs/1105.2205. (accessed March 22 2020).

(2)   Schmitt-Rink, S.; Miller, D. A.; Chemla, D. S. Theory of the linear and nonlinear optical properties of semiconductor microcrystallites. *Phys Rev B Condens Matter* **1987**, *35*, 8113-8125.

(3)   Lipovskii, A.; Kolobkova, E.; Petrikov, V.; Kang, I.; Olkhovets, A.; Krauss, T.; Thomas, M.; Silcox, J.; Wise, F.; Shen, Q.; Kycia, S. Synthesis and characterization of PbSe quantum dots in phosphate glass. *Applied Physics Letters* **1997**, *71*, 3406-3408.

(4)   Alivisatos, A. P. Semiconductor Clusters, Nanocrystals, and Quantum Dots. *Science* **1996**, *271*, 933-937.

(5)   Nozik, A. J. Quantum dot solar cells. *Physica E: Low-dimensional Systems and Nanostructures* **2002**, *14*, 115-120.

(6)   Klimov, V. I.; Mikhailovsky, A. A.; Xu, S.; Malko, A.; Hollingsworth, J. A.; Leatherdale, C. A.; Eisler, H.-J.; Bawendi, M. G. Optical Gain and Stimulated Emission in Nanocrystal Quantum Dots. *Science* **2000**, *290*, 314-317.

(7)   Semonin, O. E.; Luther, J. M.; Beard, M. C. Quantum dots for next-generation photovoltaics. *Materials Today* **2012**, *15*, 508-515.

(8)   Ekimov, A. I. O., A.A. Quantum Size Effect in Three-Dimensional_Microscopic Semiconductor Crystal. *American Institute of Physics* **1981**, *34*, 363-366.

(9)   Ekimov, A. I. O., A.A. . Quantum size effect in the optical-spectra of semiconductor micro-crystals. *Soviet Physics Semiconductors-USSR*. **1982.** , *16* 775–778.

(10)   Rossetti, R.; Nakahara, S.; Brus, L. E. Quantum size effects in the redox potentials, resonance Raman spectra, and electronic spectra of CdS crystallites in aqueous solution. *The Journal of Chemical Physics* **1983**, *79*, 1086-1088.

(11)   Reed, M. A.; Bate, R. T.; Bradshaw, K.; Duncan, W. M.; Frensley, W. R.; Lee, J. W.; Shih, H. D. Spatial quantization in GaAs−AlGaAs multiple quantum dots. *Journal of Vacuum Science & Technology B* **1986**, *4*, 358-360.

(12)   Murray, C. B.; Norris, D. J.; Bawendi, M. G. Synthesis and characterization of nearly monodisperse CdE (E = sulfur, selenium, tellurium) semiconductor nanocrystallites. *Journal of the American Chemical Society* **1993**, *115*, 8706-8715.

(13)   Peng, Z. A.; Peng, X. Formation of High-Quality CdTe, CdSe, and CdS Nanocrystals Using CdO as Precursor. *Journal of the American Chemical Society* **2001**, *123*, 183-184.

(14)   https://sites.google.com/site/ee535test/declan-baugh. (accessed 02/25/2020 2020).

(15)   Moreels, I.; Lambert, K.; Smeets, D.; De Muynck, D.; Nollet, T.; Martins, J. C.; Vanhaecke, F.; Vantomme, A.; Delerue, C.; Allan, G.; Hens, Z. Size-Dependent Optical Properties of Colloidal PbS Quantum Dots. *ACS Nano* **2009**, *3*, 3023-3030.

(16)   Dai, Q.; Wang, Y.; Li, X.; Zhang, Y.; Pellegrino, D. J.; Zhao, M.; Zou, B.; Seo, J.; Wang, Y.; Yu, W. W. Size-Dependent Composition and Molar Extinction Coefficient of PbSe Semiconductor Nanocrystals. *ACS Nano* **2009**, *3*, 1518-1524.

(17)   Lifshitz, E.; Bashouti, M.; Kloper, V.; Kigel, A.; Eisen, M. S.; Berger, S. Synthesis and Characterization of PbSe Quantum Wires, Multipods, Quantum Rods, and Cubes. *Nano Letters* **2003**, *3*, 857-862.

(18)   Houtepen, A. J.; Koole, R.; Vanmaekelbergh, D.; Meeldijk, J.; Hickey, S. G. The Hidden Role of Acetate in the PbSe Nanocrystal Synthesis. *Journal of the American Chemical Society* **2006**, *128*, 6792-6793.

(19)   Koh, W.-k.; Bartnik, A. C.; Wise, F. W.; Murray, C. B. Synthesis of Monodisperse PbSe Nanorods: A Case for Oriented Attachment. *Journal of the American Chemical Society* **2010**, *132*, 3909-3913.

****

(20)   Smith, D. K.; Luther, J. M.; Semonin, O. E.; Nozik, A. J.; Beard, M. C. Tuning the Synthesis of Ternary Lead Chalcogenide Quantum Dots by Balancing Precursor Reactivity. *ACS Nano* **2011**, *5*, 183-190.

(21)   Koh, W. K.; Koposov, A. Y.; Stewart, J. T.; Pal, B. N.; Robel, I.; Pietryga, J. M.; Klimov, V. I. Heavily doped n-type PbSe and PbS nanocrystals using ground-state charge transfer from cobaltocene. *Sci Rep* **2013**, *3*, 2004.

(22)   Bae, W. K.; Joo, J.; Padilha, L. A.; Won, J.; Lee, D. C.; Lin, Q.; Koh, W.-k.; Luo, H.; Klimov, V. I.; Pietryga, J. M. Highly Effective Surface Passivation of PbSe Quantum Dots through Reaction with Molecular Chlorine. *Journal of the American Chemical Society* **2012**, *134*, 20160-20168.

(23)   Pietryga, J. M. S., R. D.; Werder, D.; Stewart, M.H.; Klimov, V. I.; Hollingsworth, J. A. Pushing the Band Gap Envelope: Mid-Infrared Emitting Colloidal PbSe Quantum Dots. *Journal of American Chemical Society* **2004**, *126*, 11752-11753.

(24)   Schaller, R. D.; Klimov, V. I. High efficiency carrier multiplication in PbSe nanocrystals: implications for solar energy conversion. *Phys Rev Lett* **2004**, *92*, 186601.

(25)   Knoll, G. F.: *Radiation Detection and Measurement*; John Wiley and Sons, Inc: New York, NY, 2010; Vol. 4th ed.

(26)   Cirloganu, C. M.; Padilha, L. A.; Lin, Q.; Makarov, N. S.; Velizhanin, K. A.; Luo, H.; Robel, I.; Pietryga, J. M.; Klimov, V. I. Enhanced carrier multiplication in engineered quasi-type-II quantum dots. *Nat Commun* **2014**, *5*, 4148.

(27)   Padilha, L. A.; Stewart, J. T.; Sandberg, R. L.; Bae, W. K.; Koh, W. K.; Pietryga, J. M.; Klimov, V. I. Aspect ratio dependence of auger recombination and carrier multiplication in PbSe nanorods. *Nano Lett* **2013**, *13*, 1092-1099.

(28)   Makarov, N. S.; Lin, Q.; Pietryga, J. M.; Robel, I.; Klimov, V. I. Auger Up-Conversion of Low-Intensity Infrared Light in Engineered Quantum Dots. *ACS Nano* **2016**, *10*, 10829-10841.

(29)   Koh, W.-k.; Yoon, Y.; Murray, C. B. Investigating the Phosphine Chemistry of Se Precursors for the Synthesis of PbSe Nanorods. *Chemistry of Materials* **2011**, *23*, 1825-1829.

(30)   Moreels, I.; Fritzinger, B.; Martins, J. C.; Hens, Z. Surface Chemistry of Colloidal PbSe Nanocrystals. *Journal of the American Chemical Society* **2008**, *130*, 15081-15086.

(31)   Zhang, J.; Gao, J.; Miller, E. M.; Luther, J. M.; Beard, M. C. Diffusion-Controlled Synthesis of PbS and PbSe Quantum Dots with in Situ Halide Passivation for Quantum Dot Solar Cells. *ACS Nano* **2014**, *8*, 614-622.

(32)   Lin, Q.; Yun, H. J.; Liu, W.; Song, H. J.; Makarov, N. S.; Isaienko, O.; Nakotte, T.; Chen, G.; Luo, H.; Klimov, V. I.; Pietryga, J. M. Phase-Transfer Ligand Exchange of Lead Chalcogenide Quantum Dots for Direct Deposition of Thick, Highly Conductive Films. *J Am Chem Soc* **2017**, *139*, 6644-6653.

(33)   Joo, J.; Pietryga, J. M.; McGuire, J. A.; Jeon, S.-H.; Williams, D. J.; Wang, H.-L.; Klimov, V. I. A Reduction Pathway in the Synthesis of PbSe Nanocrystal Quantum Dots. *Journal of the American Chemical Society* **2009**, *131*, 10620-10628.

(34)   Sugimoto, T. Underlying mechanisms in size control of uniform nanoparticles. *Journal of Colloid and Interface Science* **2007**, *309*, 106-118.

(35)   LaMer, V. K.; Dinegar, R. H. Theory, Production and Mechanism of Formation of Monodispersed Hydrosols. *Journal of the American Chemical Society* **1950**, *72*, 4847-4854.

(36)   Hassinen, A.; Moreels, I.; De Nolf, K.; Smet, P. F.; Martins, J. C.; Hens, Z. Short-Chain Alcohols Strip X-Type Ligands and Quench the Luminescence of PbSe and CdSe Quantum Dots, Acetonitrile Does Not. *Journal of the American Chemical Society* **2012**, *134*, 20705-20712.

(37)   Nagpal, P.; Klimov, V. I. Role of mid-gap states in charge transport and photoconductivity in semiconductor nanocrystal films. *Nat Commun* **2011**, *2*, 486.

(38)   Pietryga, J. M.; Werder, D. J.; Williams, D. J.; Casson, J. L.; Schaller, R. D.; Klimov, V. I.; Hollingsworth, J. A. Utilizing the Lability of Lead Selenide to Produce Heterostructured

****

Nanocrystals with Bright, Stable Infrared Emission. *Journal of the American Chemical Society* **2008**, *130*, 4879-4885.

(39)   Ithurria, S.; Talapin, D. V. Colloidal Atomic Layer Deposition (c-ALD) using Self-Limiting Reactions at Nanocrystal Surface Coupled to Phase Transfer between Polar and Nonpolar Media. *Journal of the American Chemical Society* **2012**, *134*, 18585-18590.

(40)   Sagar, L. K.; Walravens, W.; Zhao, Q.; Vantomme, A.; Geiregat, P.; Hens, Z. PbS/CdS Core/Shell Quantum Dots by Additive, Layer-by-Layer Shell Growth. *Chemistry of Materials* **2016**, *28*, 6953-6959.

(41)   Zhao, H.; Jin, L.; Zhou, Y.; Bandar, A.; Fan, Z.; Govorov, A. O.; Mi, Z.; Sun, S.; Rosei, F.; Vomiero, A. Green synthesis of near infrared core/shell quantum dots for photocatalytic hydrogen production. *Nanotechnology* **2016**, *27*, 495405.

(42)   Greytak, A. B.; Allen, P. M.; Liu, W.; Zhao, J.; Young, E. R.; Popović, Z.; Walker, B. J.; Nocera, D. G.; Bawendi, M. G. Alternating layer addition approach to CdSe/CdS core/shell quantum dots with near-unity quantum yield and high on-time fractions. *Chemical Science* **2012**, *3*, 2028-2034.

(43)   Lee, D. C.; Robel, I.; Pietryga, J. M.; Klimov, V. I. Infrared-Active Heterostructured Nanocrystals with Ultralong Carrier Lifetimes. *Journal of the American Chemical Society* **2010**, *132*, 9960-9962.

(44)   Hanson, C. J.; Hartmann, N. F.; Singh, A.; Ma, X.; DeBenedetti, W. J. I.; Casson, J. L.; Grey, J. K.; Chabal, Y. J.; Malko, A. V.; Sykora, M.; Piryatinski, A.; Htoon, H.; Hollingsworth, J. A. Giant PbSe/CdSe/CdSe Quantum Dots: Crystal-Structure-Defined Ultrastable Near-Infrared Photoluminescence from Single Nanocrystals. *Journal of the American Chemical Society* **2017**, *139*, 11081-11088.

(45)   McDonald, S. A.; Konstantatos, G.; Zhang, S.; Cyr, P. W.; Klem, E. J.; Levina, L.; Sargent, E. H. Solution-processed PbS quantum dot infrared photodetectors and photovoltaics. *Nat Mater* **2005**, *4*, 138-142.

(46)   Konstantatos, G.; Howard, I.; Fischer, A.; Hoogland, S.; Clifford, J.; Klem, E.; Levina, L.; Sargent, E. H. Ultrasensitive solution-cast quantum dot photodetectors. *Nature* **2006**, *442*, 180-183.

(47)   Chernomordik, B. D.; Marshall, A. R.; Pach, G. F.; Luther, J. M.; Beard, M. C. Quantum Dot Solar Cell Fabrication Protocols. *Chemistry of Materials* **2017**, *29*, 189-198.

(48)   Maulu, A.; Rodríguez-Cantó, P. J.; Navarro-Arenas, J.; Abargues, R.; Sánchez-Royo, J. F.; García-Calzada, R.; Martínez Pastor, J. P. Strongly-coupled PbS QD solids by doctor blading for IR photodetection. *RSC Advances* **2016**, *6*, 80201-80212.

(49)   Sliz, R.; Lejay, M.; Fan, J. Z.; Choi, M.-J.; Kinge, S.; Hoogland, S.; Fabritius, T.; García de Arquer, F. P.; Sargent, E. H. Stable Colloidal Quantum Dot Inks Enable Inkjet-Printed High-Sensitivity Infrared Photodetectors. *ACS Nano* **2019**, *13*, 11988-11995.

(50)   Kagan, C. R.; Murray, C. B. Charge transport in strongly coupled quantum dot solids. *Nat Nanotechnol* **2015**, *10*, 1013-1026.

(51)   Kagan, C. R.; Lifshitz, E.; Sargent, E. H.; Talapin, D. V. Building devices from colloidal quantum dots. *Science* **2016**, *353*.

(52)   Luther, J. M.; Law, M.; Song, Q.; Perkins, C. L.; Beard, M. C.; Nozik, A. J. Structural, Optical, and Electrical Properties of Self-Assembled Films of PbSe Nanocrystals Treated with 1,2-Ethanedithiol. *ACS Nano* **2008**, *2*, 271-280.

(53)   Abboud, J. L. M.; Notari, R. Critical compilation of scales of solvent parameters. Part I. Pure, non-hydrogen bond donor solvents. *Pure and Applied Chemistry* **1999**, *71*, 645.

(54)   Tang, J.; Kemp, K. W.; Hoogland, S.; Jeong, K. S.; Liu, H.; Levina, L.; Furukawa, M.; Wang, X.; Debnath, R.; Cha, D.; Chou, K. W.; Fischer, A.; Amassian, A.; Asbury, J. B.; Sargent, E. H. Colloidal-quantum-dot photovoltaics using atomic-ligand passivation. *Nat Mater* **2011**, *10*, 765-771.

****

(55)   Chuang, C. H.; Brown, P. R.; Bulovic, V.; Bawendi, M. G. Improved performance and stability in quantum dot solar cells through band alignment engineering. *Nat Mater* **2014**, *13*, 796-801.

(56)   Brown, P. R. K., D.; Lunt, R.R.; Zhao, N.; Bawendi, M.G.; Grossman, J.C.; Bulovic, V. Energy Level Modification in Lead Sulfide Quantum Dot Thin Films through Ligand Exchange. *ACS Nano* **2014**, *8*, 5863-5872.

(57)   Talapin, D. V.; Murray, C. B. PbSe Nanocrystal Solids for n- and p-Channel Thin Film Field-Effect Transistors. *Science* **2005**, *310*, 86-89.

(58)   Klem, E. J. D.; Shukla, H.; Hinds, S.; MacNeil, D. D.; Levina, L.; Sargent, E. H. Impact of dithiol treatment and air annealing on the conductivity, mobility, and hole density in PbS colloidal quantum dot solids. *Applied Physics Letters* **2008**, *92*.

(59)   Oh, S. J.; Berry, N. E.; Choi, J.-H.; Gaulding, E. A.; Paik, T.; Hong, S.-H.; Murray, C. B.; Kagan, C. R. Stoichiometric Control of Lead Chalcogenide Nanocrystal Solids to Enhance Their Electronic and Optoelectronic Device Performance. *ACS Nano* **2013**, *7*, 2413-2421.

(60)   Oh, S. J.; Berry, N. E.; Choi, J. H.; Gaulding, E. A.; Lin, H.; Paik, T.; Diroll, B. T.; Muramoto, S.; Murray, C. B.; Kagan, C. R. Designing high-performance PbS and PbSe nanocrystal electronic devices through stepwise, post-synthesis, colloidal atomic layer deposition. *Nano Lett* **2014**, *14*, 1559-1566.

(61)   Mosahebfard, A.; Jahromi, H. D.; Sheikhi, M. H. Highly Sensitive, Room Temperature Methane Gas Sensor Based on Lead Sulfide Colloidal Nanocrystals. *IEEE Sensors Journal* **2016**, *16*, 4174-4179.

(62)   Carey, G. H.; Levina, L.; Comin, R.; Voznyy, O.; Sargent, E. H. Record Charge Carrier Diffusion Length in Colloidal Quantum Dot Solids via Mutual Dot-To-Dot Surface Passivation. *Adv Mater* **2015**, *27*, 3325-3330.

(63)   Liu, Y.; Tolentino, J.; Gibbs, M.; Ihly, R.; Perkins, C. L.; Liu, Y.; Crawford, N.; Hemminger, J. C.; Law, M. PbSe quantum dot field-effect transistors with air-stable electron mobilities above 7 cm2 V(-1) s(-1). *Nano Lett* **2013**, *13*, 1578-1587.

(64)   Liu, Y.; Gibbs, M.; Perkins, C. L.; Tolentino, J.; Zarghami, M. H.; Bustamante, J., Jr.; Law, M. Robust, functional nanocrystal solids by infilling with atomic layer deposition. *Nano Lett* **2011**, *11*, 5349-5355.

(65)   Balazs, D. M.; Matysiak, B. M.; Momand, J.; Shulga, A. G.; Ibanez, M.; Kovalenko, M. V.; Kooi, B. J.; Loi, M. A. Electron Mobility of 24 cm(2) V(-1) s(-1) in PbSe Colloidal-Quantum-Dot Superlattices. *Adv Mater* **2018**, *30*, e1802265.

(66)   Ten Cate, S.; Liu, Y.; Suchand Sandeep, C. S.; Kinge, S.; Houtepen, A. J.; Savenije, T. J.; Schins, J. M.; Law, M.; Siebbeles, L. D. Activating Carrier Multiplication in PbSe Quantum Dot Solids by Infilling with Atomic Layer Deposition. *J Phys Chem Lett* **2013**, *4*, 1766-1770.

(67)   Hines, M. A.; Guyot-Sionnest, P. Synthesis and Characterization of Strongly Luminescing ZnS-Capped CdSe Nanocrystals. *The Journal of Physical Chemistry* **1996**, *100*, 468-471.

(68)   Kim, S.; Fisher, B.; Eisler, H.-J.; Bawendi, M. Type-II Quantum Dots: CdTe/CdSe(Core/Shell) and CdSe/ZnTe(Core/Shell) Heterostructures. *Journal of the American Chemical Society* **2003**, *125*, 11466-11467.

(69)   Balet, L. P.; Ivanov, S. A.; Piryatinski, A.; Achermann, M.; Klimov, V. I. Inverted Core/Shell Nanocrystals Continuously Tunable between Type-I and Type-II Localization Regimes. *Nano Letters* **2004**, *4*, 1485-1488.

(70)   García-Santamaría, F.; Chen, Y.; Vela, J.; Schaller, R. D.; Hollingsworth, J. A.; Klimov, V. I. Suppressed Auger Recombination in "Giant" Nanocrystals Boosts Optical Gain Performance. *Nano Letters* **2009**, *9*, 3482-3488.

(71)   Lim, J.; Park, Y.-S.; Wu, K.; Yun, H. J.; Klimov, V. I. Droop-Free Colloidal Quantum Dot Light-Emitting Diodes. *Nano Letters* **2018**, *18*, 6645-6653.

****

(72)   Bae, W. K.; Padilha, L. A.; Park, Y.-S.; McDaniel, H.; Robel, I.; Pietryga, J. M.; Klimov, V. I. Controlled Alloying of the Core–Shell Interface in CdSe/CdS Quantum Dots for Suppression of Auger Recombination. *ACS Nano* **2013**, *7*, 3411-3419.

(73)   Chen, O.; Zhao, J.; Chauhan, V. P.; Cui, J.; Wong, C.; Harris, D. K.; Wei, H.; Han, H.-S.; Fukumura, D.; Jain, R. K.; Bawendi, M. G. Compact high-quality CdSe–CdS core–shell nanocrystals with narrow emission linewidths and suppressed blinking. *Nature Materials* **2013**, *12*, 445-451.

(74)   Lin, Q.; Makarov, N. S.; Koh, W.-k.; Velizhanin, K. A.; Cirloganu, C. M.; Luo, H.; Klimov, V. I.; Pietryga, J. M. Design and Synthesis of Heterostructured Quantum Dots with Dual Emission in the Visible and Infrared. *ACS Nano* **2015**, *9*, 539-547.

(75)   Casavola, M.; van Huis, M. A.; Bals, S.; Lambert, K.; Hens, Z.; Vanmaekelbergh, D. Anisotropic Cation Exchange in PbSe/CdSe Core/Shell Nanocrystals of Different Geometry. *Chemistry of Materials* **2012**, *24*, 294-302.

(76)   Nan, W.; Niu, Y.; Qin, H.; Cui, F.; Yang, Y.; Lai, R.; Lin, W.; Peng, X. Crystal Structure Control of Zinc-Blende CdSe/CdS Core/Shell Nanocrystals: Synthesis and Structure-Dependent Optical Properties. *Journal of the American Chemical Society* **2012**, *134*, 19685-19693.

(77)   Nag, A.; Kovalenko, M. V.; Lee, J.-S.; Liu, W.; Spokoyny, B.; Talapin, D. V. Metal-free Inorganic Ligands for Colloidal Nanocrystals: S2–, HS–, Se2–, HSe–, Te2–, HTe–, TeS32–, OH–, and NH2– as Surface Ligands. *Journal of the American Chemical Society* **2011**, *133*, 10612-10620.

(78)   Semonin, O. E.; Johnson, J. C.; Luther, J. M.; Midgett, A. G.; Nozik, A. J.; Beard, M. C. Absolute Photoluminescence Quantum Yields of IR-26 Dye, PbS, and PbSe Quantum Dots. *The Journal of Physical Chemistry Letters* **2010**, *1*, 2445-2450.

(79)   Pu, C.; Zhou, J.; Lai, R.; Niu, Y.; Nan, W.; Peng, X. Highly reactive, flexible yet green Se precursor for metal selenide nanocrystals: Se-octadecene suspension (Se-SUS). *Nano Research* **2013**, *6*, 652-670.

(80)   Manna, L.; Milliron, D. J.; Meisel, A.; Scher, E. C.; Alivisatos, A. P. Controlled growth of tetrapod-branched inorganic nanocrystals. *Nature Materials* **2003**, *2*, 382-385.

(81)   Shieh, F.; Saunders, A. E.; Korgel, B. A. General Shape Control of Colloidal CdS, CdSe, CdTe Quantum Rods and Quantum Rod Heterostructures. *The Journal of Physical Chemistry B* **2005**, *109*, 8538-8542.

(82)   Talapin, D. V. L., J.; Kovalenko, M. V.; Shevchenko, E. V. Prospects of Colloidal Nanocrystals for Electronic and Optoelectronic Applications. *Chemical Reviews* **2010**, *110*.

(83)   Konstantatos, G.; Sargent, E. H. Colloidal quantum dot photodetectors. *Infrared Physics & Technology* **2011**, *54*, 278-282.

(84)   Schaller, R. D.; Agranovich, V. M.; Klimov, V. I. High-efficiency carrier multiplication through direct photogeneration of multi-excitons via virtual single-exciton states. *Nature Physics* **2005**, *1*, 189-194.

(85)   Zhang, C.; Xia, Y.; Zhang, Z.; Huang, Z.; Lian, L.; Miao, X.; Zhang, D.; Beard, M. C.; Zhang, J. Combination of Cation Exchange and Quantized Ostwald Ripening for Controlling Size Distribution of Lead Chalcogenide Quantum Dots. *Chemistry of Materials* **2017**, *29*, 3615-3622.

(86)   Xing, X.; Liu, C.; Shang, W.; Qin, H.; Chen, Z.; Cao, F. Liquid-type structure near-infrared light-emitting diodes based on PbSe quantum dots for acetylene gas detection. *Infrared Physics & Technology* **2019**, *98*, 315-322.

(87)   Konstantatos, G.; Sargent, E. H. Nanostructured materials for photon detection. *Nat Nanotechnol* **2010**, *5*, 391-400.

(88)   Soole, J. B. D. S., H. InGaAs Metal-Semiconductor-Metal Photodetectors for Long Wavelength Optical Communications. *IEEE JOURNAL OF QUANTUM ELECTRONICS* **1991**, *27*.

(89)   Coe, S.; Woo, W.-K.; Bawendi, M.; Bulović, V. Electroluminescence from single monolayers of nanocrystals in molecular organic devices. *Nature* **2002**, *420*, 800-803.

****

(90)   Ning, Z.; Voznyy, O.; Pan, J.; Hoogland, S.; Adinolfi, V.; Xu, J.; Li, M.; Kirmani, A. R.; Sun, J. P.; Minor, J.; Kemp, K. W.; Dong, H.; Rollny, L.; Labelle, A.; Carey, G.; Sutherland, B.; Hill, I.; Amassian, A.; Liu, H.; Tang, J.; Bakr, O. M.; Sargent, E. H. Air-stable n-type colloidal quantum dot solids. *Nat Mater* **2014**, *13*, 822-828.

(91)   Zarghami, M. H. L., Y.; Gibbs, M.; Gebremichael, E.; Webster, C.; Law, M. p-Type PbSe and PbS Quantum Dot Solids Prepared with Short-Chain Acids and Diacids. *ACS Nano* **2010**, *4*, 2475-2485.

(92)   Hetsch, F.; Zhao, N.; Kershaw, S. V.; Rogach, A. L. Quantum dot field effect transistors. *Materials Today* **2013**, *16*, 312-325.

(93)   Carey, G. H.; Abdelhady, A. L.; Ning, Z.; Thon, S. M.; Bakr, O. M.; Sargent, E. H. Colloidal Quantum Dot Solar Cells. *Chemical Reviews* **2015**, *115*, 12732-12763.

(94)   Sayevich, V.; Gaponik, N.; Plötner, M.; Kruszynska, M.; Gemming, T.; Dzhagan, V. M.; Akhavan, S.; Zahn, D. R. T.; Demir, H. V.; Eychmüller, A. Stable Dispersion of Iodide-Capped PbSe Quantum Dots for High-Performance Low-Temperature Processed Electronics and Optoelectronics. *Chemistry of Materials* **2015**, *27*, 4328-4337.

(95)   Osedach, T. P. Z., N.; Andrew, T. L.; Brown, P.R..; Wanger, D. D.; Strasfeld,D. B.; Chang, L.; Bawendi,M. G.; Bulovic, V. . Bias-Stress Effect in 1,2-Ethanedithiol-Treated PbS Quantum Dot Field-Effect Transistors. *ACS Nano* **2012**, *6*, 3121-3127.

(96)   Leschkies, K. S.; Kang, M. S.; Aydil, E. S.; Norris, D. J. Influence of Atmospheric Gases on the Electrical Properties of PbSe Quantum-Dot Films. *The Journal of Physical Chemistry C* **2010**, *114*, 9988-9996.

(97)   Balazs, D. M.; Nugraha, M. I.; Bisri, S. Z.; Sytnyk, M.; Heiss, W.; Loi, M. A. Reducing charge trapping in PbS colloidal quantum dot solids. *Applied Physics Letters* **2014**, *104*, 112104.

(98)   Liu, Y.; Gibbs, M.; Puthussery, J.; Gaik, S.; Ihly, R.; Hillhouse, H. W.; Law, M. Dependence of carrier mobility on nanocrystal size and ligand length in PbSe nanocrystal solids. *Nano Lett* **2010**, *10*, 1960-1969.

(99)   NanoTech, U. C.: Savannah S100, S200, and S300 Atomic Layer Deposition Systems User Manual. 2004; pp 54.

(100)   Clifford, J. P.; Konstantatos, G.; Johnston, K. W.; Hoogland, S.; Levina, L.; Sargent, E. H. Fast, sensitive and spectrally tuneable colloidal-quantum-dot photodetectors. *Nat Nanotechnol* **2009**, *4*, 40-44.

(101)   Saran, R.; Curry, R. J. Lead sulphide nanocrystal photodetector technologies. *Nature Photonics* **2016**, *10*, 81-92.

(102)   De Iacovo, A.; Venettacci, C.; Colace, L.; Scopa, L.; Foglia, S. PbS Colloidal Quantum Dot Visible-Blind Photodetector for Early Indoor Fire Detection. *IEEE Sensors Journal* **2017**, *17*, 4454-4459.

(103)   Yan, L.; Zhang, Y.; Zhang, T.; Feng, Y.; Zhu, K.; Wang, D.; Cui, T.; Yin, J.; Wang, Y.; Zhao, J.; Yu, W. W. Tunable near-infrared luminescence of PbSe quantum dots for multigas analysis. *Anal Chem* **2014**, *86*, 11312-11318.

(104)   Pal, B. N.; Robel, I.; Mohite, A.; Laocharoensuk, R.; Werder, D. J.; Klimov, V. I. High-Sensitivity p−n Junction Photodiodes Based on PbS Nanocrystal Quantum Dots. *Advanced Functional Materials* **2012**, *22*, 1741-1748.

(105)   Ankah, G. N.; Büchele, P.; Poulsen, K.; Rauch, T.; Tedde, S. F.; Gimmler, C.; Schmidt, O.; Kraus, T. PbS quantum dot based hybrid-organic photodetectors for X-ray sensing. *Organic Electronics* **2016**, *33*, 201-206.

(106)   Tan, T. T.; Selvan, S. T.; Zhao, L.; Gao, S.; Ying, J. Y. Size Control, Shape Evolution, and Silica Coating of Near-Infrared-Emitting PbSe Quantum Dots. *Chemistry of Materials* **2007**, *19*, 3112-3117.

(107)   Murray, C. B. S., S.; Gaschler, W.; Doyle, H.; Betley, T.A.; Kagan, C.R. Colloidal synthesis of nanocrystals and nanocrystal superlattices. *IBM J. RES. & DEV.* **2001**, *45*, 47-56.

(108)   Sargent, E. H. In *Tilte*, Hong Kong, China2004.

****

(109)   Koh, W. K.; Saudari, S. R.; Fafarman, A. T.; Kagan, C. R.; Murray, C. B. Thiocyanate-capped PbS nanocubes: ambipolar transport enables quantum dot based circuits on a flexible substrate. *Nano Lett* **2011**, *11*, 4764-4767.
(110)   Otto, T.; Miller, C.; Tolentino, J.; Liu, Y.; Law, M.; Yu, D. Gate-dependent carrier diffusion length in lead selenide quantum dot field-effect transistors. *Nano Lett* **2013**, *13*, 3463-3469.
(111)   Lee, J. S.; Kovalenko, M. V.; Huang, J.; Chung, D. S.; Talapin, D. V. Band-like transport, high electron mobility and high photoconductivity in all-inorganic nanocrystal arrays. *Nat Nanotechnol* **2011**, *6*, 348-352.
(112)   Pietryga, J. M.; Park, Y. S.; Lim, J.; Fidler, A. F.; Bae, W. K.; Brovelli, S.; Klimov, V. I. Spectroscopic and Device Aspects of Nanocrystal Quantum Dots. *Chem Rev* **2016**, *116*, 10513-10622.
(113)   Ellingson, R. J.; Beard, M. C.; Johnson, J. C.; Yu, P.; Micic, O. I.; Nozik, A. J.; Shabaev, A.; Efros, A. L. Highly Efficient Multiple Exciton Generation in Colloidal PbSe and PbS Quantum Dots. *Nano Letters* **2005**, *5*, 865-871.
(114)   Semonin, O. E.; Luther, J. M.; Choi, S.; Chen, H.-Y.; Gao, J.; Nozik, A. J.; Beard, M. C. Peak External Photocurrent Quantum Efficiency Exceeding 100% via MEG in a Quantum Dot Solar Cell. *Science* **2011**, *334*, 1530-1533.
(115)   Böhm, M. L.; Jellicoe, T. C.; Tabachnyk, M.; Davis, N. J. L. K.; Wisnivesky-Rocca-Rivarola, F.; Ducati, C.; Ehrler, B.; Bakulin, A. A.; Greenham, N. C. Lead Telluride Quantum Dot Solar Cells Displaying External Quantum Efficiencies Exceeding 120%. *Nano Letters* **2015**, *15*, 7987-7993.
(116)   Nozik, A. J. Quantum dot solar cells. *Physica E Low-Dimensional Systems and Nanostructures* **2002**, *14*, 115-120.
(117)   Hanna, M. C.; Nozik, A. J. Solar conversion efficiency of photovoltaic and photoelectrolysis cells with carrier multiplication absorbers. *Journal of Applied Physics* **2006**, *100*, 074510.
(118)   Hanna, M. C.; Beard, M. C.; Nozik, A. J. Effect of Solar Concentration on the Thermodynamic Power Conversion Efficiency of Quantum-Dot Solar Cells Exhibiting Multiple Exciton Generation. *The Journal of Physical Chemistry Letters* **2012**, *3*, 2857-2862.
(119)   Nozik, A. J.; Beard, M. C.; Luther, J. M.; Law, M.; Ellingson, R. J.; Johnson, J. C. Semiconductor Quantum Dots and Quantum Dot Arrays and Applications of Multiple Exciton Generation to Third-Generation Photovoltaic Solar Cells. *Chemical Reviews* **2010**, *110*, 6873-6890.
(120)   Midgett, A. G.; Luther, J. M.; Stewart, J. T.; Smith, D. K.; Padilha, L. A.; Klimov, V. I.; Nozik, A. J.; Beard, M. C. Size and Composition Dependent Multiple Exciton Generation Efficiency in PbS, PbSe, and PbSxSe1−x Alloyed Quantum Dots. *Nano Letters* **2013**, *13*, 3078-3085.
(121)   Zhang, J.; Tolentino, J.; Smith, E. R.; Zhang, J.; Beard, M. C.; Nozik, A. J.; Law, M.; Johnson, J. C. Carrier Transport in PbS and PbSe QD Films Measured by Photoluminescence Quenching. *The Journal of Physical Chemistry C* **2014**, *118*, 16228-16235.
(122)   Gao, J.; Jeong, S.; Lin, F.; Erslev, P. T.; Semonin, O. E.; Luther, J. M.; Beard, M. C. Improvement in carrier transport properties by mild thermal annealing of PbS quantum dot solar cells. *Applied Physics Letters* **2013**, *102*, 043506.
(123)   Kramer, I. J.; Levina, L.; Debnath, R.; Zhitomirsky, D.; Sargent, E. H. Solar cells using quantum funnels. *Nano Lett* **2011**, *11*, 3701-3706.
(124)   Xu, F.; Ma, X.; Haughn, C. R.; Benavides, J.; Doty, M. F.; Cloutier, S. G. Efficient Exciton Funneling in Cascaded PbS Quantum Dot Superstructures. *ACS Nano* **2011**, *5*, 9950-9957.
(125)   Gao, J.; Perkins, C. L.; Luther, J. M.; Hanna, M. C.; Chen, H.-Y.; Semonin, O. E.; Nozik, A. J.; Ellingson, R. J.; Beard, M. C. n-Type Transition Metal Oxide as a Hole Extraction Layer in PbS Quantum Dot Solar Cells. *Nano Letters* **2011**, *11*, 3263-3266.

****

(126)   Luther, J. M.; Law, M.; Beard, M. C.; Song, Q.; Reese, M. O.; Ellingson, R. J.; Nozik, A. J. Schottky Solar Cells Based on Colloidal Nanocrystal Films. *Nano Letters* **2008**, *8*, 3488-3492.
(127)   Luther, J. M.; Gao, J.; Lloyd, M. T.; Semonin, O. E.; Beard, M. C.; Nozik, A. J. Stability Assessment on a 3% Bilayer PbS/ZnO Quantum Dot Heterojunction Solar Cell. *Advanced Materials* **2010**, *22*, 3704-3707.
(128)   Gao, J.; Luther, J. M.; Semonin, O. E.; Ellingson, R. J.; Nozik, A. J.; Beard, M. C. Quantum Dot Size Dependent J–V Characteristics in Heterojunction ZnO/PbS Quantum Dot Solar Cells. *Nano Letters* **2011**, *11*, 1002-1008.
(129)   Cao, Y.; Stavrinadis, A.; Lasanta, T.; So, D.; Konstantatos, G. The role of surface passivation for efficient and photostable PbS quantum dot solar cells. *Nature Energy* **2016**, *1*, 16035.
(130)   Zhao, N.; Osedach, T. P.; Chang, L.-Y.; Geyer, S. M.; Wanger, D.; Binda, M. T.; Arango, A. C.; Bawendi, M. G.; Bulovic, V. Colloidal PbS Quantum Dot Solar Cells with High Fill Factor. *ACS Nano* **2010**, *4*, 3743-3752.
(131)   Colvin, V. L.; Schlamp, M. C.; Alivisatos, A. P. Light-emitting diodes made from cadmium selenide nanocrystals and a semiconducting polymer. *Nature* **1994**, *370*, 354-357.
(132)   Mueller, A. H.; Petruska, M. A.; Achermann, M.; Werder, D. J.; Akhadov, E. A.; Koleske, D. D.; Hoffbauer, M. A.; Klimov, V. I. Multicolor Light-Emitting Diodes Based on Semiconductor Nanocrystals Encapsulated in GaN Charge Injection Layers. *Nano Letters* **2005**, *5*, 1039-1044.
(133)   Stouwdam, J. W.; Janssen, R. A. J. Red, green, and blue quantum dot LEDs with solution processable ZnO nanocrystal electron injection layers. *Journal of Materials Chemistry* **2008**, *18*, 1889-1894.
(134)   Leatherdale, C. A.; Kagan, C. R.; Morgan, N. Y.; Empedocles, S. A.; Kastner, M. A.; Bawendi, M. G. Photoconductivity in CdSe quantum dot solids. *Physical Review B* **2000**, *62*, 2669-2680.
(135)   Rosen, E. L.; Sawvel, A. M.; Milliron, D. J.; Helms, B. A. Influence of Surface Composition on Electronic Transport through Naked Nanocrystal Networks. *Chemistry of Materials* **2014**, *26*, 2214-2217.
(136)   Rosen, E. L.; Buonsanti, R.; Llordes, A.; Sawvel, A. M.; Milliron, D. J.; Helms, B. A. Exceptionally Mild Reactive Stripping of Native Ligands from Nanocrystal Surfaces by Using Meerwein's Salt. *Angewandte Chemie* **2012**, *51*, 684-689.
(137)   Hwang, E. H.; Adam, S.; Sarma, S. D. Carrier transport in two-dimensional graphene layers. *Phys Rev Lett* **2007**, *98*, 186806.
(138)   Novoselov, K. S.; Geim, A. K.; Morozov, S. V.; Jiang, D.; Zhang, Y.; Dubonos, S. V.; Grigorieva, I. V.; Firsov, A. A. Electric Field Effect in Atomically Thin Carbon Films. *Science* **2004**, *306*, 666-669.
(139)   Wang, Q. H.; Kalantar-Zadeh, K.; Kis, A.; Coleman, J. N.; Strano, M. S. Electronics and optoelectronics of two-dimensional transition metal dichalcogenides. *Nat Nanotechnol* **2012**, *7*, 699-712.
(140)   Xia, F.; Wang, H.; Xiao, D.; Dubey, M.; Ramasubramaniam, A. Two-dimensional material nanophotonics. *Nature Photonics* **2014**, *8*, 899-907.
(141)   Dawlaty, J. M.; Shivaraman, S.; Strait, J.; George, P.; Chandrashekhar, M.; Rana, F.; Spencer, M. G.; Veksler, D.; Chen, Y. Measurement of the optical absorption spectra of epitaxial graphene from terahertz to visible. *Applied Physics Letters* **2008**, *93*.
(142)   Nair, R. R.; Blake, P.; Grigorenko, A. N.; Novoselov, K. S.; Booth, T. J.; Stauber, T.; Peres, N. M. R.; Geim, A. K. Fine Structure Constant Defines Visual Transparency of Graphene. *Science* **2008**, *320*, 1308-1308.
(143)   Kuzmenko, A. B.; van Heumen, E.; Carbone, F.; van der Marel, D. Universal optical conductance of graphite. *Phys Rev Lett* **2008**, *100*, 117401.

****

(144)   Zhang, B. Y.; Liu, T.; Meng, B.; Li, X.; Liang, G.; Hu, X.; Wang, Q. J. Broadband high photoresponse from pure monolayer graphene photodetector. *Nat Commun* **2013**, *4*, 1811.
(145)   Malouf, A.; Henderson-Sapir, O.; Set, S.; Yamashita, S.; Ottaway, D. J. Two-photon absorption and saturable absorption of mid-IR in graphene. *Applied Physics Letters* **2019**, *114*.
(146)   Dawlaty, J. M.; Shivaraman, S.; Chandrashekhar, M.; Rana, F.; Spencer, M. G. Measurement of ultrafast carrier dynamics in epitaxial graphene. *Applied Physics Letters* **2008**, *92*.
(147)   Brida, D.; Tomadin, A.; Manzoni, C.; Kim, Y. J.; Lombardo, A.; Milana, S.; Nair, R. R.; Novoselov, K. S.; Ferrari, A. C.; Cerullo, G.; Polini, M. Ultrafast collinear scattering and carrier multiplication in graphene. *Nat Commun* **2013**, *4*, 1987.
(148)   Liu, X.; Guo, Q.; Qiu, J. Emerging Low-Dimensional Materials for Nonlinear Optics and Ultrafast Photonics. *Advanced Materials* **2017**, *29*, 1605886.
(149)   Li, Z. Q.; Henriksen, E. A.; Jiang, Z.; Hao, Z.; Martin, M. C.; Kim, P.; Stormer, H. L.; Basov, D. N. Dirac charge dynamics in graphene by infrared spectroscopy. *Nature Physics* **2008**, *4*, 532-535.
(150)   Wang, F.; Zhang, Y.; Tian, C.; Girit, C.; Zettl, A.; Crommie, M.; Shen, Y. R. Gate-Variable Optical Transitions in Graphene. *Science* **2008**, *320*, 206-209.
(151)   Zhang, Y.; Tang, T.-T.; Girit, C.; Hao, Z.; Martin, M. C.; Zettl, A.; Crommie, M. F.; Shen, Y. R.; Wang, F. Direct observation of a widely tunable bandgap in bilayer graphene. *Nature* **2009**, *459*, 820.
(152)   Das Sarma, S.; Adam, S.; Hwang, E. H.; Rossi, E. Electronic transport in two-dimensional graphene. *Reviews of Modern Physics* **2011**, *83*, 407-470.
(153)   Banszerus, L.; Schmitz, M.; Engels, S.; Dauber, J.; Oellers, M.; Haupt, F.; Watanabe, K.; Taniguchi, T.; Beschoten, B.; Stampfer, C. Ultrahigh-mobility graphene devices from chemical vapor deposition on reusable copper. *Science Advances* **2015**, *1*, e1500222.
(154)   Bolotin, K. I.; Sikes, K. J.; Jiang, Z.; Klima, M.; Fudenberg, G.; Hone, J.; Kim, P.; Stormer, H. L. Ultrahigh electron mobility in suspended graphene. *Solid State Communications* **2008**, *146*, 351-355.
(155)   Farmer, D. B.; Chiu, H.-Y.; Lin, Y.-M.; Jenkins, K. A.; Xia, F.; Avouris, P. Utilization of a Buffered Dielectric to Achieve High Field-Effect Carrier Mobility in Graphene Transistors. *Nano Letters* **2009**, *9*, 4474-4478.
(156)   Mueller, T.; Xia, F.; Avouris, P. Graphene photodetectors for high-speed optical communications. *Nature Photonics* **2010**, *4*, 297-301.
(157)   Gan, X.; Shiue, R.-J.; Gao, Y.; Meric, I.; Heinz, T. F.; Shepard, K.; Hone, J.; Assefa, S.; Englund, D. Chip-integrated ultrafast graphene photodetector with high responsivity. *Nature Photonics* **2013**, *7*, 883-887.
(158)   Han, M. Y.; Ozyilmaz, B.; Zhang, Y.; Kim, P. Energy band-gap engineering of graphene nanoribbons. *Phys Rev Lett* **2007**, *98*, 206805.
(159)   Li, X.; Wang, X.; Zhang, L.; Lee, S.; Dai, H. Chemically Derived, Ultrasmooth Graphene Nanoribbon Semiconductors. *Science* **2008**, *319*, 1229-1232.
(160)   Chen, Y.-C.; de Oteyza, D. G.; Pedramrazi, Z.; Chen, C.; Fischer, F. R.; Crommie, M. F. Tuning the Band Gap of Graphene Nanoribbons Synthesized from Molecular Precursors. *ACS Nano* **2013**, *7*, 6123-6128.
(161)   Bai, J.; Zhong, X.; Jiang, S.; Huang, Y.; Duan, X. Graphene nanomesh. *Nature Nanotechnology* **2010**, *5*, 190.
(162)   Ouyang, F.; Peng, S.; Liu, Z.; Liu, Z. Bandgap Opening in Graphene Antidot Lattices: The Missing Half. *ACS Nano* **2011**, *5*, 4023-4030.
(163)   Balog, R.; Jørgensen, B.; Nilsson, L.; Andersen, M.; Rienks, E.; Bianchi, M.; Fanetti, M.; Lægsgaard, E.; Baraldi, A.; Lizzit, S.; Sljivancanin, Z.; Besenbacher, F.; Hammer, B.; Pedersen, T. G.; Hofmann, P.; Hornekær, L. Bandgap opening in graphene induced by patterned hydrogen adsorption. *Nature Materials* **2010**, *9*, 315.

****

(164)   Samarakoon, D. K.; Wang, X.-Q. Tunable Band Gap in Hydrogenated Bilayer Graphene. *ACS Nano* **2010**, *4*, 4126-4130.
(165)   Park, J.; Jo, S. B.; Yu, Y.-J.; Kim, Y.; Yang, J. W.; Lee, W. H.; Kim, H. H.; Hong, B. H.; Kim, P.; Cho, K.; Kim, K. S. Single-Gate Bandgap Opening of Bilayer Graphene by Dual Molecular Doping. *Advanced Materials* **2012**, *24*, 407-411.
(166)   Zhang, H.; Bekyarova, E.; Huang, J.-W.; Zhao, Z.; Bao, W.; Wang, F.; Haddon, R. C.; Lau, C. N. Aryl Functionalization as a Route to Band Gap Engineering in Single Layer Graphene Devices. *Nano Letters* **2011**, *11*, 4047-4051.
(167)   Liu, L.; Shen, Z. Bandgap engineering of graphene: A density functional theory study. *Applied Physics Letters* **2009**, *95*, 252104.
(168)   Bhimanapati, G. R.; Lin, Z.; Meunier, V.; Jung, Y.; Cha, J.; Das, S.; Xiao, D.; Son, Y.; Strano, M. S.; Cooper, V. R.; Liang, L.; Louie, S. G.; Ringe, E.; Zhou, W.; Kim, S. S.; Naik, R. R.; Sumpter, B. G.; Terrones, H.; Xia, F.; Wang, Y.; Zhu, J.; Akinwande, D.; Alem, N.; Schuller, J. A.; Schaak, R. E.; Terrones, M.; Robinson, J. A. Recent Advances in Two-Dimensional Materials beyond Graphene. *ACS Nano* **2015**, *9*, 11509-11539.
(169)   Liu, H.; Neal, A. T.; Zhu, Z.; Luo, Z.; Xu, X.; Tománek, D.; Ye, P. D. Phosphorene: An Unexplored 2D Semiconductor with a High Hole Mobility. *ACS Nano* **2014**, *8*, 4033-4041.
(170)   Cai, Y.; Zhang, G.; Zhang, Y. W. Layer-dependent band alignment and work function of few-layer phosphorene. *Sci Rep* **2014**, *4*, 6677.
(171)   Yu, X.; Zhang, S.; Zeng, H.; Wang, Q. J. Lateral black phosphorene P−N junctions formed via chemical doping for high performance near-infrared photodetector. *Nano Energy* **2016**, *25*, 34-41.
(172)   Kuc, A.; Zibouche, N.; Heine, T. Influence of quantum confinement on the electronic structure of the transition metal sulfideTS2. *Physical Review B* **2011**, *83*.
(173)   Ataca, C.; Şahin, H.; Ciraci, S. Stable, Single-Layer MX2 Transition-Metal Oxides and Dichalcogenides in a Honeycomb-Like Structure. *The Journal of Physical Chemistry C* **2012**, *116*, 8983-8999.
(174)   Rao, C. N.; Gopalakrishnan, K.; Maitra, U. Comparative Study of Potential Applications of Graphene, MoS2, and Other Two-Dimensional Materials in Energy Devices, Sensors, and Related Areas. *ACS Appl Mater Interfaces* **2015**, *7*, 7809-7832.
(175)   Mak, K. F.; Shan, J. Photonics and optoelectronics of 2D semiconductor transition metal dichalcogenides. *Nature Photonics* **2016**, *10*, 216.
(176)   Yin, Z.; Li, H.; Li, H.; Jiang, L.; Shi, Y.; Sun, Y.; Lu, G.; Zhang, Q.; Chen, X.; Zhang, H. Single-Layer MoS2 Phototransistors. *ACS Nano* **2012**, *6*, 74-80.
(177)   Wang, L.; Jie, J.; Shao, Z.; Zhang, Q.; Zhang, X.; Wang, Y.; Sun, Z.; Lee, S.-T. MoS2/Si Heterojunction with Vertically Standing Layered Structure for Ultrafast, High-Detectivity, Self-Driven Visible–Near Infrared Photodetectors. *Advanced Functional Materials* **2015**, *25*, 2910-2919.
(178)   Xu, Y.; Yuan, J.; Fei, L.; Wang, X.; Bao, Q.; Wang, Y.; Zhang, K.; Zhang, Y. Selenium-Doped Black Phosphorus for High-Responsivity 2D Photodetectors. *Small* **2016**, *12*, 5000-5007.
(179)   Engel, M.; Steiner, M.; Avouris, P. Black Phosphorus Photodetector for Multispectral, High-Resolution Imaging. *Nano Letters* **2014**, *14*, 6414-6417.
(180)   Xia, F.; Mueller, T.; Lin, Y.-m.; Valdes-Garcia, A.; Avouris, P. Ultrafast graphene photodetector. *Nature Nanotechnology* **2009**, *4*, 839.
(181)   Lu, C.; Quan, C.; Si, K.; Xu, X.; He, C.; Zhao, Q.; Zhan, Y.; Xu, X. Charge transfer in graphene/WS2 enhancing the saturable absorption in mixed heterostructure films. *Applied Surface Science* **2019**, *479*, 1161-1168.
(182)   Li, X.; Tao, L.; Chen, Z.; Fang, H.; Li, X.; Wang, X.; Xu, J.-B.; Zhu, H. Graphene and related two-dimensional materials: Structure-property relationships for electronics and optoelectronics. *Applied Physics Reviews* **2017**, *4*.

****

(183)   Buron, J. D.; Pizzocchero, F.; Jepsen, P. U.; Petersen, D. H.; Caridad, J. M.; Jessen, B. S.; Booth, T. J.; Bøggild, P. Graphene mobility mapping. *Scientific Reports* **2015**, *5*, 12305.
(184)   Wang, K.; Szydłowska, B. M.; Wang, G.; Zhang, X.; Wang, J. J.; Magan, J. J.; Zhang, L.; Coleman, J. N.; Wang, J.; Blau, W. J. Ultrafast Nonlinear Excitation Dynamics of Black Phosphorus Nanosheets from Visible to Mid-Infrared. *ACS Nano* **2016**, *10*, 6923-6932.
(185)   Lherbier, A.; Blase, X.; Niquet, Y.-M.; Triozon, F.; Roche, S. Charge Transport in Chemically Doped 2D Graphene. *Physical Review Letters* **2008**, *101*, 036808.
(186)   Kang, J.; Jariwala, D.; Ryder, C. R.; Wells, S. A.; Choi, Y.; Hwang, E.; Cho, J. H.; Marks, T. J.; Hersam, M. C. Probing Out-of-Plane Charge Transport in Black Phosphorus with Graphene-Contacted Vertical Field-Effect Transistors. *Nano Letters* **2016**, *16*, 2580-2585.
(187)   Balis, N.; Stratakis, E.; Kymakis, E. Graphene and transition metal dichalcogenide nanosheets as charge transport layers for solution processed solar cells. *Materials Today* **2016**, *19*, 580-594.
(188)   Schmidt, H.; Giustiniano, F.; Eda, G. Electronic transport properties of transition metal dichalcogenide field-effect devices: surface and interface effects. *Chem Soc Rev* **2015**, *44*, 7715-7736.
(189)   Long, M.; Wang, P.; Fang, H.; Hu, W. Progress, Challenges, and Opportunities for 2D Material Based Photodetectors. *Advanced Functional Materials* **2018**, *29*.
(190)   Konstantatos, G.; Badioli, M.; Gaudreau, L.; Osmond, J.; Bernechea, M.; Garcia de Arquer, F. P.; Gatti, F.; Koppens, F. H. Hybrid graphene-quantum dot phototransistors with ultrahigh gain. *Nat Nanotechnol* **2012**, *7*, 363-368.
(191)   Wu, J.; Lu, Y.; Feng, S.; Wu, Z.; Lin, S.; Hao, Z.; Yao, T.; Li, X.; Zhu, H.; Lin, S. The Interaction between Quantum Dots and Graphene: The Applications in Graphene-Based Solar Cells and Photodetectors. *Advanced Functional Materials* **2018**, *28*.
(192)   Hu, J.; Shi, Y.; Zhang, Z.; Zhi, R.; Yang, S.; Zou, B. Recent progress of infrared photodetectors based on lead chalcogenide colloidal quantum dots. *Chinese Physics B* **2019**, *28*.
(193)   Ng, S. M. S. a. K. K.: *Physics of Semiconductor Devices, 3rd Edition*; John Wiley & Sons, Inc., 2007.
(194)   Schneider, H.; Walther, M.; Schönbein, C.; Rehm, R.; Fleissner, J.; Pletschen, W.; Braunstein, J.; Koidl, P.; Weimann, G.; Ziegler, J.; Cabanski, W. QWIP FPAs for high-performance thermal imaging. *Physica E: Low-dimensional Systems and Nanostructures* **2000**, *7*, 101-107.
(195)   Heinz, P.; Garmire, E. Photoconductive arrays for monitoring motion of spatial optical intensity patterns. *Appl. Opt.* **2007**, *46*, 8515-8526.
(196)   Konstantatos, G.; Sargent, E. H. Solution-Processed Quantum Dot Photodetectors. *Proceedings of the IEEE* **2009**, *97*, 1666-1683.
(197)   Koppens, F. H.; Mueller, T.; Avouris, P.; Ferrari, A. C.; Vitiello, M. S.; Polini, M. Photodetectors based on graphene, other two-dimensional materials and hybrid systems. *Nat Nanotechnol* **2014**, *9*, 780-793.
(198)   Law, M.; Beard, M. C.; Choi, S.; Luther, J. M.; Hanna, M. C.; Nozik, A. J. Determining the Internal Quantum Efficiency of PbSe Nanocrystal Solar Cells with the Aid of an Optical Model. *Nano Letters* **2008**, *8*, 3904-3910.
(199)   Sun, Z.; Liu, Z.; Li, J.; Tai, G. A.; Lau, S. P.; Yan, F. Infrared photodetectors based on CVD-grown graphene and PbS quantum dots with ultrahigh responsivity. *Adv Mater* **2012**, *24*, 5878-5883.
(200)   Turyanska, L.; Makarovsky, O.; Svatek, S. A.; Beton, P. H.; Mellor, C. J.; Patanè, A.; Eaves, L.; Thomas, N. R.; Fay, M. W.; Marsden, A. J.; Wilson, N. R. Ligand-Induced Control of Photoconductive Gain and Doping in a Hybrid Graphene-Quantum Dot Transistor. *Advanced Electronic Materials* **2015**, *1*.

****

(201)   Nian, Q.; Gao, L.; Hu, Y.; Deng, B.; Tang, J.; Cheng, G. J. Graphene/PbS-Quantum Dots/Graphene Sandwich Structures Enabled by Laser Shock Imprinting for High Performance Photodetectors. *ACS Appl Mater Interfaces* **2017**, *9*, 44715-44723.
(202)   Zhang, Y.; Cao, M.; Song, X.; Wang, J.; Che, Y.; Dai, H.; Ding, X.; Zhang, G.; Yao, J. Multiheterojunction Phototransistors Based on Graphene–PbSe Quantum Dot Hybrids. *The Journal of Physical Chemistry C* **2015**, *119*, 21739-21743.
(203)   Chen, W.; Castro, J.; Ahn, S.; Li, X.; Vazquez-Mena, O. Improved Charge Extraction Beyond Diffusion Length by Layer-by-Layer Multistacking Intercalation of Graphene Layers inside Quantum Dots Films. *Adv Mater* **2019**, *31*, e1807894.
(204)   Grotevent, M. J.; Hail, C. U.; Yakunin, S.; Dirin, D. N.; Thodkar, K.; Borin Barin, G.; Guyot-Sionnest, P.; Calame, M.; Poulikakos, D.; Kovalenko, M. V.; Shorubalko, I. Nanoprinted Quantum Dot–Graphene Photodetectors. *Advanced Optical Materials* **2019**.
(205)   Nikitskiy, I.; Goossens, S.; Kufer, D.; Lasanta, T.; Navickaite, G.; Koppens, F. H.; Konstantatos, G. Integrating an electrically active colloidal quantum dot photodiode with a graphene phototransistor. *Nat Commun* **2016**, *7*, 11954.
(206)   Che, Y.; Cao, X.; Yao, J. A PbSe nanocrystal vertical phototransistor with graphene electrode. *Optical Materials* **2019**, *89*, 138-141.
(207)   Lin, C.-C.; Wang, D.-Y.; Tu, K.-H.; Jiang, Y.-T.; Hsieh, M.-H.; Chen, C.-C.; Chen, C.-W. Enhanced infrared light harvesting of inorganic nanocrystal photovoltaic and photodetector on graphene electrode. *Applied Physics Letters* **2011**, *98*.
(208)   Che, Y.; Zhang, Y.; Cao, X.; Song, X.; Zhang, H.; Cao, M.; Dai, H.; Yang, J.; Zhang, G.; Yao, J. High-performance PbS quantum dot vertical field-effect phototransistor using graphene as a transparent electrode. *Applied Physics Letters* **2016**, *109*.
(209)   Che, Y.; Zhang, Y.; Cao, X.; Zhang, H.; Song, X.; Cao, M.; Yu, Y.; Dai, H.; Yang, J.; Zhang, G.; Yao, J. Ambipolar Graphene-Quantum Dot Hybrid Vertical Photodetector with a Graphene Electrode. *ACS Appl Mater Interfaces* **2017**, *9*, 32001-32007.
(210)   Kufer, D.; Nikitskiy, I.; Lasanta, T.; Navickaite, G.; Koppens, F. H.; Konstantatos, G. Hybrid 2D-0D MoS2 -PbS quantum dot photodetectors. *Adv Mater* **2015**, *27*, 176-180.
(211)   Kufer, D.; Lasanta, T.; Bernechea, M.; Koppens, F. H. L.; Konstantatos, G. Interface Engineering in Hybrid Quantum Dot–2D Phototransistors. *ACS Photonics* **2016**, *3*, 1324-1330.
(212)   Pak, S.; Cho, Y.; Hong, J.; Lee, J.; Lee, S.; Hou, B.; An, G.-H.; Lee, Y.-W.; Jang, J. E.; Im, H.; Morris, S. M.; Sohn, J. I.; Cha, S.; Kim, J. M. Consecutive Junction-Induced Efficient Charge Separation Mechanisms for High-Performance MoS2/Quantum Dot Phototransistors. *ACS Applied Materials & Interfaces* **2018**, *10*, 38264-38271.
(213)   Yu, Y.; Zhang, Y.; Song, X.; Zhang, H.; Cao, M.; Che, Y.; Dai, H.; Yang, J.; Zhang, H.; Yao, J. PbS-Decorated WS2 Phototransistors with Fast Response. *ACS Photonics* **2017**, *4*, 950-956.
(214)   Hu, C.; Dong, D.; Yang, X.; Qiao, K.; Yang, D.; Deng, H.; Yuan, S.; Khan, J.; Lan, Y.; Song, H.; Tang, J. Synergistic Effect of Hybrid PbS Quantum Dots/2D-WSe2Toward High Performance and Broadband Phototransistors. *Advanced Functional Materials* **2017**, *27*.
(215)   Özdemir, O.; Ramiro, I.; Gupta, S.; Konstantatos, G. High Sensitivity Hybrid PbS CQD-TMDC Photodetectors up to 2 μm. *ACS Photonics* **2019**, *6*, 2381-2386.
(216)   Pradhan, S.; Stavrinadis, A.; Gupta, S.; Bi, Y.; Di Stasio, F.; Konstantatos, G. Trap-State Suppression and Improved Charge Transport in PbS Quantum Dot Solar Cells with Synergistic Mixed-Ligand Treatments. *Small* **2017**, *13*, 1700598.
(217)   Gao, L.; Chen, C.; Zeng, K.; Ge, C.; Yang, D.; Song, H.; Tang, J. Broadband, sensitive and spectrally distinctive SnS2 nanosheet/PbS colloidal quantum dot hybrid photodetector. *Light Sci Appl* **2016**, *5*, e16126.
(218)   You, C.; Zhang, G.; Deng, W.; Zhao, C.; An, B.; Liu, B.; Wang, B.; Yan, H.; Liu, D.; Zhang, Y. Cascade-type energy band design of a black phosphorus photodetector with high performance. *Journal of Materials Chemistry C* **2019**, *7*, 2232-2239.

****

(219)   Kwak, D. H.; Ra, H. S.; Yang, J.; Jeong, M. H.; Lee, A. Y.; Lee, W.; Hwang, J. Y.; Lee, J. H.; Lee, J. S. Recovery Mechanism of Degraded Black Phosphorus Field-Effect Transistors by 1,2-Ethanedithiol Chemistry and Extended Device Stability. *Small* **2018**, *14*.

(220)   Lee, A. Y.; Ra, H. S.; Kwak, D. H.; Jeong, M. H.; Park, J. H.; Kang, Y. S.; Chae, W. S.; Lee, J. S. Hybrid Black Phosphorus/Zero-Dimensional Quantum Dot Phototransistors: Tunable Photodoping and Enhanced Photoresponsivity. *ACS Appl Mater Interfaces* **2018**, *10*, 16033-16040.

(221)   Luo, P.; Zhuge, F.; Wang, F.; Lian, L.; Liu, K.; Zhang, J.; Zhai, T. PbSe Quantum Dots Sensitized High-Mobility Bi2O2Se Nanosheets for High-Performance and Broadband Photodetection Beyond 2 μm. *ACS Nano* **2019**, *13*, 9028-9037.

(222)   Dagtepe, P.; Chikan, V. Quantized Ostwald Ripening of Colloidal Nanoparticles. *The Journal of Physical Chemistry C* **2010**, *114*, 16263-16269.

(223)   Kim, S.; Marshall, A. R.; Kroupa, D. M.; Miller, E. M.; Luther, J. M.; Jeong, S.; Beard, M. C. Air-Stable and Efficient PbSe Quantum-Dot Solar Cells Based upon ZnSe to PbSe Cation-Exchanged Quantum Dots. *ACS Nano* **2015**, *9*, 8157-8164.

(224)   Padilha, L. A. S., J. T.; Sandberg, R. L.; Bae, W. K.; Koh, W.; Pietryga, J. M.; Klimov, V. I. Carrier Multiplication in Semiconductor Nanocrystals: Influence of Size, Shape, and Composition. *Accounts of Chemical Research* **2013**, *46*, 1261-1269.

(225)   Zhang, C.; Lian, L.; Yang, Z.; Zhang, J.; Zhu, H. Quantum Confinement-Tunable Ultrafast Charge Transfer in a PbS Quantum Dots/WSe2 0D-2D Hybrid Structure: Transition from the Weak to Strong Coupling Regime. *J Phys Chem Lett* **2019**, 7665-7671.

****